Measuring the fluctuating Hydraulic Gradient in bed protections

Validating a model for pressure fluctuations in rock layers induced by flow and waves, towards improving open filter design

CEGM0500 Master Thesis

S.R. Ledeboer

Delft University of Technology

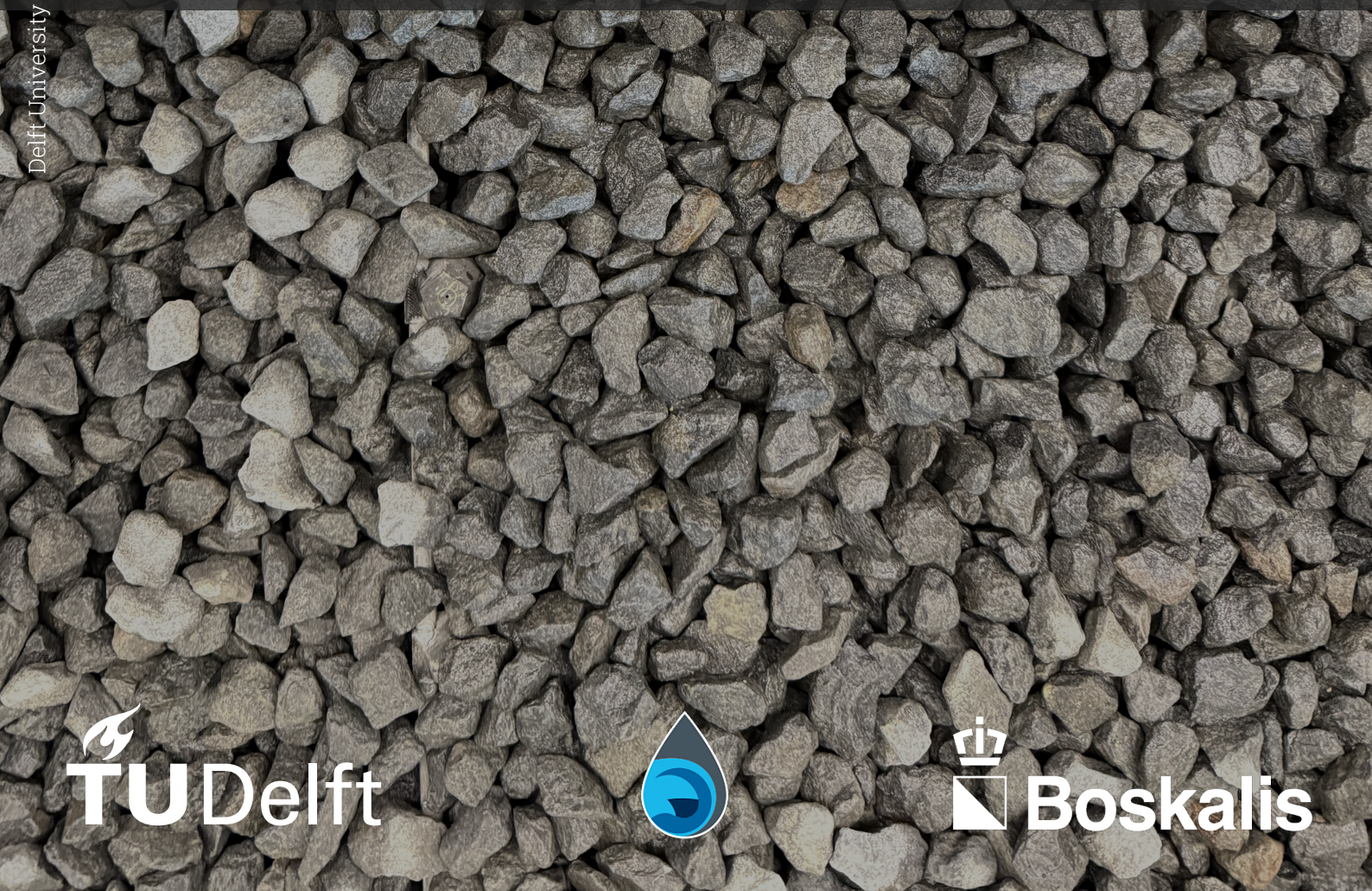

TU Delft

Boskalis

Measuring the fluctuating Hydraulic Gradient in bed protections

Validating a model for pressure fluctuations in rock layers induced by flow and waves, towards improving open filter design

by

S.R. Ledeboer

in partial fulfilment of the requirements to obtain the degree of Master of Science at the Delft University of Technology

Student Number	:	4866487
Faculty	:	Civil Engineering and Geosciences
Study	:	Msc. Civil Engineering
Program	:	Hydraulic and Offshore Structures
Project Duration	:	04, 2025 - 12, 2025

Thesis Committee

Chair	dr. ir. B. Hofland	Delft University of Technology
Supervisor	prof. dr. ir. M.R.A. van Gent	Delft University of Technology
Supervisor	ir. J. P. van den Bos	Royal Boskalis Westminster N.V.

This thesis was written with the assistance of OpenAI's ChatGPT, which was used to draft and refine Python scripts for data processing and analysis, and to improve grammar, spelling, and academic readability.

Het experimentele werk in dit onderzoek is mede gefinancierd uit de PPS-innovatie programmasubsidie van het ministerie van Economische Zaken en Klimaat, binnen het TKI Deltatechnologie-project TU16/LabCoSts2.

TU Delft

TOPSECTOR WATER & MARITIEM

Boskalis

Preface

This thesis presents the research conducted as part of the Civil Engineering Master's programme in the field of Hydraulic and Offshore Structures at Delft University of Technology. The work was carried out between April and December 2025, partly at the university and partly at Boskalis. The experimental campaign took place in the Waterlab of the Faculty of Civil Engineering and Geosciences. The study investigates the load and damping of hydraulic pressure fluctuations within open granular filter layers, with the aim of contributing to more comprehensive and improved design approaches for bed, bank, and shore protections.

I am grateful to Boskalis for the opportunity to conduct my thesis within the company and for the insights shared by many colleagues. A special thanks goes to Jeroen van den Bos for his supervision, guidance, and for helping me keep sight of the bigger picture. I also thank Quinten Thomas for developing the underlying model and for his support in applying it.

My sincere gratitude goes to my TU Delft supervisors, Bas Hofland and Marcel van Gent, whose enthusiasm for hydraulic engineering, together with their expertise, guidance, and constructive feedback, have been invaluable throughout this project.

I am also thankful to the Hydraulic Engineering technical staff, in particular Chantal Willems, Arie van der Vlies, Arno Doorn, Jennifer Rietdijk, and Frank Kalkman, for their active support during the experimental campaign. Their help with preparatory tests, creative problem-solving, and the setup and operation of equipment was essential for the successful execution of the experiments. I additionally thank Wim Uijttewaal for his guidance and for helping me make some final improvements to the test setup.

Finally, I wish to thank my family and friends for their encouragement, support, and valuable perspectives throughout the completion of this thesis. A special thanks to my brother for assisting me in cleaning and preparing the testing materials.

S.R. Ledeboer
Rotterdam, December 2025

Summary

This thesis examines the propagation of turbulent and wave-induced pressure fluctuations through open granular filter layers through experimental validation and extension of an existing theoretical model. The focus lies on the fluctuating hydraulic gradient within the filter, which can be used to determine the hydraulic load on geotextiles placed beneath it. As hydraulic engineering increasingly adopts natural geotextiles as sustainable alternatives to synthetic fabrics, understanding this fluctuating load becomes essential. Natural geotextiles typically have larger pore openings and lower mechanical strength, making them more sensitive to local hydraulic gradients. Reliable knowledge of the magnitude and spectral structure of these gradients is therefore necessary for the safe and efficient design of bed, bank and shore-protections.

Background

Traditional granular filter design primarily addresses mechanical stability, while the dynamic component of hydraulic loading caused by turbulence is far less understood. Previous studies documented turbulent pressures acting *on top* of granular filters, but did not quantify their transmission *through* the layer. The spectral model of Thomas (2023) addresses this gap by predicting the wavenumber-dependent damping of pressure fluctuations within porous media. This thesis experimentally validates that theoretical framework.

Methodology

Experiments were conducted in the sediment flume of the Hydraulic Engineering lab at TU Delft using two vertically aligned twelve-sensor Pressure Sensor Arrays (PSAs) installed at the top and base of filters with thicknesses $D_f = 4, 6, 8$ cm. Tests included current-driven and wave-induced conditions across varying flow velocities and water depths. Pressure time-series signals were processed using linear detrending, Hampel filtering, and high-pass filtering. From these signals, pressure spectra were formed using the Welch method, with additional coherence filtering applied during the construction of the Power Spectral Densities (PSDs). Subsequently, white-noise filtering and notch filtering were applied to further purify the power spectral densities. Using ω–k conversion, based on the convection approximation $d\omega/dk \approx 0.44, \overline{U}$, the time-series-based PSDs were transformed into spatial PSDs. Damping ratios and hydraulic gradient spectra were then computed using both direct and indirect spectral approaches.

Results

Overall, the experimental results show a broadly consistent agreement with the theoretical hypothesis, particularly under highly turbulent conditions characterised by high flow velocities and shallow water depths. Although some deviations remain, especially when viewed on logarithmic scales, the main spectral trend of the filter-top interface generally follows the expected patterns.

The experiments further demonstrate that *damping efficiency is heavily influenced by geometric parameters*, the filter thickness D_f and water depth h. Their ratio, h/D_f, provides the clearest predictor for attenuation behaviour. Thicker layers and shallower water exhibit stronger damping, whereas thin layers and larger water depths allow more turbulent energy to reach the base, highlighting that hydraulic performance depends not only on material properties but also on the geometric configuration of the system.

In contrast, *flow velocity does not significantly alter the damping efficiency*. The shape of the attenuation curve remains similar across velocities. Instead, velocity determines the *absolute hydraulic load*: higher $\overline{U}$ produces a larger turbulent input, increasing the gradient amplitude even when the relative damping remains unchanged.

Wave-induced fluctuations (low wavenumbers) displayed very weak damping, penetrating the filter layers and experiencing little reduction. The indirect spectral method aligned well with the theoretical model across low and mid wavenumbers, while the direct method showed greater sensitivity to measurement spacing and noise. The anomalously low damping observed for the 6 cm layer is attributed to the upper PSA being positioned too deeply, causing premature attenuation of the signal.

Discussion

The limited damping of wave-induced (low-k) fluctuations highlights that empirical design rules linking filter thickness solely to stone size do not fully capture the hydraulic performance of open filters, especially when combined with geotextiles. Because natural geotextiles are more permeable and mechanically weaker than synthetic alternatives, a detailed understanding of the fluctuating hydraulic load is crucial for their safe application.

Methodological uncertainties, including PSA placement, convection-velocity estimation, and lateral flow effects, introduced variability between test but did not compromise the observed spectral trends or the validation of the theoretical model.

Conclusions and Recommendations

The principal findings of this thesis are:

- Damping increases with filter thickness and wavenumber, and decreases with relative water depth h/D_f.
- Flow velocity influences the *magnitude* of the hydraulic load but not the *damping efficiency*, which is governed by geometry.
- Wave-induced loads experience limited attenuation, indicating the need for thicker or multiple filter layers under oscillatory conditions.
- The indirect spectral method is validated as a reliable approach for determining hydraulic gradient spectra.

Recommended avenues for future research include:

- Determining the convection velocity empirically using cross-spectral density to reduce uncertainty in ω–k conversion.
- Investigating lateral attenuation patterns using the full 12-sensor PSA configurations.
- Developing a load-type-dependent correction factor to refine design relations for D_{n50} and filter thickness.
- Study the influence of combined current-wave regimes.
- Study the effect on damping or load on the base using multiple open granular filter layers.

Overall, this thesis provides experimental validation of a spectral damping model for open granular filters and delivers a physical basis for designing hydraulically efficient and environmentally sustainable filter-geotextile systems.

Contents

1

Introduction

1.1. Background

Geotextiles are permeable fabrics placed between soil and granular layers to provide separation, and protection. While synthetic variants, typically manufactured from polypropylene (PP), polyester, nylon, fibreglass, or polyethylene (PE), are commonly used, growing environmental concerns have increased interest in natural alternatives such as jute, hemp, wool, and coconut fibre. Although geotextiles are not the main subject of this study, they form the background motivation for examining the hydraulic loads transmitted through granular filter layers, as these loads ultimately determine the applicability of natural geotextiles in bed protections.

Above a geotextile, or directly on top of a base layer, a granular filter is typically applied. Such filters can be classified as either geometrically closed or geometrically open, depending on whether material transport between layers is prevented or permitted. In open filters, limited material exchange is allowed, increasing the ratio between the filter material and the underlayer material Wolters and Van Gent, 2012. Traditionally, several closed filter layers are required to protect the base, but the presence of a geotextile can reduce this number, offering potential cost savings. This motivates the broader question underlying the present research: what hydraulic loads are transmitted through an open filter layer, and how effectively can such layers dampen turbulent fluctuations?

The focus of this study is therefore on the hydraulic behaviour of *open granular filter layers*, irrespective of whether a geotextile is present. The work builds upon the spectral framework of Thomas (2023), who introduced a new design method for open filters applicable to both single and double filter configurations. Whereas the resistance capacity of natural geotextiles has been investigated by Akerboom (2024), the current study examines the *load side* of the problem: the hydraulic gradient within and across the filter layer, and the relationship between its mean component and its turbulent fluctuations.

A key parameter in the design of open filters is the actual hydraulic gradient, which consists of a mean part and a fluctuating part. As expressed in Equation 1.1, this gradient must remain below the critical value associated with failure mechanisms such as uplift or internal instability. This thesis does not analyse the geotextile capacity (i_{cr}); instead, it investigates the imposed loads (i), focusing on the magnitude and behaviour of the hydraulic gradient components $\bar{i}$ and i'. Understanding this behaviour provides insight relevant both for conventional bed protections and for the potential integration of natural geotextiles in future designs.

$$i_{cr} > i = \bar{i} + i' \tag{1.1}$$

The study of Bakker et al., 1994, after Wörman, 1989 proposed a relation between the thickness of the filter layer and the hydraulic to obtain the turbulent component.

This study aims to validate and test the theoretical model described by Thomas (2023), which defines the ratio between the turbulent and mean hydraulic gradient components in open filter layers. This is

important to determine the share of the load of turbulence (i') compared to the average gradient $(\bar{i})$ in open channel flow with open filters as bed protection.

This paper will focus on the characteristics and the combination of open filters with natural geotextiles. According to Akerboom, 2024, there has not been sufficient knowledge on the use of these together. The study by Thomas, 2023, which serves as the direct starting point for this research, it suggests that the turbulent component of the actual hydraulic gradient can be derived from measured turbulent wall pressure spectra at the top of the filter layer. Based on spectral approach and linear damping, it is hypothesized that these turbulent components undergo damping within the filter layer, resulting in a diminished turbulent component at the filter/base interface. The research compared the data from two separate experiments performed by Wolters and Van Gent, 2012 and Van de Sande, 2012 to verify the hypothesis. These experiments did not use The hypothesis can be further verified, by diving further into the turbulent gradient component and perform physical testing, to get an even better understanding of the turbulent gradient. By measuring the pressures at both the interfaces of the open filter, the turbulence at the wall (filter/ base interface) and between the top of the filter layer, a further understanding of the damping within the porous medium can be obtained.

Hofland, 2005 studied the effects of turbulent pressures at the top of the filter layer. There has not been found a distribution of pressure at the filter/base interface, therefore it is necessary to perform tests at both interfaces of the filter, to obtain the turbulent component of the actual gradient. The study by Wolters and Van Gent, 2012 found that filter thickness plays a dominant role in base material transport. However, due to limited experimental data, no definitive conclusions have been drawn. This knowledge gap presents an opportunity to further investigate the damping effects of different filter thicknesses on turbulence.

1.2. Objective and Research questions

The goal of this research is to expand the understanding of the stability of open filters under uniform flow by extending and validating the spectral theory proposed by Thomas, 2023. This study aims to determine the turbulent load on the filter/base interface by analysing turbulent wall pressures and determine the hydraulic gradients through granular filter layers. Through physical experiments and spectral analysis, the research will assess the dampening of pressure fluctuations by applying a granular filter.

1.2.1. Main research question

The aim of this research yields the next main research question:

How can the spectral framework of Thomas (2023) be applied and experimentally validated to describe the turbulent (and wave-induced) pressure fluctuations within open granular filter layers?

1.2.2. Sub-questions

To answer the main research question, the following sub-questions have been drawn up:

1. How can instantaneous pressure fluctuations and resulting hydraulic gradients through the filter layer be accurately measured and determined?
2. How do variations in water depth and flow velocity influence the pressure power spectral density due to turbulent pressure fluctuations near the top of the filter?
3. How does the thickness of the filter layer affect the damping of turbulent and wave-induced pressure fluctuations between the top and base of the filter?
4. What is the influence of the ratio between water depth and filter thickness on the transmission and damping of flow-induced pressure fluctuations within the filter layer?

1.3. Thesis Outline

This thesis is structured into eight chapters. chapter 2 presents the theoretical framework that forms the foundation of this research, outlining the key physical principles, governing equations, and previous findings relevant to the study. chapter 3 describes the experimental setup and procedures used to obtain the data necessary to address the research questions. chapter 4 details the data acquisition, handling, and filtering techniques applied to convert the raw measurements into usable datasets.

chapter 5 interprets the processed data through the lens of the theoretical background, translating the experimental observations into physical insights and visual representations that support the research objectives. The results are further examined in chapter 6, which critically evaluates the assumptions, limitations, and uncertainties that may have influenced the outcomes.

Finally, chapter 7 summarises the main findings and systematically answers the research questions, while chapter 8 provides directions for future work and discusses how the insights gained from this study can be applied and further developed within the field.

2

Theoretical Framework

This chapter provides a structured overview of the interrelations among the key factors influencing the gradient fluctuations. Sections 2.1, 2.2, and 2.3 outline the fundamental principles governing the hydraulic load, the stability of individual rock elements, and the collective behaviour of the filter layer, respectively. Subsequently, section 2.4 addresses the physical mechanisms underlying the turbulent hydraulic gradient, beginning with the Navier-Stokes equations. The spectral theoretical hypotheses, originally developed from the wind tunnel experiments of Blake, 1970 and later formalised by Thomas, 2023, are presented in section 2.5. The corresponding transformation processes employed to validate the spectral theory are described in Sections 2.6 & 2.7, followed by the derivation of the damping hypothesis based on linear wave theory (Dean and Dalrymple, 1991) in section 2.8. Finally the loading caused by the fluctuating gradient is covered in section 2.9. The theoretical relations are finally summarised and visualised in the Conceptual Framework at the end of this chapter.

2.1. Hydrodynamic principles

This section briefly shows the fundamental hydrodynamic processes, this will cover basic equations from Forchheimer, Chezy, Reynolds, and Froude.

2.1.1. Wall Flow

Wall flow refers to the flow of water along a solid boundary, such as a channel bed, where the effects of viscosity and turbulence near the wall govern the momentum exchange between the fluid and the boundary. In such flows, the shear stress at the bed, τ_b, represents the key driving mechanism that balances the downslope component of the gravitational force acting on the water mass. For steady, uniform flow, an equilibrium exists between this shear stress and the hydrostatic pressure gradient along the slope. The bottom shear stress can be expressed as:

$$\tau_b = \rho \cdot g \cdot h \cdot i \tag{2.1}$$

where ρ is the fluid density, g the gravitational acceleration, h the water depth, and I the bed slope. This relationship links the hydraulic gradient to the mean flow velocity through empirical formulations such as those of Chezy.

Chezy Equation

The Chezy equation provides an empirical relationship between the mean flow velocity and the driving hydraulic and geometric parameters of the flow. It is derived from the balance between gravitational acceleration and frictional resistance within a steady, uniform flow, and can be expressed as:

$$\overline{\overline{u}} = C\sqrt{i \cdot R} \tag{2.2}$$

where $\overline{\overline{u}}$ is the depth- and time-averaged velocity, I is the slope or hydraulic gradient, R is the hydraulic radius (equal to the flow area divided by the wetted perimeter), and C is the dimensionless Chezy coefficient. The coefficient C encapsulates the effects of bed roughness and flow turbulence, and thus represents the overall efficiency of the flow.

The Chezy coefficient can be related to physical roughness through the Nikuradse-Colebrook relation for hydraulically rough flow conditions:

$$C = \sqrt{\frac{g}{c_f}} = \frac{\sqrt{g}}{\kappa} \ln\left(\frac{12R}{k_r}\right) \approx 18 \log\left(\frac{12R}{k_r}\right) \qquad \text{with:} \quad k_r = 2 * d_{n50} \quad \& \quad R = \frac{wh}{w + 2h} \tag{2.3}$$

where c_f is the dimensionless friction factor, g is the gravitational acceleration, κ is the von Kármán constant, and k_r is the equivalent Nikuradse roughness height, which is typically several times the characteristic grain diameter of the bed material. The relation shows that higher roughness results in lower C values and therefore greater flow resistance.

Physically, the Chezy equation assumes that the turbulent energy generated by the bed roughness is in equilibrium with the gravitational energy input driving the flow. This makes it a convenient and robust formulation for uniform, fully developed turbulent flow over rough boundaries, such as those encountered in rock beds or open filters. In the present work, the Chezy equation is used to relate the mean velocity $\overline{\overline{u}}$ and the bed shear stress via the shear velocity u_*:

$$u_* = \frac{\overline{\overline{u}}\sqrt{g}}{C} \tag{2.4}$$

Which provides a direct link between measurable flow quantities and the near-bed shear dynamics. Because the Chezy coefficient incorporates both hydraulic roughness and flow geometry, it serves as a practical and physically consistent means of describing the bulk flow conditions used throughout this study.

2.1.2. Porous flow

The Forchheimer equation is used to consider the posibility of the inertial flow effects due to the narrowing of pores by formation damage in the momentum balance, according to Civan, 2023.

$$\frac{1}{\rho g}\frac{\partial p}{\partial x} = i = a u_f + b u_f |u_f| + c\frac{\partial u_f}{\partial t} \tag{2.5}$$

During the experiments is stationary flow assumed, therefore the term $\frac{\partial u_f}{\partial t}$ can be omitted, and the following equation can be derived:

$$i = a u_f + b u_f |u_f| \tag{2.6}$$

The empirical parameters a and b can be calculated as stated in Equation 2.7, ”the dimensionless coefficients α and β (that depend on, among other things, the grading and the shape of the grains) have to be determined experimentally. Without any further information, $\alpha \approx 1000$ and $\beta \approx 1.1$ can be used as a first estimate (with possible values twice as low or twice as high).”(Schiereck and Verhagen, 2019, p. 106).

$$\text{with:} \quad a = \alpha\left(\frac{(1-n)^2}{n^3}\right)\frac{\nu}{g\, d_{(n)50}^2}, \qquad b = \beta\left(\frac{1-n}{n^3}\right)\frac{1}{g\, d_{(n)50}} \tag{2.7}$$

The filter velocity shown in Equation 2.6 can be derived when equalizing the Forchheimer gradient to the gradient through average velocity. Equation 2.8 shows the calculation for the gradient obtained with the average velocity, Hydraulic Radius and Chezy coefficient.

$$i = \frac{\overline{u}^2}{C^2 R} \tag{2.8}$$

The filter velocity can now be derived using Equation 2.6 and the quadratic formula, next the last boundary condition can be implemented:

$$Re_p = \frac{u_f D_{n50}}{n\nu} \tag{2.9}$$

According to Burcharth and Christensen, 1991 the value of 300 for the porous Reynolds number dictates the lower boundary of the turbulent flow regime, ”the fully turbulent flow regime should be somewhat larger, i.e. $Re_c \simeq 600$–1000”.

2.1.3. Flow Regime

The flow regime in open-channel hydraulics is primarily governed by the ratio between inertial and gravitational forces, expressed by the dimensionless *Froude number*:

$$Fr = \frac{U}{\sqrt{gh}}, \tag{2.10}$$

where U is the characteristic flow velocity, g the gravitational acceleration, and h the characteristic water depth. The Froude number indicates the relative importance of inertia and gravity in determining the behaviour of the free surface and thus serves as a key parameter in classifying flow regimes.

Flows are referred to as *subcritical* when $Fr < 1$, meaning that gravitational effects dominate and surface disturbances can propagate upstream. When $Fr = 1$, the flow is said to be *critical*, representing the transition between slow and fast flow conditions. For $Fr > 1$, the flow becomes *supercritical*, dominated by inertia, where disturbances cannot travel upstream and energy dissipation may occur through hydraulic jumps.

Although the Froude number does not directly describe the stability of the flow in the hydrodynamic sense, it provides an essential indication of the flow regime and the dynamic behaviour of the water surface. In this study, it is used to characterise the hydraulic state of the flow above and within the filter layer.

2.2. Rock Stability

The stability of granular material in a filter or bed layer can be evaluated using the Shields parameter, which defines the ratio between the applied bed shear stress and the submerged weight of a representative particle. For stable conditions, the Shields parameter must remain below the threshold $\psi < 0.03$. The Shields equation can be expressed as:

$$\psi = \frac{\tau}{(\rho_s - \rho_w) g d_{50}} = \frac{u_*^2}{\Delta g d_{50}} \Rightarrow d_{50} = \frac{u_*^2}{\psi g \Delta} \tag{2.11}$$

Where ρ_s and ρ_w are the sediment and water densities, respectively, d_{50} is the median particle diameter, $\Delta = (\rho_s - \rho_w)/\rho_w$ is the relative density difference, and u_* is the shear velocity defined in Equation 2.4.

The shear velocity u_* can then be obtained through the Chezy relation given in Equation 2.2, with the roughness and hydraulic radius from Equation 2.3. Because the roughness height k_r is approximately twice the nominal grain size, the Chezy coefficient C depends directly on the assumed grain diameter.

Finally, the conversion from the median to the nominal grain diameter follows:

$$d_{n50} = 0.84\, d_{50}, \tag{2.12}$$

By iteratively adjusting d_{n50} and recomputing C, u_*, and ψ, the design converges toward a stable configuration satisfying the Shields criterion. Since only water is used as the working fluid in the experiments, the density ρ in Equation 2.4 corresponds to ρ_w.

2.3. Rock Filters

Filter layers or geotextiles are meant to reduce flow through porous media or around hard structures and prevent erosion. In short filter layers are meant to make a smooth transition between base material and hard structures. There are two types of filters, *Geometrically Open filter* layers and *Geometrically Closed filter* layers.

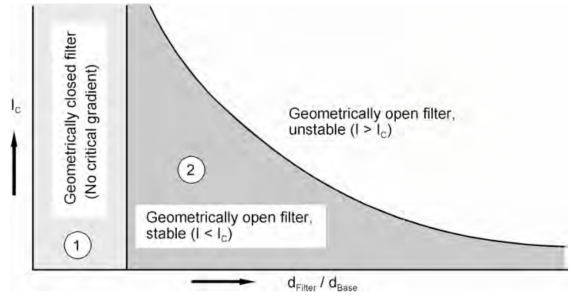

Figure 2.1: Possible design criteria for granular filters, (Schiereck and Verhagen, 2019)

2.3.1. Geometrically Closed Filters

Geometrically closed filters are designed to prevent the migration of base material through the filter layer by ensuring a stable gradation relationship between the two layers. The principle of closure is governed by the relative particle sizes of the filter material and the base material beneath it. A geometrically closed filter has a sufficiently small pore size to block the movement of finer base particles, while still allowing seepage flow to occur without inducing excessive pore pressures.

The stability criterion in Equation 2.13, according to Schiereck and Verhagen (2019) using the method of Terzaghi and Peck (1948), ensures that the openings between the filter particles are too small for the underlying material to be entrained, thus preventing internal erosion or piping. The internal stability condition guarantees that the filter itself is not prone to segregation or self-filtration under hydraulic loading, preserving its structure and permeability over time. The permeability criterion ensures that the filter layer remains adequately permeable to transmit seepage water without generating uplift pressures in the base layer.

$$\text{Stability: } \frac{d_{15f}}{d_{85b}} < 5 \quad \text{Int. Stability: } \frac{d_{60}}{d_{10}} < 10 \quad \text{Permeability: } \frac{d_{15f}}{d_{15b}} > 5 \tag{2.13}$$

In essence, a geometrically closed filter acts as a barrier that maintains mechanical stability by restricting soil particle movement across the interface, while still fulfilling the hydraulic function of safely dissipating pore water pressures.

2.3.2. Geometrically Open Filters

Geometrically open, or *hydraulically sand-tight*, filters are designed to stabilize the base material not by geometric retention, but by damping the hydraulic load within the filter layer itself. In contrast to geometrically closed filters, which prevent particle movement by minimizing pore openings, geometrically open filters allow partial communication between the base and filter layers. Their stability is governed by hydraulic interaction rather than mechanical exclusion. The essential requirement is that the hydraulic load at the interface between the filter and base layer is sufficiently reduced such that the driving forces on the base material remain below its threshold of motion Schiereck and Verhagen, 2019; Van de Sande, 2012.

Within such filters, flow is generally turbulent, and pressure fluctuations are transmitted through the voids of the filter layer. The attenuation of these fluctuations depends on the porosity, particle size distribution, and thickness of the filter. Stable geometrically open filters thus rely on an equilibrium between hydraulic damping and particle mobility: although the base material can theoretically pass through the pores, the flow-induced stresses are sufficiently dissipated before reaching the interface, preventing erosion or winnowing. These systems are easier to construct and maintain than

geometrically closed filters, but they require a thicker layer to ensure adequate energy dissipation and stability under varying hydraulic conditions Van de Sande, 2012.

Three main design approaches exist for the stability of geometrically open filters. Each approach relates the ratio between the filter and base material sizes to hydraulic and geometric parameters that influence erosion resistance.

Wörman (1989)

Wörman, 1989 developed an empirical relationship for single-layer open filter structures under non-uniform flow conditions, such as those found around bridge piers. His design approach assumes that the filter stability depends on the balance between hydraulic loading and the density contrast between the base and filter materials:

$$\frac{d_{15t}}{d_{85b}} = 5\frac{(1-n_t)}{n_t}\frac{\Delta_b}{\Delta_t}\frac{D}{d_{50t}} \tag{2.14}$$

This relationship indicates that, for coarser filters (larger d_{50t}), the hydraulic load must be further damped by sufficient layer thickness D or porosity control to prevent base material instability.

Bakker & Konter (1994)

Bakker et al., 1994 extended the concept to uniform flow conditions by including the influence of turbulent fluctuations within the filter, expressed through the hydraulic radius R. Their formulation incorporates the turbulence coefficient C_0 and a correction factor e to represent flow differences between open channels and porous media. The resulting design equation is given as:

$$\frac{D_{15f}}{d_{85b}} = 6.25\frac{(1-n)}{n}\frac{d}{R}\frac{\Delta_b}{\Delta_t}\frac{R}{D_{85t}} \tag{2.15}$$

This expression emphasizes that filter stability is not solely dependent on geometric ratios, but also on hydraulic roughness and turbulence intensity within the filter layer. Higher turbulence levels require smaller filter-to-base size ratios to maintain stability.

Van de Sande (2012)

Building on previous work, Van de Sande, 2012 introduced a more comprehensive relation that includes the effects of material properties such as relative density Δ, stability parameters Ψ_c, and shape factors V_G. This approach allows for probabilistic assessment and has been validated through extensive flume testing for single-layered open filters:

$$\frac{D_f}{d_{15f}} = \alpha_d \ln\left(\frac{\Delta_f d_{50f}\,\Psi_{cf}\,(1-\gamma V_{Gf})}{\Delta_b d_{50b}\,\Psi_{cb}\,(1-\gamma V_{Gb})}\right) \tag{2.16}$$

The logarithmic relationship reflects the damping behaviour of turbulent energy through the filter. The factor α_d serves as a calibration constant and has been shown to vary between 0.69 and 0.86 for stable conditions, depending on grading and flow regime.

Critical Gradient

The stability of a geometrically open filter also depends on the critical hydraulic gradient I_C, which expresses the balance between the driving hydraulic load and the resisting forces of the filter and base materials. Following Van de Sande, 2012, the critical gradient can be expressed as:

$$i_{cr} = \left[\frac{0.06}{n_f^3 d_{15f}^{4/3}} + \frac{n_f^{5/3} d_{15f}^{1/3}}{1000\, d_{50b}^{5/3}}\right] u_{*c}^2 \tag{2.17}$$

When the hydraulic gradient within the filter remains below this critical value, the filter effectively dampens the turbulent pressure fluctuations and prevents the onset of winnowing or internal instability.

In summary, geometrically open filters function by dissipating hydraulic energy through the porous medium rather than by forming a geometrically sealed barrier. Their design thus requires an integrated assessment of the hydraulic load, filter porosity, and material interaction, as defined by the empirical and semi-empirical relationships of Wörman, Bakker & Konter, and Van de Sande.

2.4. Turbulent Hydraulic Gradient

This section elaborates on the derivation and physical interpretation of the turbulent hydraulic gradient, also referred to as the fluctuating gradient. The hydraulic gradient describes the spatial variation in hydraulic head and, when fluctuating, represents the dynamic component induced by turbulence and pressure oscillations within a porous medium.

The governing framework originates from the Navier–Stokes equation, which expresses the balance of momentum for a fluid element as:

$$\rho\left(\frac{\partial \mathbf{u}}{\partial t}+\mathbf{u}\cdot\nabla\mathbf{u}\right)=-\nabla p+\nabla\cdot\left[\mu\left(\nabla\mathbf{u}+(\nabla\mathbf{u})^{T}\right)\right]+\nabla\cdot[\lambda(\nabla\cdot\mathbf{u})\mathbf{I}]+\rho\mathbf{g} \tag{2.18}$$

where $\mathbf{u}$ is the flow velocity vector field, $\nabla\cdot\mathbf{u}$ is the divergence of the flow velocity vector, $\mathbf{u}\cdot\nabla\mathbf{u}$ is the convective acceleration, $\nabla\mathbf{u}$ is the velocity gradient tensor, $\frac{\partial\mathbf{u}}{\partial t}$ is the local acceleration, ρ is the density of the fluid, ∇p is the pressure gradient, μ is the dynamic viscosity of the fluid, $\mathbf{I}$ is the identity tensor, λ is the second viscosity, and $\rho\mathbf{g}$ is the gravity term. The left-hand side describes the temporal and convective acceleration of the fluid, whereas the right-hand side represents the pressure, viscous, and gravitational forces acting on it.

For incompressible flow in water, the continuity equation simplifies to

$$\nabla\cdot\mathbf{u}=0, \tag{2.19}$$

which implies that no volumetric compression or expansion occurs within the fluid. This assumption holds for both free-surface and porous flow under normal laboratory conditions. In porous media, where the flow paths are tortuous and confined, the macroscopic behaviour of the fluid can be described by Darcy's law, which relates the specific discharge $\mathbf{q}$ to the hydraulic gradient ∇h:

$$\mathbf{q}=-K\nabla h, \tag{2.20}$$

Combining the momentum balance (Navier–Stokes) with Darcy's law under the assumption of constant K and steady, incompressible flow yields:

$$\mathbf{u_f}=-K\nabla h \quad \text{and} \quad \nabla\cdot\mathbf{u_f}=0 \quad \Rightarrow \quad \nabla K\nabla h=0 \quad \Rightarrow \quad \nabla^2 h=0. \tag{2.21}$$

This simplification of the derivation is demonstrated by Breugem et al. (2006), employing the Whitaker volume-averaged Navier–Stokes framework (see also Whitaker (2013)). This demonstrates that the hydraulic head within a homogeneous porous medium satisfies Laplace's equation, and therefore varies smoothly and continuously in space.

If the hydraulic head is assumed to vary sinusoidally in space, for instance under wave-induced or turbulent pressure fluctuations. The corresponding hydraulic gradient is obtained by differentiation, showing that the gradient fluctuates spatially with an amplitude proportional to both the wave amplitude A and the wavenumber k. Hence, smaller-scale fluctuations (high k) result in larger instantaneous gradients.

$$h=A\sin kx \quad \Rightarrow \quad i=\frac{\partial h}{\partial x}=Ak\cos kx \tag{2.22}$$

Following Bakker et al. (1994), the total hydraulic gradient can be decomposed into a time-averaged (mean) component $\bar{i}$ and a fluctuating component i'. The mean gradient is linked to the bed shear stress τ_b, whereas the fluctuating part represents the contribution of turbulent pressure fluctuations:

$$\bar{i} = \frac{\tau_b}{\rho g h} = \frac{u_*^2}{gh}, \qquad i' = \frac{2\pi\hat{p}}{\rho g L} = \frac{2\pi\sqrt{2}}{\rho g L}\sqrt{\overline{(p')^2}}, \tag{2.23}$$

where u_* is the shear velocity, $\hat{p}$ the amplitude of the pressure fluctuations, and L the characteristic wavelength. The second expression shows that the fluctuating hydraulic gradient is directly related to the root-mean-square of the pressure fluctuations. Physically, this represents the dynamic driving force responsible for pore-scale flow oscillations and the transient energy exchange between the fluid and the porous skeleton. Together, these relationships form the theoretical basis for describing the turbulent hydraulic gradient as used in this study, linking pressure fluctuations, flow turbulence, and hydraulic energy transmission through the filter layer.

2.5. Theoretical Hypothesis

As mentioned in section 2.4 the hydraulic gradient consists of a turbulent and shear component. The turbulent component registers as pressure fluctuations (Bakker et al., 1994), while the time averaged among variables, depends on the shear velocity as show in Chezy's equation in Equation 2.2.

2.5.1. Dimensionless spectra - (Blake, 1970)

The energy of the pressure fluctuations that illustrate the turbulent hydraulic gradient component can be visualised in a pressure power spectral density. Blake, 1970 tested the turbulent pressure field above hydraulically rough walls in a controlled wind tunnel environment. These experiments demonstrated that the energy content of the pressure fluctuations, when expressed as a power spectral density (PSD), follows a characteristic distribution that depends on the ratio between the frequency of the fluctuations and the relevant hydraulic length and velocity scales. The PSD thus represents the spectral energy of the turbulent hydraulic gradient component as a function of angular frequency, where high spectral densities correspond to energetic pressure oscillations near the bed.

Blake proposed a dimensionless representation of the pressure spectra in which the measured power spectral density, $\Phi(\omega)$, is scaled using characteristic velocity, density, and length scales representative of either the outer region of the flow (governed by large scale turbulence over the water depth) or the inner region (governed by the roughness elements at the bed). The validity of this scaling approach was later confirmed experimentally by Hofland (2005). These formulations allow spectra from different flow conditions and roughness configurations to be compared on a common basis and form the foundation for the spectral framework subsequently refined by Thomas (2023). The two dimensionless forms are expressed as:

$$\frac{\Phi(\omega)}{u_0^3 c_f^2 \rho_w^2 h} \quad \text{vs.} \quad \frac{\omega h}{u_0} \quad \text{(outer)} \tag{2.24}$$

$$\frac{\Phi(\omega)}{u_*^3 \rho_w^2 d_{n50}} \quad \text{vs.} \quad \frac{\omega d_{n50}}{u_*} \quad \text{(inner)} \tag{2.25}$$

The original experimental data obtained by Blake (1970) are shown in Figure 2.2. These curves present the dimensionless spectra for both outer and inner scaling. The red fitting curve included in the figures was added later by Thomas (2023) to highlight the characteristic decay behaviour.

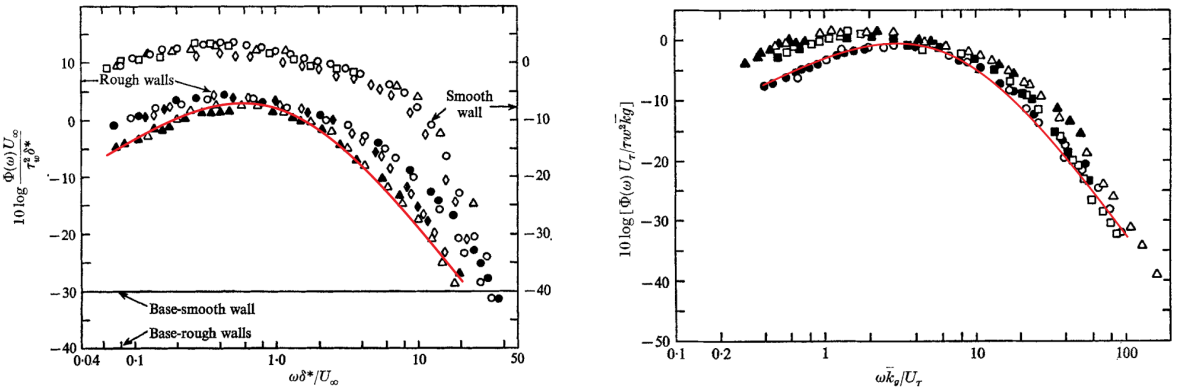

(a) The curve presenting the outer variables.

(b) The curve presenting the inner variables.

Figure 2.2: Pressure spectra of the D–L elements. Experimental data reproduced from Blake (1970); the red fitting curve was added by Thomas (2023).

These dimensionless spectral forms were subsequently replotted by Thomas (2023), as shown in Figure 2.3, to illustrate how the outer and inner scaling collapse the spectral shapes for different flow conditions. The left plot shows the collapse under outer scaling, emphasising the influence of depth scale turbulence, whereas the right plot shows the collapse under inner scaling, representing turbulence generated by interaction with roughness elements. Together, they demonstrate the two regime behaviour that underpins the spectral hypothesis applied in the present thesis.

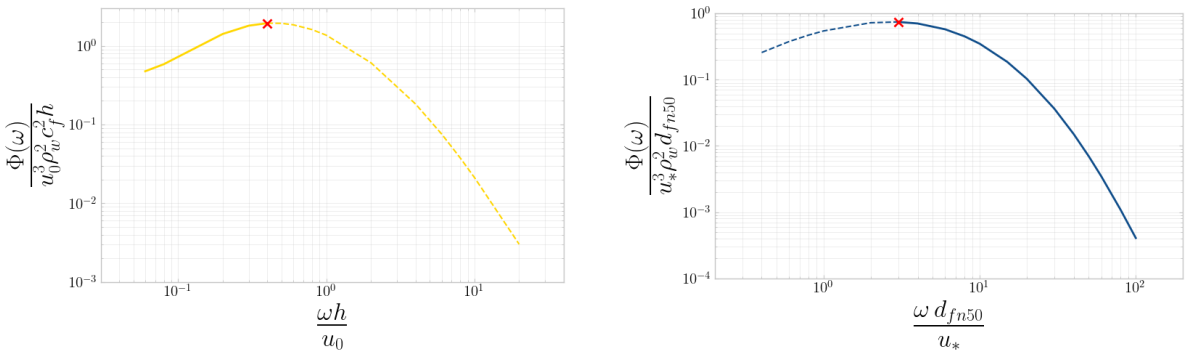

Figure 2.3: Pressure power spectral density theory of Blake (1970) plotted by Thomas (2023), scaled with outer variables (left) and with inner variables (right)

2.5.2. Convection velocity

According to Blake (1970), the convection velocity represents the characteristic speed at which pressure-producing turbulent eddies are advected downstream. The convection velocity establishes the relationship between the angular frequency ω and the wavenumber k through the fundamental transformation, as depicted in Equation 2.26.

which enables the conversion of a pressure spectrum defined in the temporal domain, $\Phi_{pp}(\omega)$, into its spatial equivalent, $\Phi_{pp}(k)$. Physically, this transformation assumes that the turbulent eddies are approximately "frozen" as they convect past the measurement location with velocity U_c. The convection velocity thus provides the link between the frequency content of the pressure fluctuations and their spatial organization along the flow direction.

In practice, the convection velocity is determined empirically from space-time correlations or cross-spectral analyses of pressure measurements, as demonstrated by Blake, 1970 for both smooth and rough boundary conditions. A distinction can be made between the *phase convection velocity*, describing the propagation of individual spectral components, and the *group convection velocity*, which characterizes the transport of energy within a narrow frequency band. For hydraulically rough boundaries, the turbulent structures interacting with the bed exhibit a significantly reduced convection speed compared to smooth-wall conditions. For the densely packed large elements roughness case (the D–L wall), Blake, 1970 reported that the broadband convection velocity asymptotically approaches approximately $0.44, U$, indicating that the pressure-producing eddies are advected at less than half the mean streamwise velocity. In the context of the present experiments, this value is adopted to represent the relationship between the bulk flow velocity and the convection velocity. The conversion is based on Taylor's frozen turbulence hypothesis, which assumes that turbulent structures are convected downstream without significant temporal evolution, as expressed in Equation 2.26.

$$U_{cp} = \frac{r_1\omega}{\alpha(r_1,\omega)} = 0.44U_\infty = 0.44\overline{U} = \frac{d\omega}{dk} \tag{2.26}$$

$$\Phi_{pp}(k) = \Phi_{pp}(\omega)\cdot 0.44\cdot u_0 = \Phi_{pp}(\omega)\cdot u_c \tag{2.27}$$

The equation for the convection velocity as given by Blake, 1970, where the r_1 is the microphone separation distance, ω is the angular frequency and α is the phase angle of the cross-spectral density.

2.6. Pressure Spectrum

This section presents the theoretical background of the pressure spectrum, describing how pressure fluctuations can be represented through their power spectral density.

Two principal approaches can be employed to determine the hydraulic gradient spectrum. The indirect approach derives the gradient spectrum from the pressure spectrum, which is initially expressed in the temporal domain. Through the application of energy conservation principles and the conversion of pressure fluctuations into hydraulic head, the temporal spectrum can be transformed into its spatial equivalent, yielding the corresponding gradient spectrum. The direct approach, on the other hand, is based on measured pressure differences between two points aligned with the flow direction. This method inherently provides the hydraulic head variation over a defined spatial distance, thereby allowing the gradient spectrum to be obtained directly as a function of the angular wavenumber. The following section elaborates on the theoretical basis for converting the pressure spectrum from the temporal to the spatial domain.

2.6.1. Indirect - (Thomas, 2023)

Using the wave spectra as explained in section 2.5, the variance of the pressure amplitude per frequency is given as $\Phi^f_{pp}(f) \quad [\mathrm{Pa}^2/\mathrm{Hz}]$. The power spectral density (PSD) in frequency is in a temporal scale, however the hydraulic gradient is on a spatial scale $[m]/[m]$, as given in Equation 2.22. The conversion of the temporal to spatial, can be done as ocean waves using the dispersion relation, however the turbulent pressure waves do not follow the hydrostatic properties that ocean waves follow. Therefore the conversion from temporal to spatial goes through the convection velocity as described by Blake, 1970. The dispersion relation and the convection method use the angular frequency (ω) to convert to angular wavenumber (k). To define angular frequency $\omega = 2\pi f$ and convert to ω-basis via conservation of variance:

$$\Phi^{\omega}_{pp}(\omega)\, d\omega = \Phi^{f}_{pp}(f)\, df \quad \Rightarrow \quad \Phi^{\omega}_{pp}(\omega) = \frac{\Phi^{f}_{pp}(f)}{2\pi}\,. \tag{2.28}$$

Next to convert the angular frequency to angular wavenumber the conservation of energy is used, as in Equation 2.29. This realises the temporal to spatial translation. Using the change of variables,

$$\int \Phi^{k}_{pp}(k)\, dk = \int \Phi^{\omega}_{pp}\big(\omega(k)\big)\, d\omega \quad \Rightarrow \quad \boxed{\Phi^{k}_{pp}(k) = \Phi^{\omega}_{pp}\big(\omega(k)\big)\,\frac{d\omega}{dk}} \qquad [\mathrm{Pa}^2 \cdot \mathrm{m}]. \tag{2.29}$$

The turbulent pressure fluctuations generated within the boundary layer do not follow hydrostatic relations, as is the case for wave-induced motion, but are instead governed by the interaction between the turbulent flow and the bed roughness. Consequently, these fluctuations are primarily a function of the local flow velocity rather than the water depth. To relate the temporal variability of the pressure signal to its spatial structure, a convection velocity is used, as described in subsection 2.5.2. From this point onward, the theoretical framework developed by Thomas, 2023 serves as the foundation. However, several modifications and additional derivations are introduced in this work to obtain the hydraulic gradient through an indirect formulation.

Example theory based on Thomas (2023)

The input parameters in this example reflect the estimated upper limits of the test facility. From the chosen outer variables $(u_0,\, h)$, the inner variables $(u_*,\, d_{n50})$ follow directly via the Chézy relation (2.3) and the shear-velocity (2.4). The dimensionless peak locations of the outer and inner spectra, taken directly from the universal curves of Blake (1970) as reproduced by Thomas (2023), are listed in Table 2.1. These peaks represent the dominant turbulent time scales associated with flow-depth and roughness-scale motions.

Table 2.1: Coordinates of the dimensionless spectral maxima for the outer and inner regions, directly from Blake (1970), derived by Thomas (2023).

Spectrum	Peak location (dimensionless)	Peak value (dimensionless)
Outer spectrum	$\dfrac{\omega h}{u_0} = 0.40$	$\Phi = 1.94$
Inner spectrum	$\dfrac{\omega d_{n50}}{u_*} = 3.00$	$\Phi = 0.7466$

These peak coordinates are universal and do not depend on the flow conditions of this study. Only after selecting representative values for u_0, h, c_f and d_{n50},and computing u_*, can the dimensional forms of the outer and inner spectra be constructed.

To construct the dimensional spectra together, the universal dimensionless curves of Blake (1970) are used. Following the notation introduced by Thomas (2023), the symbols F and G serve only as placeholders to represent these empirically obtained curves. They do *not* originate from Blake as analytical functions, but simply denote the interpolated shapes of the inner- and outer-scaled spectra. When evaluated at the appropriate dimensionless groups,

$$G\left(\frac{\omega h}{u_0}\right), \qquad F\left(\frac{\omega d_{n50}}{u_*}\right),$$

they describe how the turbulent pressure-fluctuation energy is distributed across frequencies in the outer and inner regions. Reintroducing the physical scales yields the dimensional spectra:

$$\Phi_{pp,\mathrm{out}}(\omega) = u_0^3 c_f^2 \rho_w^2 h \; G\left(\frac{\omega h}{u_0}\right), \qquad \Phi_{pp,\mathrm{in}}(\omega) = u_*^3 c_f^2 \rho_w^2 d_{n50} \; F\left(\frac{\omega d_{n50}}{u_*}\right).$$

Figure 2.4 shows how these two dimensional spectra are combined. In the left panel, both spectra are evaluated using the same flow parameters, ensuring that they describe the same physical pressure-fluctuation signal and can therefore be plotted on identical axes. The two branches are joined by interpolating between their universal peak values; the dashed segment merely provides continuity in log–log space and does not represent a physical scaling law.

The middle panel shows the resulting combined temporal spectrum $\Phi_{pp}(\omega)$, representing the full distribution of pressure-fluctuation energy at a fixed point. Finally, the right panel converts this temporal spectrum to a spatial spectrum using the convection-velocity assumption (Equation 2.29) with $u_c = 0.44\,\overline{u}$, yielding the wavenumber spectrum $\Phi_{pp}(k)$ required for analysing damping within the granular filter layer.

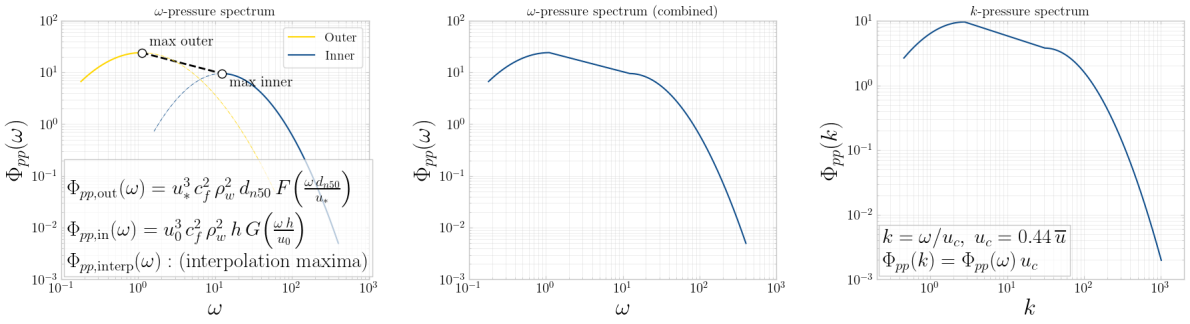

Figure 2.4: Construction of the dimensional pressure spectrum following Thomas (2023). Left: outer- and inner-scaled spectra based on Blake (1970). Middle: combined temporal spectrum. Right: conversion to spatial spectrum.

2.6.2. Waves - Indirect

The hypothesis of The relation between ω and k for waves is depicted in the dispersion relation, in Equation 2.30 and Equation 2.31, for linear gravity waves of finite and constant depth h.

$$\omega^2 = g\,k\,\tanh(kh) \qquad k = \frac{\omega^2}{g\tanh kh}, \tag{2.30}$$

$$\frac{d\omega}{dk} = \frac{g\tanh(kh) + gkh\,\mathrm{sech}^2(kh)}{2\omega} \equiv c_g(k,h). \tag{2.31}$$

The angular wavenumber for each value of the angular frequency can be calculated using iteration as seen in Equation 2.30.

2.7. Gradient Spectrum

This section focusses on the translation of pressure spectra to gradient spectra, in this thesis two ways are considered to obtain the gradient spectrum as mentioned before. First the method to go from a pressure spectrum to gradient spectrum is shown in subsection 2.7.1. The theoretical substantiation of the direct method, using directly measured differences in pressure fluctuations, is elaborated in subsection 2.7.2.

2.7.1. Current - Indirect (Thomas, 2023)

Let ρ be water density and g gravity. Define the (dimensioned) transfer gains:

$$p(x) = \sum_{n=1}^{N} a_n\,\sin(k_n x) \tag{2.32}$$

$$\Delta k\,\Phi_{pp}(k_n) = \tfrac{1}{2}a_n^2 \tag{2.33}$$

$$i'(x) = \sum_{n=1}^{N} a_{i,n}\,\cos(k_n x) \qquad \text{with:} \qquad a_{i,n} = \frac{k_n a_n}{\rho_w g} \tag{2.34}$$

$$\Delta k\,\Phi_{ii}(k_i) = \tfrac{1}{2}a_i^2 \tag{2.35}$$

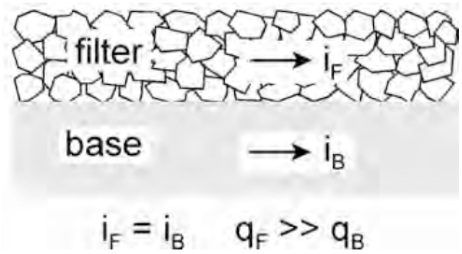

Figure 2.5: Parallel flow in granular filter, (Schiereck and Verhagen, 2019)

For the horizontal consideration (parallel to the filter) of the hydraulic gradient, the conversion term (in Equation 2.36 depicted as T) is what remains when considering Equations 2.32 to 2.35. This is the conversion term of the gradient is what remains when considering the pressure amplitude in relation to the gradient amplitude, as seen in Equation 2.34. When using this term to substitute for the pressure amplitude and when considering the pressure PSD, the gradient PSD can be obtained using Equation 2.36.

$$\boxed{\Phi_{i_x i_x}^{(\text{indirect})}(k) = \left|T_x(k)\right|^2 \Phi_{pp}^k(k) = \left[\frac{k}{\rho g}\right]^2 \Phi_{pp}^k(k)} \qquad [-]. \tag{2.36}$$

2.7.2. Direct Method

The direct determination of the hydraulic gradient is based on the spatial pressure difference measured between two synchronised sensors positioned along the flow direction. According to Equation 2.37, the instantaneous hydraulic gradient is obtained from the pressure gradient divided by the hydrostatic term ρg:

$$i = \frac{dh}{dx} = \frac{1}{\rho g}\frac{dp}{dx} = \frac{ak}{\rho g}\cos(kx), \tag{2.37}$$

This expression directly links the pressure variation over distance to the local hydraulic gradient and does not rely on any theoretical assumptions about the turbulent structure of the flow.

Waves and Currents

In practice, the direct horizontal gradient is obtained from two aligned pressure sensors separated by a known horizontal distance Δx. The instantaneous gradient signal is determined from the finite pressure difference between both sensors:

$$i_x^{\mathrm{FD}}(t) = \frac{p_2(t) - p_1(t)}{\rho g\, \Delta x}\,. \tag{2.38}$$

This results in a continuous time series of the local hydraulic gradient $i_x^{\mathrm{FD}}(t)$, which reflects both the mean and the fluctuating (turbulent or wave-induced) components of the pressure field. By performing a spectral analysis of this signal, the PSD of the gradient can be obtained, describing how the variance of the gradient is distributed across frequencies.

To enable comparison with theoretical formulations that are expressed in the wavenumber domain, the temporal PSD $\Phi^f_{i_x i_x}(f)$ must be transformed to an equivalent wavenumber spectrum. The transformation involves several intermediate steps. First, the frequency-based spectrum is converted to an angular frequency spectrum:

$$\Phi^{\omega}_{i_x i_x}(\omega) = \frac{\Phi^f_{i_x i_x}(f)}{2\pi}, \tag{2.39}$$

after which the spectrum is mapped to the wavenumber domain using the appropriate physical relation between angular frequency ω and wavenumber k:

$$\Phi^{k,\mathrm{FD}}_{i_x i_x}(k) = \Phi^{\omega}_{i_x i_x}\big(\omega(k)\big)\,\frac{d\omega}{dk}. \tag{2.40}$$

The frequency–wavenumber relation differs for waves and steady currents. For oscillatory wave motion, the transformation is based on the linear wave dispersion relation from Equation 2.30. In contrast, for steady current flow, the spectral conversion follows the hypothesis of Blake, 1970, which assumes that turbulent pressure structures are advected downstream with a mean convection velocity U_c, derived from Equation 2.26.

Hence, while both approaches yield a wavenumber-based spectrum of the hydraulic gradient, the governing transformation mechanism differs: wave-dominated conditions rely on dispersion, whereas current-dominated conditions rely on convection. This distinction is crucial when comparing the directly measured spectra with theoretical or indirect (model-based) predictions, as it determines the scaling between temporal and spatial representations of the turbulent energy.

2.8. Damping

The damping of pressure and gradient fluctuations within a permeable layer is a direct consequence of energy dissipation as turbulent pressure waves propagate through the porous medium. The proposed hypothesis by Thomas (2023) describes this behaviour as a function of the wavenumber k and the layer thickness D_f, both derived from the gradient formulation and the principles of linear wave theory (Dean & Dalrymple, 1991).

The instantaneous fluctuating hydraulic gradient can be expressed as a superposition of harmonic components of varying wavenumbers:

$$i'(x,z) = \sum_{n=1}^{N} \frac{a_{i,n}\,\cos(k_n x + \varphi)}{\cosh(k_n z)}, \tag{2.41}$$

where φ is the random phase. Within a porous filter layer, these harmonic components experience a reduction in amplitude with depth due to frictional losses and phase attenuation. The resulting damping can therefore be described as a function of wavenumber and layer thickness. Assuming the same exponential decay behaviour as for linear wave propagation, the relationship between the gradient spectra at the top and bottom of the filter layer becomes:

$$\Phi_{ii}(k, z=-D_f) = \frac{\Phi_{ii}(k, z=0)}{\cosh(kD_f)^2}, \qquad K_{D,\,m_0} = \frac{1}{\cosh(kD_f)^2}, \qquad K_{D,\,\sigma} = \frac{1}{\cosh(kD_f)}, \tag{2.42}$$

where $\Phi_{ii}(k,z)$ is the gradient power spectral density at depth z, and K_D is the dimensionless damping coefficient. The factor $K_{D,\,m_0}$ represents the damping of spectral energy (i.e., variance or zeroth moment of the spectrum), while $K_{D,\,\sigma}$ corresponds to the damping of the standard deviation of the fluctuating hydraulic gradient.

This formulation implies that higher wavenumber components (shorter turbulent structures) experience stronger attenuation with depth, while long-wavelength fluctuations penetrate more deeply into the filter layer. Consequently, the damping behaviour acts as a frequency-dependent filter, controlling the extent to which turbulent pressure fluctuations at the bed surface influence the flow within the porous layer.

2.9. Loading - Fluctuating Hydraulic gradient

The study by Wolters and Van Gent (2012) showed that the bed material transport can be described as a function of the ratio $i_{2\%}/i_{\mathrm{cr}}$. To assess the structural integrity of the bed material, both the hydraulic load ($i_{2\%}$) and the resistance (i_{cr}) must be known. The critical gradient for granular filters with a granular base follows from Equation 2.17, while Akerboom (2024) provides experimentally determined critical gradients for open filters on several types of natural geotextiles. With the resistance i_{cr} known, the remaining task is to determine the hydraulic load $i_{2\%}$.

Following the analysis of Thomas (2023), the total hydraulic gradient inside porous filter layers can be written as described in Equation 1.1, where $\bar{i}$ is the mean gradient and i' represents the turbulent fluctuating component. Thomas shows that the variance of i is overwhelmingly dominated by i', meaning that the instantaneous hydraulic loading acting on the porous material is controlled almost entirely by the fluctuating gradient. Therefore, the quantity of interest for the hydraulic load becomes the highest two-percentile of the fluctuating gradient, denoted $i'_{2\%}$.

According to Hofland (2005), the *pressure fluctuations* p' in the near-bed region are approximately Gaussian. However, the *magnitude of the fluctuating hydraulic gradient*, defined as

$$i' = \frac{|\nabla p'|}{\rho g}, \tag{2.43}$$

is a non-negative quantity and exhibits a positively skewed probability density function with an exponential-type tail. Hofland does not explicitly classify this distribution as Rayleigh, but the shape of the reported PDFs displays clear Rayleigh-like characteristics. A similar distributional shape appears in the fluctuating gradient statistics of Thomas (2023), as shown in Figure 2.6.

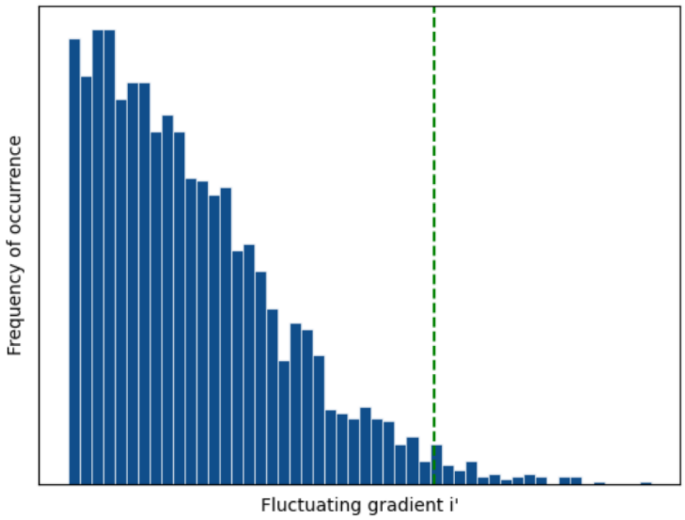

Figure 2.6: PDF of the fluctuating gradient (Thomas, 2023)

Based on these observations, this thesis assumes that the probability density function of i' is well represented by a Rayleigh distribution. Under this assumption, the two-percentile value of the fluctuating gradient becomes

$$i'_{2\%} = \sigma\sqrt{-2\ln(1-p)} \approx 2.797\,\sigma \tag{2.44}$$

where p is the chance of exceedance, when looking at the highest 2% the value of p is 0.98, σ is the standard deviation of i', obtained via Parseval's theorem from the wavenumber spectrum.

3

Methodology

This chapter shows the test setup that are used in the experiments. The experiments have been conducted in the Sediment Flume at the Waterlab, TU Delft. For this experiment the pressure fluctuations are obtained using pressure sensor arrays.

3.1. Test Equipment

This section highlights the equipment required to carry out the experimental program. Once the equipment list has been established, an inventory should be conducted to assess which materials and devices are already available in the laboratory. Any missing or insufficient equipment must then be identified and, if necessary, acquired to ensure the experiments can be performed as planned.

3.1.1. Sediment Flume

The dimensions of the sediment flume are as follows: the length is 39 meter, the width 0.76 meter and the height is 0.85 meter, the walls of the flume have a board with an extra 0.20 meter height, to prevent possible overflow due to waves. The pump used for this flume has an absolute maximum discharge of $500l/s$, considering the safety factor that states that the pump cannot exceed 70% of its pumping capacity, leaves the maximum safe discharge at $350l/s$. Using the discharge and the cross-section of the flume gives an overall flow velocity of $\overline{u} = 0.79[m/s]$ at the maximal usable water height.

3.1.2. Flume Layout

The layout of the flume consists of a false floor with a height of 8 cm, a length of 15 meters and covers the complete width of the flume. At the start of the false floor (towards the outlet of the pump) the false floor has a 1:3 slope, at the end of the false floor (towards the inlet of the pump) there is a 1:1 slope. The False floor is positioned towards the end of the flume, there is 5 meters between the Rehbock weir and the end of the false floor. The sensors are positioned at 10 meters from the weir, making the influence of the elevation due to the floor and the backwater curve of the weir negligible. The false floor layout and positioning of the pressure sensors are depicted in Figure 3.1. The false floor reduces the disturbances in the flow caused by the sensor tubes.

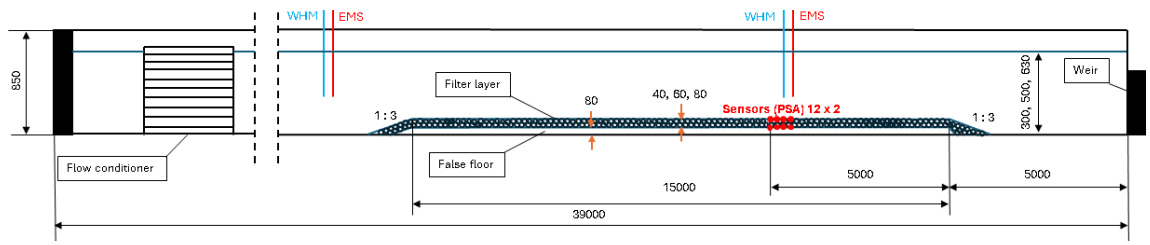

Figure 3.1: Setup for current loading (side view)

For the wave experiments, the experimental setup was modified: the breakwater was installed at the downstream end of the flume, and the upstream flow conditioner was removed to allow the generation of undisturbed wave conditions. The alterations are visible when comparing Figures 3.1 & 3.2.

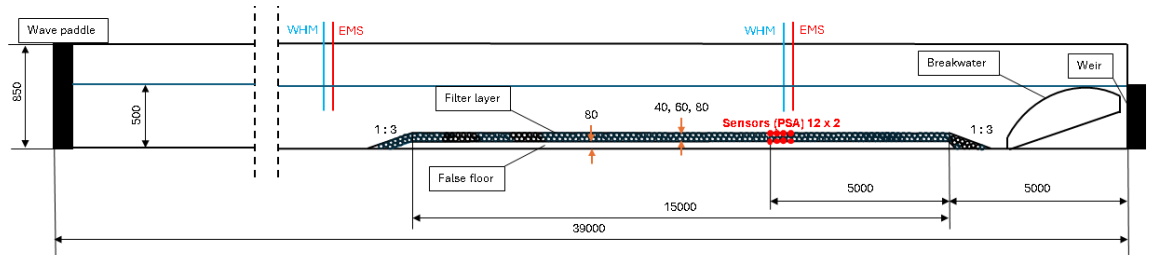

Figure 3.2: Setup for wave loading (side view)

3.1.3. Flow conditioner

The flow conditioners is a honeycomb-like structure that settles the flow of the flume. In the case of the experiments the flow conditioner is made up of pvc tubes. The purpose is to reduce the large vortices caused by the flow of the pump and the large bend in the pipe. The structure is placed shortly after the outlet of the pump.

Figure 3.3: Flow conditioner, front view (left), top view (right)

3.1.4. Obstacle

The obstacle was designed to create flow interference and a temporary velocity increase, thereby generating more intense turbulence in its wake. It blocked approximately 20% of the flow area and consisted of five vertical rectangular columns, each 3 cm wide, spaced 12 cm apart, with 6 cm clearance to the flume walls. The wall-mounted beams shown in the centre of Figure 3.4 contained holes at 1 m and 2 m upstream of the pressure sensor array, ensuring identical positioning across test runs. The corresponding test variables and programme are listed in Appendix F.

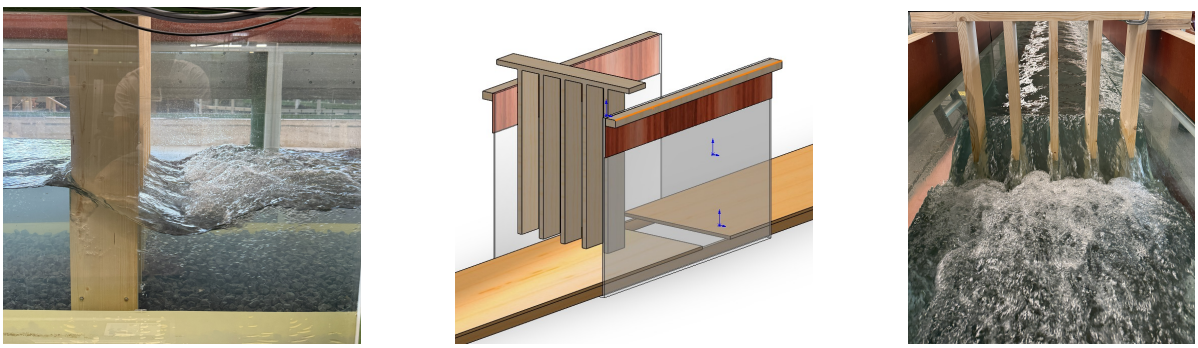

Figure 3.4: Obstacle side- (left), and front view (left) and sketch (middle, courtesy of Arie van der Vlies)

3.2. Material properties

This section touches upon the properties of the used filter material, how they are obtained and what their influence on the tests are. The significant properties consist of the density of the material, the grain size distribution, the nominal diameter of the rocks, the thickness of the rock layers that have been used for the tests, and finally the porosity of the test experiment.

3.2.1. Filter material

The filter consists of basalt riprap (dimensions in subsections 3.2.2 & 3.2.3). Basalt is preferred because its relatively high particle density improves stability, its rough surface enhances interlock, and it is widely available; typical values lie between 2.5 and 3.1 t/m³ CIRIA et al., 2007. The density of the specific basalt used was determined experimentally using Archimedes' principle, which states that a body wholly or partially submerged in a fluid experiences an upward buoyant force equal to the weight of the displaced fluid. Practically, a sample of 350 stones was first weighed dry on a scale to obtain the sample mass. Then a bucket of water was tared on the same scale, and the entire sample, held in a fishnet so that all stones were fully submerged yet did not touch the bucket, was lowered into the water. The increase in the scale reading equals the weight of the displaced water and therefore gives the displaced-water mass. Dividing this by the water density yields the submerged volume of the stone sample. The stone density follows as the dry sample mass divided by this displaced volume.

Using this procedure, the basalt density for the tests was found to be **2855 kg/m³**.

3.2.2. Filter Grainsize

In this subsection, the required grain size is first calculated based on the experimental boundary conditions, after which the actual grain size is determined by measuring the obtained rock materials.

Calculated grain size

In this section, the grain size is determined using multiple Boundary conditions, the Shields equation, Froude number, Maximal discharge capacity, dimensions of the Flume and the Reynolds Number in Porous Media.

The nominal grain size d_{n50} of the filter material was determined using a boundary-based design approach. This combines hydraulic and sediment stability criteria to ensure that the filter layer remains stable under all flow conditions in the flume. The method considers the following constraints: (1) flume dimensions and discharge capacity, (2) particle stability according to the Shields criterion, (3) subcritical flow regime, and (4) turbulence through the porous medium.

Table 3.1: Boundary conditions governing the design of d_{n50}.

Condition	Equation	Criterion
Flume dimensions	$w = 0.76\,\mathrm{m},\ h < 0.72\,\mathrm{m}$	Physical limit
Max. discharge	$Q_{\max} = 0.35\,\mathrm{m}^3/\mathrm{s}$	Operational
Shields stability	$\psi = u_*^2/(\Delta g d_{50}) < 0.03$	No particle motion
Froude number	$Fr = u/\sqrt{gh} < 0.75$	Subcritical flow
Porous turbulence	$Re_p = u_f D_{n50}/(n\nu) > 300$	Turbulent regime

The procedure iteratively solves for d_{n50} by combining the Chezy equation, Shields stability criterion, and the Forchheimer relation for porous flow. Input parameters include $\rho_w = 1000\,\mathrm{kg/m^3}$, $\rho_s = 2850\,\mathrm{kg/m^3}$, $\Delta = 1.85$, $n = 0.46$, and $g = 9.81\,\mathrm{m/s^2}$. The resulting d_{n50} provides a hydraulically stable and fully turbulent filter layer, preventing particle movement or clogging within the flume setup.

Detailed derivations and the full boundary-condition formulations are provided in Appendix D.

Determined grain size

The required grainsize has been calculated in subsection 3.2.2, using the boundary conditions. In this subsection is the nominal grian size of the acquired materials determined, through physical measurements. The equation for the nominal diameter is given by Schiereck and Verhagen, 2019:

$$d_{n50} = d_{50} * 0.84 \tag{3.1}$$

Using the values obtained in subsection 3.2.2 the d_{50} = 1.73 cm, therefore the nominal diameter is: d_{n50} = **1.455 cm**.

3.2.3. Grainsize distribution

The grainsize distribution of the filter has been determined, by weighing every rock separately and knowing the density form obtained in subsection 3.2.1. These measurements gave the nominal diameter of every separate rock by Equation 3.2. Next the nominal diameter is converted to the diameter, using the shape factor (shown in Table 3.3.

$$d_n = \sqrt[3]{\frac{W}{\rho}} \tag{3.2}$$

Next a cumulative density function has been drawn up as seen in Figure 3.5.

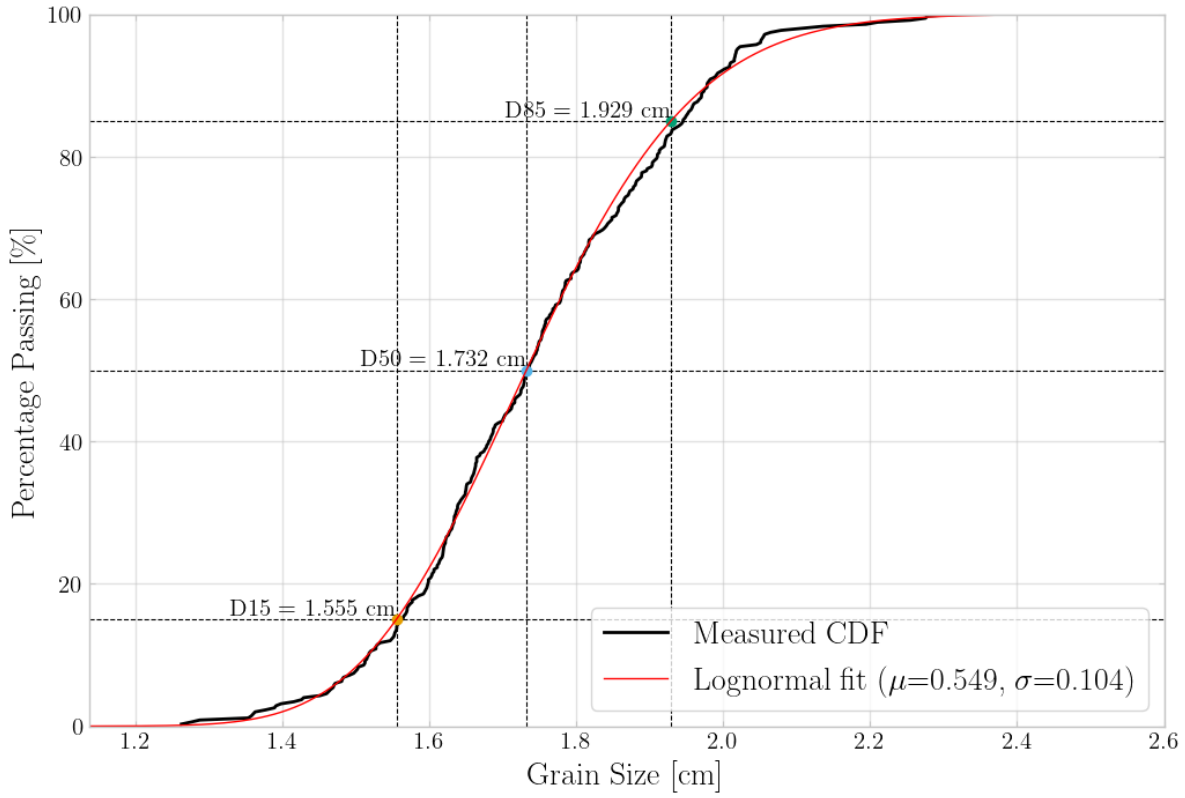

Figure 3.5: Grain size distribution(CDF) with lognormal fit

3.2.4. Filter thickness

For the layer thickness are some rules of thumb that can be used for an initial guess of the layer thickness. The layer thickness should comply with two rules, The thickness should be larger than the largest stone in the filter grading $(d_{100} > D_f)$, also the layer should be 1.5 times larger than the median grain size $(1.5 \cdot d_{50} > D_f)$, as stated by Robinson et al., 1998 after Brown and Clyde, 1989. These rules only give guidelines for the minimal thickness of the layer. An estimation of the filter thickness will be derived from the theory of Thomas, 2023, whilst considering the minimal thickness as stated above.

The hypothesis derived from the theory of Thomas, 2023, combined with the guidelines stated before, Table 3.2 shows the filter thicknesses according to the guidelines and the hypothesis and the right part of the table shows the picked filter thicknesses.

Guideline	D_f [cm]	Week	D_f [cm]
$D_f > d_{100}$	2.4	1	0
$D_f > d_{50} \cdot 1.5$	2.6	2	4
		3	6
		4	8

Table 3.2: Layer thickness

3.2.5. Porosity

As described in subsection 2.1.2, the porosity has a large influence on the filter velocity, derived using the Forchheimer equation, where the forchheimer coefficients directly depend on the porosity as shown in(Equation 2.7) and has influence on the Porous Reynolds number, shown in Equation 2.9.The porosity has been determined in two ways one is by physically measuring the porosity, described in Equation 3.2.5 and another way is with an equation using the grainsize distribution.

Theoretical determined Porosity

The theoretical approximation of the porosity uses the formulae (Equations 3.3 to 3.5) given by CIRIA et al., 2007 and the grainsize distribution, given in subsection 3.2.3.

Table 3.3: Input parameters for porosity calculation.

Symbol	Description	Value
d_{n50}	Nominal diameter (median)	$0.01455\ \mathrm{m}$
y_{NUL}	Nominal Upper Limit fraction passing	0.85
y_{NLL}	Nominal Lower Limit fraction passing	0.15
d_{15}	Nominal lower-limit diameter	$0.01555\ \mathrm{m}$
d_{85}	Nominal upper-limit diameter	$0.01929\ \mathrm{m}$
F_s	Shape factor (grading stones)	0.84
ρ_s	Particle density (rock)	ρ_s
e_0	Single-size void ratio (Mechanically crushed)	0.94

Grading masses.

$$M_{\mathrm{NUL}} = \left(d_{85} F_s\right)^3 \rho_s, \qquad M_{\mathrm{NLL}} = \left(d_{15} F_s\right)^3 \rho_s. \tag{3.3}$$

RRM exponents.

$$\text{(i)}\ \Lambda = \frac{\ln\!\left(1 - y_{\mathrm{NUL}}\right)}{\ln\!\left(1 - y_{\mathrm{NLL}}\right)}, \tag{3.4a}$$

$$\text{(ii)}\ n_{\mathrm{RRM}} = \frac{\ln \Lambda}{\ln\!\left(\dfrac{M_{\mathrm{NUL}}}{M_{\mathrm{NLL}}}\right)}, \tag{3.4b}$$

$$\text{(iii)}\ n_{\mathrm{RRD}} = 3\, n_{\mathrm{RRM}}. \tag{3.4c}$$

Void ratio and porosity. Equation 3.5a slightly differs from the Rockmanual (CIRIA et al., 2007), for θ has to be given in degrees, therefore the conversion from radians to degrees is needed. With n_{RRD} from (3.4), define

$$\theta_{\mathrm{deg}} = \arctan\!\left(0.645\, n_{\mathrm{RRD}}\right) \cdot \frac{180}{\pi}, \tag{3.5a}$$

$$e = \frac{e_0}{90}\, \theta_{\mathrm{deg}}, \tag{3.5b}$$

$$n_v = \frac{e}{1 + e}. \tag{3.5c}$$

Here, e is the void ratio and n_v is the bulk-placed porosity (volume fraction). θ_{deg} should give the angle in degrees, therefore this equation converts the radians to degrees in Equation 3.5a, this conversion is not included in the Rock Manual.

The input resulted in a bulk-placed porosity of **46.21%**.

Physical determined Porosity

The physically obtained porosity, has been done by measuring the total volume of the pores with, by filling the voids with water and weighing the added water weight. First a bucket has been placed on a scale and is filled to the rim with water, knowing the density of water, the volume of the bucket can be accurately determined. Filling a bucket can cause the bucket to entrap more liquid than is actually the volume as a consequence of surface tension and thus a convex meniscus. However, in a bucket with a volume of 6 L the influence of that phenomenon is negligible.

Next the bucket is filled completely with the granular material, which consists of multiple samples from different places in the rock storage, to get the most accurate distribution of the granular material. The rocks are filled in a way that a little mountain forms on top of the bucket, so no unnecessary voids are formed at the top. This bucket again is placed on a scale, which is set to zero. Lastly the bucket is again filled to the rim with water, so all the voids fill with water. Now the weight that is given by the scale is the weight of the water and knowing the density of the water, the volume of the water and thus the voids is determined.

$$n = \frac{V_v}{V_T} \tag{3.6}$$

The porosity equation of the porosity is the ratio between the volume of the voids and the total volume, as given by Equation 3.6. The volume of the voids will not perfectly represent the porosity in the Flume, because the bucket has as smaller volume than the complete experimental setup. Therefore, the small test is more influenced by the wall, due to the smooth surface, leading to larger voids and thus a larger void ratio.

A total volume of 6 liters and a void volume of 2.77 liters gave a void ratio of **46.16%**.

Summary Porosity

The physically obtained porosity and the theoretically obtained void ratio are very similar, therefore it can be said that the void ratio is **46.2%**.

3.3. Pressure sensors

The measuring equipment used for the experiments need to be able to measure the occurring pressure fluctuations at both interfaces, the base/filter and top of filter. These fluctuations have to be measured with pressure sensor arrays, which will be able to detect the pressure fluctuations due to the occurring local turbulence.

The number of pressure sensors required depends on the specifics of the experimental setup. Sensors are always placed in pairs in order to measure the pressure difference (Δp) across a small known distance (Δx). Increasing the number of sensors improves the resolution of the measurements and allows for a more accurate assessment of the pressure wavelength (λ) and corresponding wavenumber (k).

To create a pressure sensor array that can measure the pressure differences in the spatial domain, the wave length domain needs to be determined. The smallest wavelength depends on the dimensions of the sensor and the constructibility of the array. Therefore the smallest wavelength is 4 cm.

Since this study focuses on capturing the fluctuating gradient at both the top and bottom interfaces of the filter layer, sensor arrays are required at both locations. To minimize experimental uncertainty, a duplicate array is installed downstream. If lateral (y-direction) variations are to be captured as well, an additional set of sensor arrays is necessary. In total, this results in 48 pressure sensors being used, excluding any spares kept on hand for replacements.

3.3.1. Sealed sensor

To minimize interference of the Pressure Sensor Array (PSA) with the surrounding porous media, a sealed pressure sensor configuration was adopted. Unlike vented sensors, sealed sensors do not contain a reference tube that must remain in contact with the atmosphere. Instead, they consist solely of a pressure-sensitive diaphragm enclosed in a watertight casing, connected via a cable for data transmission. The cables of both the upper and lower PSA are routed beneath the false floor and along the sidewall of the flume to minimize hydrodynamic disturbances. For the upper PSA, the cables pass through the filter layer before reaching the underside of the false floor, as illustrated in Figure 3.8b. To reduce the number of penetrations through the filter and false floor, a single cable per sensor is preferred—hence the choice for a sealed configuration.

Prior to the main experiments, a series of reliability tests were conducted to verify the performance of the sealed sensors. These tests are described in detail in Appendix G. One recommendation from these preliminary tests was to include a thermometer in the flume to compensate for possible temperature-induced drift, as thermal variations can cause gradual offset shifts in sealed sensors. However, this was deemed unnecessary for the present study, since each test sequence lasted no longer than 20 minutes and the sensors were re-normalized at the start of each segment following the procedure outlined in subsection 4.3.4.

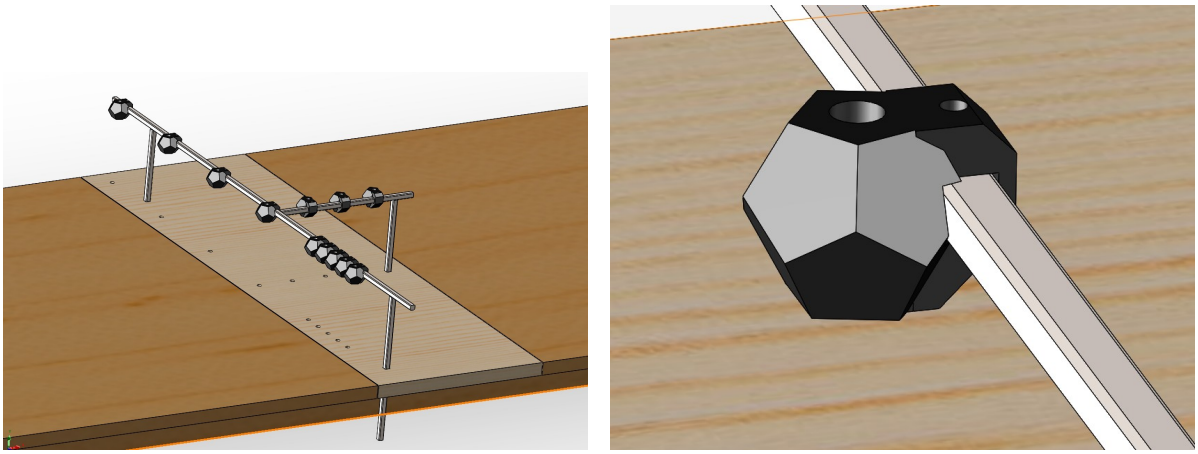

Figure 3.6: Sketch - Upper pressure sensor array (left) and detail of sealed sensor casing (right)

Figure 3.6 shows, on the left, a schematic of the sensor array and, on the right, a detail of the sensor casing. The sensors are housed in a custom casing designed with multiple purposes: (I) to mimic the irregular shape of the surrounding rock material, (II) to enable mounting on a frame ensuring equal elevation of all sensors, and (III) to guarantee watertight protection. The sensors are embedded in the casing and the remaining voids are filled with epoxy to achieve complete sealing. The frame height can be precisely adjusted by setting the three supporting columns to identical elevations.

The sealed sensor itself is shaped as a dodecahedron, as illustrated in the right-hand panel of Figure 3.6. This irregular geometry was chosen to approximate the natural form of the filter rocks, while its volume was adjusted to match the nominal stone diameter (D_{n50}). The irregular shape promotes the formation of natural voids between the surrounding rocks and the sensors, ensuring representative local flow conditions. Moreover, the geometry allows the centre-to-centre distance between sensors to correspond accurately to the spacing defined in Figure 3.8a. The length of the edge (a) can be traced back to the Volume calculation of the dodecahedron and with that the nominal diameter, as shown in Equation 3.7.

$$V_{50} = \frac{15 + 7\sqrt{5}}{4} \cdot a_{50}^3 = d_{n50}^3 \tag{3.7}$$

3.3.2. Unsealed sensor

The unsealed sensors are equipped with two separate tubes: one for electrical wiring and one serving as a reference to the atmosphere. These sensors measure the pressure difference between the atmospheric pressure (via the reference tube) and the absolute pressure at the sensor inlet, which in this case corresponds to the submerged location within the flume. The unsealed configuration was applied for the lower Pressure Sensor Array (PSA), where the sensors are mounted to the underside of the false floor, as illustrated in Figure 3.7 and Figure 3.8b.

Figure 3.7: Lower Pressure Sensor Array underside - with reference tubes

3.3.3. Literature pressure sensors

To substantiate the test setup drawn up in chapter 3, prior papers investigating pressure fluctuations according to physical modelling have been looked into.

The wind tunnel experiments by Hudy et al., 2003, investigates the spatial and temporal character of the surface-pressure field within a separating/reattaching flow region. Therefore it uses a continuous pressure sensor array, in contrast to the study conducted by Cherry et al., 1984, which is often cited, where a two-point unsteady surface pressure measurement is performed. The choice to implement a continuous pressure sensor array, in stead of a two point configuration, allows to obtain a more detailed picture of the spatial structure of the cross correlation, according to Hudy et al., 2003.

3.3.4. Pressure Sensor Array

Below, Figure 3.8a and Figure 3.8b present the top and side views, respectively, of the pressure-sensor array. The top view illustrates the lateral arrangement of the sensors, indicated by the red circular markers. One additional sensor, positioned just outside the photographed frame, is located to the left of the leftmost visible marker, with spacing of 12.5 cm. The flow direction is indicated by the red arrow together with the symbols for flow velocity and discharge (U, Q). The coordinate axes shown in white define the x–y plane, and this orientation is used consistently throughout the thesis.

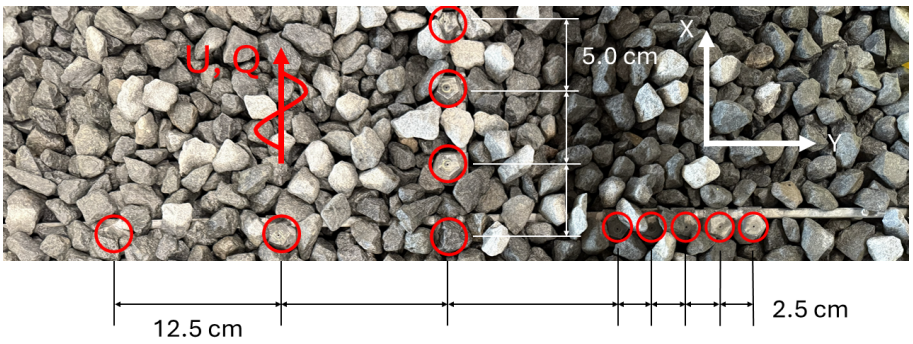

(a) Top view of the sensors embedded in the rock layer.

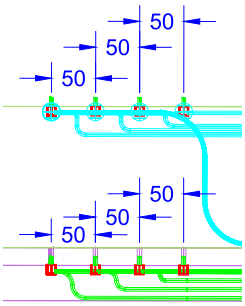

(b) Side view of the sensor detail.

Figure 3.8: Sensor configuration showing (a) the top view with lateral positioning of the pressure sensors and (b) the side view illustrating their vertical placement within the granular layer.

The spacing of the sensor array was determined based on the incremental distance steps that can be achieved between individual sensors. In the lateral direction, two basic step sizes are available: 12.5 cm and 2.5 cm, as visible in Figure 3.8a. By combining these intervals, any desired spacing in increments of 2.5 cm up to a total distance of 60 cm can be configured. This flexible arrangement enables the reconstruction of the lateral pressure fluctuation profile across the filter surface.

Figures 3.8a & 3.8b show that both the upper and lower Pressure Sensor Arrays (PSAs) contain four sensors arranged in a line parallel to the flow direction. This configuration allows for the assessment of pressure fluctuations in the spatial domain along the main flow axis. The upper pressure sensor array was embedded into the rock layer, the sensors were mounted on T-shaped steel rods. As is visible in the right side of Figure 3.9 the cable tubes of the sensors went through the filter layer. These might have caused larger voids at the location of the pressure sensor array.

Figure 3.9: Upper pressure sensor array - Top view - marked - with rock layer (left) and after testing (right)

The board positioned between the upper and lower Pressure Sensor Arrays (PSAs) contains milled grooves that provide channels for routing the sensor tubes. As shown in Figure 3.9, these grooves were subsequently covered and smoothed with aluminium tape to ensure a uniform surface and to prevent local flow disturbances within the filter layer.

3.3.5. Correction for the Measurement - Direct Method

When the hydraulic gradient is obtained from two pressure sensors separated by a finite distance Δx, the resulting estimate represents a *measurement difference* rather than the true spatial derivative. As a consequence, the measured gradient systematically underestimates the true gradient at higher wavenumbers.

To illustrate this effect, consider a pressure wave as depicted in Equation 2.32. The true hydraulic gradient follows from differentiation as shown in Equation 2.37.

The measurement-difference estimate from two sensors spaced Δx apart is

$$i_{\mathrm{MD}}(x) = \frac{p(x+\Delta x) - p(x)}{\rho g\, \Delta x} = \frac{\sin\big(k(x+\Delta x)\big) - \sin(kx)}{\rho g\, \Delta x}.$$

Taking the ratio of the measurement–difference estimate to the true gradient and averaging this ratio over one wavelength yields the transfer function relating their standard deviations. This transfer behaviour, which was derived explicitly in prior internal analyses, is

$$\frac{\sigma(i_{\mathrm{MD}})}{\sigma(i_{\mathrm{true}})} = \sqrt{\frac{2\big(1-\cos(k\Delta x)\big)}{(k\Delta x)^2}}. \tag{3.8}$$

The term in Equation 3.8 quantifies how the sensor spacing attenuates the measured gradient. The attenuation increases strongly with wavenumber, because short-wavelength pressure variations become partially “filtered out” by the finite sensor spacing. This behaviour is shown in Figure 3.10, with the characteristic roll-off and oscillatory pattern at high k.

Since the measured spectrum $\Phi_{i_x i_x}^{k,\mathrm{MD}}(k)$ inherits this attenuation, the true continuous gradient spectrum can be recovered by dividing out the squared transfer function:

$$\boxed{\Phi_{i_x i_x}^{(\mathrm{Direct})}(k) = \frac{\Phi_{i_x i_x}^{k,\mathrm{MD}}(k)}{\dfrac{2\big(1-\cos(k\Delta x)\big)}{(k\Delta x)^2}}} \qquad [\mathrm{m/rad}]. \tag{3.9}$$

This correction compensates for the attenuation inherent to the two-sensor measurement configuration. As expected, the correction becomes ill-conditioned at wavenumbers where the denominator approaches zero (the nulls of the transfer function), and spectral values in those regions should therefore be interpreted with care.

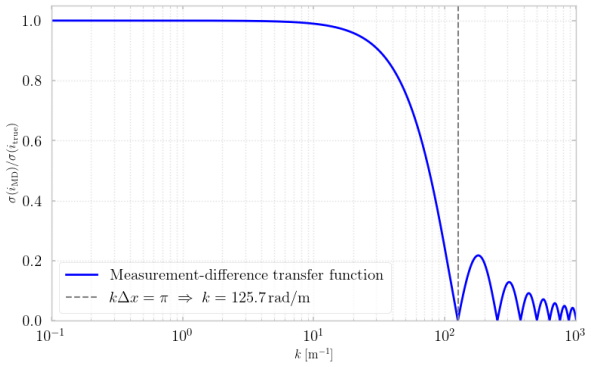

Figure 3.10: Measurement correction factor Direct Method - Standard Deviation

The corrected spectrum Equation 3.9 allows the directly measured gradient spectra to be meaningfully compared with theoretical or indirectly derived gradient spectra in the wavenumber domain.

3.3.6. Pressures sensor preparation

The most critical specifications of the pressure sensor are its pressure range and measurement frequency. The pressure range should be selected based on an estimate of the expected pressure fluctuations in the system to ensure accurate and reliable measurements. Additionally, the measurement frequency must be sufficiently high to capture the turbulence characteristics and to prevent aliasing in the recorded signal.

To ensure the equipment is ready for use, all sensors must first be properly calibrated. Prior to calibration, the sensors should be made water-resistant. Once the wiring is complete, this can be achieved by sealing any exposed components or voids using epoxy resin. When assembling the test setup, the pressure sensors will be positioned sufficiently downstream from the flume inlet to ensure that the flow has fully developed and reached a uniform and stable condition.

3.3.7. Sensor Type

The pressure measurements in this study were obtained using Honeywell 24PCAFA6D differential pressure sensors, installed in both the upper and lower pressure sensor arrays. These sensors measure the pressure difference between two ports and are equipped with a fluorosilicone seal, making them suitable for operation in wet environments. The devices feature a straight-port inlet geometry, allowing direct connection to reference tubing, and a single in-line package (SIP) termination, which facilitates robust electrical wiring during data acquisition.

Table 3.4: Decoding of the Honeywell Pressure Sensor Part Number `24PCAFA6D`

Code	Meaning	Description
`24PC`	Product Series	24PC Series miniature low-pressure sensors (uncompensated, unamplified)
`A`	Pressure Range	± 1 psi differential range
`F`	Seal Material	Fluorosilicone seal
`A`	Pressure Port	Straight-port configuration
	Termination	1×4 SIP, 15.2 mm lead length
`6D`	Output Polarity	Normal polarity output
	Pressure Type	**Differential** pressure

The upper sensor array employed sealed sensors. For these sensors, the top inlet remained open to register the local pore pressure, while the bottom inlet was removed and sealed to minimise geometric footprint such that the sensor would fit inside the dodecahedron housings described in subsection 3.3.1. This configuration ensured that only the external pressure field influenced the measurement.

In contrast, the lower array utilised both inlets of the sensor. The sensors were mounted within a dedicated casing to integrate them flush with the false floor. The lower inlet was connected to a 6 m reference tube routed beneath the false floor and along the flume wall, surfacing in open air approximately 2 m downstream of the array. This configuration ensured a stable atmospheric reference pressure for differential measurements at the filter-base interface. Table 3.4 summarises the decoding of the manufacturer's part number, while Figure 3.11 provides the corresponding mechanical drawing and dimensional specifications.

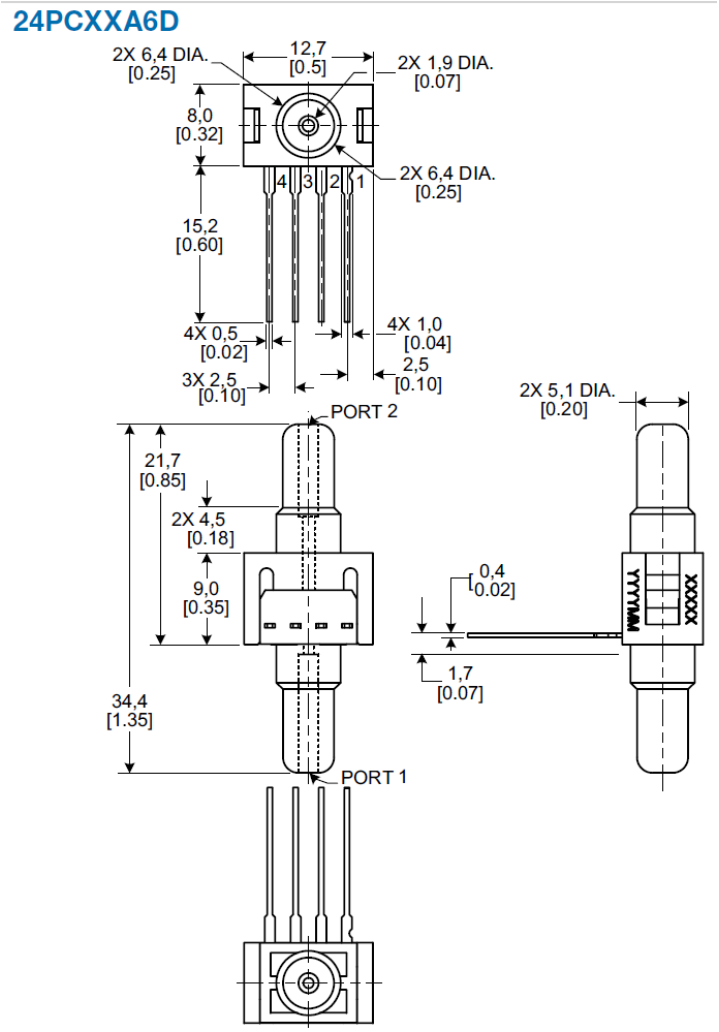

Figure 3.11: Technical drawing of the Honeywell 24PCXXA6D pressure sensor (Honeywell International Inc., 2015).

3.4. Measurements

This section describes the sensors that have been used to measure the variables during the experiments in the flume, discharge, velocity and water level.

3.4.1. Discharge meter

The discharge meter is an ultrasonic flow meter, that measures the discharge of a pipe using sound waves. The discharge meter is essential to accurately know the average flow velocity in the flume. Using the Chezy coefficient and the average flow velocity, the shear velocity can be obtained.

3.4.2. Velocity meter (EMS)

The velocity in single points is measured using two electromagnetic liquid velocity meters (EMS). The velocity measurements are used to indicate the mean flow velocity before the rock layer and the shear velocity at the pressure sensor array. According to Griffin, 2006, “When depths are less than 2.5 ft (76 cm), a single velocity measurement is taken at 0.6 of the total depth.” During the experiments, the maximum water depth was 0.77 m; therefore, the velocity meter was positioned at approximately 40 % of the water depth (measured from the bed), which provides the most representative estimate of the mean flow velocity under turbulent flow conditions. The shear velocity is measured by placing the EMS, very close to the bed as the EMS measures the velocity of the liquid beneath the probe. The EMS is placed in the middle of the flume (in width of the flume), to minimize the wall influence of the sides.

The operation and calibration principles of the electromagnetic velocity meter (EMS) used in the experiments were interpreted based on the Programmable Electromagnetic Liquid Velocity Meter manual provided by Deltares *Programmable Electromagnetic Liquid Velocity Meter, Version 1.1*, 2019. Although it is not confirmed that the EMS applied in these tests is of the exact same model as the one described in the manual, the instrument used appears visually identical and the provided documentation was therefore used as a technical reference to understand its measurement principle, voltage response, and calibration procedure.

3.4.3. Water level meter (WHM)

The water level is mostly measured using Wave height meters, which can be used to calibrate the pressure sensors. The wave height meters uses a probe to measure the height of the water, by registering the conductivity height between two electrodes submerged in the water. One of the wave probes is located one meter before the rock layer and the elevation of the false floor. The second is located approximately 35 centimetres behind the pressure sensor array, this way there is no interference due to the wake of the sensor. Both wave height meters are placed left of the EMS (in width of the flume), the water level is less influenced by the wall on the sides than the velocity. The functioning of the wave height meters was studied using the Wave Height Meter manual published by Deltares *Wave Height Meter, Version 1.1*, 2019.

Apart from the data obtained using the wave probes, the water level has most often been measured using a tape measure. When filling the flume a tape measure is quite accurate, by measuring at multiple locations to verify the height.

3.4.4. Layer thickness

To achieve the desired layer thickness within the flume, a predetermined volume of rock material was distributed among several big bags. Knowing that one big bag represented one cubic metre of material and that the placement area was known, the required volume to obtain the target layer thickness could be accurately estimated. The first layer was installed with a nominal thickness of 4 cm, corresponding to approximately 0.5 m³ of material. Subsequently, an additional 0.25 m³ was placed to increase the total thickness to 6 cm, and this process was repeated one week later to reach the final layer thickness of 8 cm. The installation process was iterative: after each placement, the actual layer thickness was measured, and additional material was added whenever the achieved thickness deviated from the target value. To ensure that the filter is not installed in a tilted way, the flume is filled with water until the top of the rock layer to ensure an even distribution of the material.

Figure 3.12: Layer thickness measurement, top view and side view of measurement

The layer thickness was determined following the methodology described in Maak- en meetnauwkeurigheden bij de uitvoering van baggerwerken en steenbestortingen Hauer, 2000, which emphasizes that the crest of the stones does not accurately represent the position of the reference plane. Therefore, a constant offset of 1 cm below the stone crests was adopted to define the level of the reference plane. As shown in Figure 3.12, the measurement of the layer thickness was conducted using a flat board to determine the crest level, while the top of the reference plane coincides with the elevation of the upper pressure sensor array.

3.5. Test Procedure

The following procedure outlines the step-by-step execution of a single experimental run on a testing day. This procedure ensures consistent data collection across all combinations of filter thicknesses, water depths, and flow velocities.

The test activities consist of systematic adjustments to the experimental setup, enabling controlled variation of key parameters. These adjustments were carried out according to a structured schedule to isolate the effects of different variables. The activities associated with each variable are outlined below. The last activity is the clean up of the entire test setup, this has to be taken into account when making the planning.

Filter Thickness was adjusted on a weekly basis. The procedure involved installing the filter material, adjusting the layer to the desired thickness, and subsequently placing the pressure sensor array directly above the filter layer.

Water Depth was adjusted twice daily, once in the morning and once in the afternoon. This required modifying the Rehbock weir and verifying the water level using float gauges to ensure consistent depth across the test section.

Flow Velocity was adjusted on an hourly basis. This involved increasing the discharge from the pump, checking the flow velocity using a flow meter, and, if necessary, making additional adjustments to the Rehbock weir. The float level gauges and flow velocity meter were monitored during each iteration to fine-tune the weir position and pump discharge.

The chronological order of interventions follows a hierarchy from large to small adjustments: filter thickness represents the most significant intervention and is adjusted once per week; water depth is a medium-scale adjustment and is modified every half day; and flow velocity is the most frequently adjusted parameter, changed each hour.

This testing procedure results in a total of 160 unique configurations of the test setup. Each configuration is tested for a duration of 10 minutes, leaving an additional 50 minutes per hour to carry out the necessary setup changes and allow the system to stabilize before the next measurement begins. Every first morning of the week there is 4 hours to install the next filter layer thickness, considering that this is a more labour intense action.

3.5.1. Preparation

The test preperation is quite similar for a Wave or current test sequence, therefore both will be described in this section. The main differences are the placement of equipment and the use of equipment.

The preparation of a test run is structured in the following way:

- **Safety inspection:** Prior to beginning the test, the laboratory environment must be verified to be safe. Ensure that no personnel are working alone in the Waterlab, and that the flume is free from tools, debris, or other obstructions that could interfere with the flow or pose safety hazards.
- **Installation of the flow conditioner (current):** Position the flow-conditioning element upstream of the test section to promote a uniform velocity distribution and minimize turbulence intensity at the measurement location. Remove the breakwater at the end of the flume for current sequences.
- **Installation of the breakwater (waves):** Position the breakwater at the downstream end of the flume and adjust its crest elevation to slightly above the still-water level. This configuration allows partial wave energy dissipation while minimizing full-wave reflection from the back wall. If the breakwater is positioned too high, excessive reflection may occur, counteracting its intended damping function. The flow conditioner used in current test sequences should be removed prior to wave testing.
- **Adjustment of the Rehbock weir:** Set the Rehbock weir to the target elevation corresponding to the desired steady-state water depth for the test configuration.
- **Positioning of velocity and wave sensors:** Adjust the height of the Electromagnetic liquid velocity meter (EMS) and Wave Height Meters (WHM) in accordance with their designated configurations. The EMS should be placed at the depth defined in subsection 3.4.2, while the

WHM probes should be submerged to approximately half their active length to ensure accurate readings. In the case of a wave test sequence, the wave height sensors should be positioned such that the probe tips remain continuously in contact with the water surface, while ensuring that the sensor housings do not come into direct contact with the water. Velocity meter and discharge meters can be turned off in case of wave testing.

- **Filling of the flume:** Activate the pumps to gradually fill the flume. Water is supplied through two inlets located at the upstream and downstream ends of the flume. As the water level approaches the target depth, the upstream inlet should be closed to allow controlled filling via the downstream inlet. This ensures a gradual increase in water level and prevents overshooting the desired water depth. Once the target level is reached, switch off the pumps and allow the flow to stabilize before proceeding.
- **Data acquisition setup:** Verify the DASYLab-file to ensure all acquisition channels are correctly defined. Start the recording software in preparation for data collection.
- **Sensor functionality verification:** Power on all measurement devices and confirm their responsiveness to the increasing water level. Sensors should exhibit a measurable change in output, indicating proper functionality.
- **Sensor calibration:** After the flume has been filled, recalibrate all sensors to ensure their output signals remain within the voltage range limits (typically ± 10 V). This prevents signal saturation and guarantees accurate measurement throughout the test.

3.5.2. Execution

During the execution of the experiments all adjustments are stored in a logging file, not just the DASYLab file but a file that registers all the manual changes. The data is stated below:

- Date and time of testing and manual changes
- Height of EMS
- Height of WHM
- Exact water depth
- Frequency of the pump
- Obstacle placement (distance and when placed)
- wave sequence (Wave height, Peak period and regularity)

The filling of the flume could cause a very long standing wave in the flume, this wave takes a while to be dampened and allowed the water depth to not be able to register immediately.

The current sequences consisted of ± 4 sequences with gradually higher discharge and 4 obstacle sequences with 2 discharge settings per obstacle alteration. So one with a medium discharge intensity and one with a high discharge intensity. The obstacle alterations meant the distance to the PSA, which was either one meter or two meters.

Adjustment of the pump intensity was performed iteratively. During the first week of testing, the upper and lower operational limits of the pump settings were determined through a series of trial-and-error experiments. Each test sequence was conducted under specific pump configurations, and the corresponding adjustment times were systematically logged. After each change in pump frequency, both the pump system and the flume required a stabilization period to reach steady-state flow conditions. Consequently, the logged adjustment times do not directly coincide with the start times of the measurement segments, as the stabilization periods were later accounted for during data processing.

3.5.3. Post-Processing

After each test period the Data acquisition is stopped, and a new file is created. The begin and the end of a test period was distinguishable by a change in water depth, this was the time a new and different file was created.

3.6. Test Program

This section dives into the planning of the tests, especially the program of the preparation and the execution of the experiments. The following step-by-step plan outlines the preparation and execution of the physical experiments.

3.6.1. Key parameters

This section addresses the key parameters that will be registered to check the influence on the pressure fluctuations.

- **Pressure fluctuation:** This is the primary variable of interest, representing the temporal variations in pressure measured by the upper and lower Pressure Sensor Arrays (PSAs). These fluctuations reflect the dynamic interaction between the overlying flow and the porous filter layer and form the basis for the spectral and damping analyses.
- **Water depth:** The mean water level in the flume, measured continuously using the Water Height Meters (WHM). Water depth affects both the hydrostatic pressure component and the development of flow structures, thereby influencing the magnitude and frequency distribution of the pressure fluctuations.
- **Mean velocity:** The time- and space-averaged flow velocity in the test section, determined from the Electromagnetic Flow Meters (EMS) and discharge measurements. The bulk velocity governs the turbulence intensity and energy input to the system and is therefore a key parameter in the scaling of the pressure spectra.
- **Filter thickness:** The thickness of the rock layer placed above the impermeable base, defined as the vertical distance between the top of the base plate and the filter surface. Filter thickness controls the degree of pressure damping and the permeability characteristics of the layer and is varied between test series to examine its influence on the damping of pressure fluctuations.

3.6.2. Boundary conditions

For the setup of the tests, the dimensions of the test setup are very important. Prevention of delays depends on the delivery of the needed equipment and samples. To determine the dimensions of the set up, some of the input parameters have to be set and known beforehand. The hydraulic boundary conditions, which partly depend on the flume capacity (subsection 3.1.1), consist of the flow velocity $[\overline{u}]$, depth $[h]$, kinematic viscosity $[\nu]$, and Shields parameter $[\psi]$. The porosity n of the filter layer and the base layer grain size d_{50b} have to be assumed, the experiment will not involve a geotextile or base sediment; therefore a simple assumption of normal sand can be used. Other input parameters are the spectral description (Thomas, 2023), and the critical gradient (Akerboom, 2024).

The dimensions of the test set up are essentially dependent on six fundamental factors. These can be combined into a design space, where all of these requirements are met. The conditions are the following:

1. The discharge cannot exceed the pump capacity, this gives an upper limit on the flow velocity $[u]$ and water depth $[h]$.
2. The width and height of the experiments are limited to the dimensions of the flume, lower values are achievable, but greater values are not. The width can be decreased, but is not preferable.
3. The filter has to be stable, which means it cannot exceed value of 0.03 for the shields parameter, this gives a lower limit on the grain size $[d_{50}]$.
4. The flow within the flume should not surpass criticality or be near criticality, therefore the Froude number $[Fr]$, can not be higher than 0.75. This constraint will give upper boundaries for the flow velocity $[\overline{u}]$ and water depth $[h]$.
5. Within the porous material there should be turbulent flow, this means that the Reynolds number for porous media should be higher than 300 as stated by Jensen et al., 2014.This constraint will give lower boundaries for the grain size $[d_{50}]$ and flow velocity $[\overline{u}]$
6. The value of the critical gradient, obtained by Akerboom, 2024 cannot be exceeded. However, the execution of the experiments need s to occur near the critical value.

7. The experiments should lead to a measurable fluctuating gradient, the correct range is derived from Thomas, 2023.
8. The filter has to be available and practical. The chosen grading and grain sizes should be commercially available to ensure that the material can be sourced without difficulty. At the same time, the filter material should be practical to work with: grains that are too small can make placement time-consuming and labor-intensive, while grains that are too large may be difficult to handle or compact properly in the setup. Furthermore grading that is too wide will pose difficulties obtaining the desired porosity.

The construction of the design space and the determination of the setup dimensions are covered in Appendix D.

Variables overview

This subsection gives an overview of the ranges of the independent variables that will be used during the tests. These have been derived from the boundary conditions given in Table 3.1 and further calculated in Appendix D.

Table 3.5: Testing Ranges of Independent Variables

Variable	Symbol	Range	Unit
Water depth	h	0.30 - 0.63	[m]
nominal diameter	d_{n50}	0.015	[m]
Flume flow velocity	$\overline{u}$	0.1 - 0.9	[m/s]
Filter flow velocity	u_f	0.005 - 0.06	[m/s]
Filter thickness	D_f	0.04 - 0.08	[m]

Figure 3.13 shows the test conditions that have been conducted and feasible region with the boundary conditions that caused physical limits had to be taken into account.

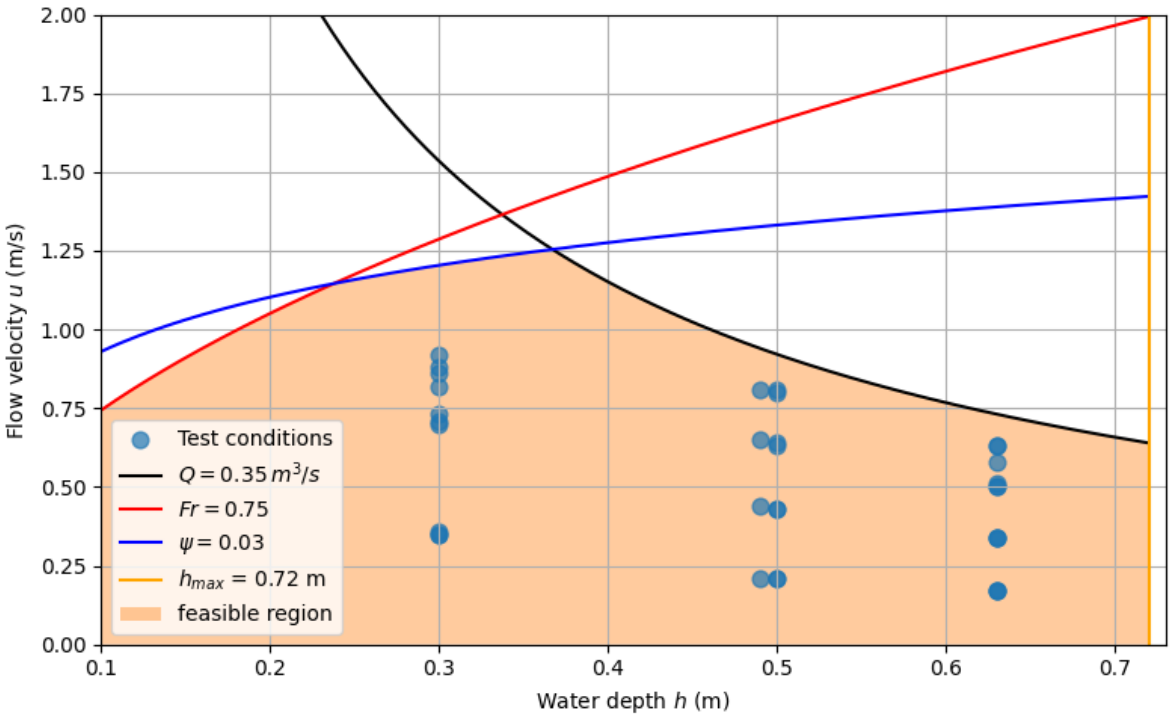

Figure 3.13: Current Test conditions with Boundary conditions

3.6.3. Preparation Phase

The preparation phase comprises all activities required before the start of the physical testing campaign. This includes the preparation of materials, calibration of the measurement equipment, and the setup of the flume facility, in accordance with the requirements specified in sections 3.1, 3.2, 3.3 & 3.4.

This phase spanned the period from the thesis kick-off on 23 April until the commencement of the tests on 21 July. The main preparatory activities are summarised below:

- Design of the experimental setup
- Procurement of materials and components:
  - Filter material (basalt split)
  - Pressure sensors
  - Tubing and connectors
  - Betonplex boards for the false floor
- Cleaning and sieving of the basalt split
- Creation of the desired filter grading and porosity
- Installation of the false floor
- Calibration of pressure sensors
- Calibration of pumps
- Verification of false-floor performance and reference measurements

Most of the activities listed above are straightforward; however, the calibration procedures for the pumps and pressure sensors require further explanation. The pumps were calibrated prior to testing by systematically adjusting their rotational frequency (rpm) and recording the resulting discharge and mean flow velocity using the Electromagnetic Flow Meters (EMS) and Water Height Meters (WHM). This procedure established a direct relationship between the pump frequency and the generated discharge, ensuring reliable flow control during the experiments.

The calibration of the pressure sensors followed the same principle as the tests described in section G.4, where each sensor was immersed in a water basin to determine the voltage–pressure relationship across its full operating range. This direct, analogue calibration method was preferred, as it provides a clear voltage-to-pressure conversion prior to data acquisition and processing.

An alternative calibration procedure was also considered, in which the sensors would be calibrated in situ by filling the flume to the sensor limit (or the maximum water level) and subsequently draining it while recording the corresponding water depth as a function of measured voltage. Since the data acquisition system stores values with precise time stamps, the depth could then be related to both absolute and elapsed time. However, this approach was not applied during the present tests, as the analogue basin calibration already yielded a reliable and reproducible voltage–pressure curve for each sensor.

After the first calibration of the sensors, the second method could be used repeatedly afterwards, by acquiring the data while the flume was being drained at the end of a test series.

1. **Selecting and Purchasing Equipment and Materials**
    - Select pressure sensors with an appropriate measurement range and frequency response, according to section 3.1.
    - Select grain size, according to subsection 3.2.2.
    - select grading, according to subsection 3.2.3.
    - Select the right range of filter thicknesses and purchase the right volume of rock using the method for determining filter thickness in subsection 3.2.4 and combine it with the dimensions of the Flume as stated in subsection 3.1.1.
2. **Prepare Filter Material and equipment**
    - Calibrate sensors under controlled conditions.
    - Seal and waterproof sensors and wiring using epoxy.
    - Wash and clean stones to remove fine particles and contaminations.
3. **Instrumentation Setup**
    - Install sensors at the top and bottom interfaces of the filter layer in the flume.
    - Verify sensor functionality and signal quality with a dry test.

3.6.4. Execution phase

The execution phase is mainly focussed on the execution of the tests, performed in the Sediment Flume from the 22^{nd} of July until the 15^{th} of August. The planning of this phase depends on the reconstruction and readjustments that will be done to obtain different conditions and combinations of the independent variables. The test procedure is structured in three levels. Firstly, the thickness of the stone layer is varied on a weekly basis. Considering that the whole test period is over a duration of four weeks, gives the opportunity to conduct control tests and tests on three layer thicknesses. Subsequently, the water level is adjusted a maximum of twice a day. For each water level setting, the flow velocity is systematically varied several times to capture the full hydraulic response.

The experimental testing program will be carried out over a four-week period. The final week is reserved for additional testing or repeating incomplete trials.

1. **Week 1: Initial Tests and Calibration**
    - Verify flume operation and stabilize baseline flow conditions.
    - Install and calibrate pressure sensors.
    - Conduct preliminary runs to test data logging, sensor sensitivity, and signal quality.
    - Check wave conditions and ensure no wave breaking.
2. **Week 2, 3 & 4: Install filter layer $D_f = 4,\ 6,\ 8$ cm**
    - Install the correct layer thickness for the test.
    - Conduct current tests.
    - Conduct Wave tests.
    - Clean the Flume and prepare for next layer.

3.6.5. Program overview

This section shows the types and quantity of tests that have been conducted during the execution phase of the experiments.

Test Planning

These tests only include the Current tests without obstacle.

Table 3.6: Planning summary per week (layer thickness, water depth, mean velocity).

Layer [cm]	Water depth [m]	Mean U [m/s]
0	0.50	0.20–0.90
	0.75	0.20–0.90
4	0.30	0.35, 0.70, 0.86, 0.92
	0.49	0.21, 0.44, 0.65, 0.81
	0.63	0.17, 0.34, 0.51, 0.63
6	0.30	0.36, 0.73, 0.82
	0.50	0.21, 0.43, 0.63, 0.80
	0.63	0.17, 0.34, 0.50, 0.63
8	0.30	0.35, 0.71, 0.88
	0.50	0.21, 0.43, 0.64, 0.81
	0.63	0.17, 0.34, 0.50, 0.58

Wave sequences

The wave conditions tested during these experiments have been determined using the literature and theoretical background explained in Appendix E. The water depth during the wave test was, during all tests, 0.5 meters above the sensor array.

Table 3.7: Wave program summary per week (peak period T_p, significant height H_s, and regularity).

Layer 0 cm			**Layer 4 cm**		
T_p **[s]**	H_s **[m]**	**Kind**	T_p **[s]**	H_s **[m]**	**Kind**
1.5	0.10	Regular	1.5	0.18	Irregular
1.5	0.10	Irregular	3.0	0.20	Irregular
1.2	0.10	Irregular	1.2	0.10	Irregular
1.5	0.15	Irregular	1.5	0.05	Irregular
1.5	0.18	Irregular	1.5	0.10	Irregular
3.0	0.21	Irregular	1.5	0.10	Regular
2.0	0.15	Regular	1.0	0.15	Regular
Layer 6 cm			**Layer 8 cm**		
T_p **[s]**	H_s **[m]**	**Kind**	T_p **[s]**	H_s **[m]**	**Kind**
1.5	0.18	Irregular	1.5	0.18	Irregular
3.0	0.20	Irregular	3.0	0.20	Irregular
1.2	0.10	Irregular	1.5	0.05	Irregular
1.5	0.05	Irregular	1.2	0.10	Irregular
1.5	0.10	Irregular	1.5	0.10	Irregular
1.5	0.10	Regular	1.5	0.10	Regular
1.0	0.15	Regular	1.0	0.15	Regular

4

Data processing

In this chapter the data management, and in more detail the data processing is touched upon. This chapter begins with the data management during the tests, followed by the handling of the data by loading and converting, next the filtering of the raw data is explained and finally the data checks, that verify the integrity of the steps, are elaborated

4.1. Managing Data

As shown in subsection 3.6.5, the test have been divided into weeks and the weeks have been divided further into water depths with the distinction between current and wave tests. Each experimental period consisted of three data files, one file contained the data from 12 sealed pressure sensors, a second file consisted of data from 12 pressure sensors with a reference tube, the last file contained the reference sensor data. The reference sensors were the discharge sensor, the two height sensors and two velocity sensors. The settings and time periods of the pump were noted in an excel file together with the wave generator data.

4.2. Data Handling

This section describes how the experimental data were imported, processed, and converted into physically meaningful quantities. It explains the workflow from loading the raw `.asc` exports produced by the DASYLab acquisition system, through selecting and synchronising the relevant time windows, to applying the appropriate calibration and unit conversions. The resulting datasets form the basis for all subsequent analyses.

4.2.1. Loading Data

The loader module is designed to process the DASYLab `.asc` export files and convert them into time-aligned datasets suitable for analysis. It reads the raw text files, extracts essential timing information, isolates specific time windows, normalises the data, and merges multiple recordings into a single continuous time series.

Extracting Header Information

The first step scans the header of each `.asc` file to retrieve key metadata that define the timing of the recording. Specifically, it identifies:

- the recording start time from the “Recording date” entry,
- the sampling interval from the “Delta” line, and
- the position of the first data row based on the “Measurement time” marker.

Once these items are found, the scan stops. If certain information is missing, default values are used, or an error is raised when critical timing data are unavailable. The result of this step is a clear definition of the start time, the sampling frequency, and the data’s header position.

Reading and Windowing the Data

The second step loads only the portion of data corresponding to a specified time window on the day of the recording. It converts the given clock times (e.g. “09:00–09:30”) into absolute timestamps using the previously determined start time, ensuring that the requested interval lies within the available data. Based on this window, it calculates how many samples to skip and how many to read, reducing the memory needed to operate the data.

The data are then imported efficiently with `pandas`, selecting only the relevant columns. Column names are standardised, European decimal commas are replaced by dots, and all numeric values are cast to a consistent float format. The relative time column is converted into a true time offset and added to the recording start to create an absolute `DateTime` index. The result is a clean, time-indexed dataset containing only the selected variables within the desired time frame.

Combining Multiple Runs

The final step allows multiple recordings or time windows to be merged into a single continuous dataset. Each file is processed as described above, after which the resulting time-indexed tables are concatenated and sorted chronologically. Any duplicate timestamps caused by overlapping windows are removed. This produces one coherent, gap-free time series ready for further processing or visualisation.

Loader Summary

In summary, the loader module automates the conversion of raw `.asc` exports into structured, time-aligned `DataFrame` objects. It ensures that all selected signals are correctly scaled, windowed to the periods of interest, and seamlessly joined across multiple test runs, forming the foundation for subsequent analysis and plotting routines.

4.2.2. Converting Data

This subsection explains how the raw signals obtained through the ASC-Loader (subsection 4.2.1) were converted into physically meaningful quantities. The voltage outputs from the upper (B) and lower (A) pressure sensor arrays (1B–12B/1A–12A) were calibrated during the test and in the test week without filter layer. The calibration was done by draining the flume, the wave height meter is calibrated by noting the Voltage per centimetre water level drop. Next the pressure sensors were compared to the calibrated wave height meter data, now there is a 1.81% difference between the upper and lower pressure sensors, the conversion data of both sensors is visible in Table 4.1.

The reference data include signals from the discharge meter, EMS velocity sensors, and height meters located both at the array and upstream of the rock layer. These voltage signals were converted into discharge, velocity, and head values in SI units (m³/s, m/s, and Pa). The EMS conversion was performed using the Deltares calibration certificate van Nieuwenhuizen and Taal, 2021, while the discharge and height meters were calibrated during week 2.

The discharge meter output ranged from 2–10 V, with 2 V representing zero flow. Voltages were corrected by subtracting 2 V and scaled to obtain the discharge in liters per second, subsequently converted to cubic meters per second. Average flow velocities were then derived by dividing the discharge by the flume width and water depth. The height meters were converted to pascals to allow comparison with the pressure sensors. All applied conversion factors are listed in Table 4.1.

Table 4.1: Sensor conversion factors applied in the data pre-processing

Signal	Input units	Conversion applied	Output units
Lower PSA (1A–12A)	V	$p = V \cdot 408.28965 * 1.0181$	Pa
Upper PSA (1B–12B)	V	$p = V \cdot 408.28965$	Pa
Flow meter Q	V	$Q = (V - 2) \times 50/1000$	m^3/s
Velocity avg. array	V	$\overline{u} = Q/(\text{Width} \cdot \text{Depth}_s)$	m/s
Velocity avg. free	V	$\overline{u} = Q/(\text{Width} \cdot \text{Depth}_{\text{free}})$	m/s
Velocity sensor (EMS)	V	$u = \Delta V \cdot 0.1023 + 0.002 - 0.000188\,(\Delta V)^2$	m/s
Height sensor	V	$p = V \div 40.57 \times 9.81 \times 10^3$	Pa

4.3. Data Filtering

After the experiments, the data is cleaned using multiple filtering techniques, this helps to remove any external influences and to get to the root of the experiment. In this section, the current experiments are mainly considered, for these need more filtering to make a distinction between noise and usable signal. During the wave experiments, the interesting data is more in the lower frequencies and wavenumbers, therefore little filtering is needed, only linear de-trending is performed to align all signals. The first few filtering techniques are basic methods to clean the pressure signal, from the coherence filter onward the filter methods are executed on the power spectral density plots. These methods influence the data in a more complex way and have more impact on the eventual results, therefore it is crucial to understand the assumptions that have been made. To clearly display the influence of each filter method, there is a before and after graph. The examples that have been given of the filtering techniques are made from the test sequence with a water depth of 50 cm, a layer thickness of 8 cm and multiple flow velocities, these are often displayed in the titles of the plots.

4.3.1. Raw Data

This subsection gives an idea of what the data looks like before it has been filtered. The ”Raw” graphs in the subsections are sometimes filtered using methods described before or directly after, this is to make very clear what the filter method does. The raw data displayed in Figure 4.1 shows the pressure signal of the pressure sensors after conversion from Volts to Pascals.

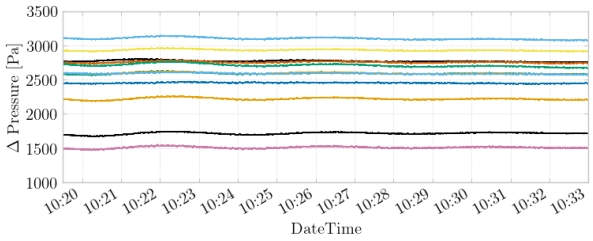

Figure 4.1: Raw signal data example

4.3.2. Fast Fourier Transform

The raw spectrum uses the filtered signal data, before the spectra filtering is performed, the data has undergone Linear de-trending, a Hampel filter and a high-pass filter. The filtered signal data is then put through a fast Fourier transform to show the amplitude versus the frequency, in the case of Figure 4.2, the FFT is converted from frequency in Hertz to angular frequency in radians per second.

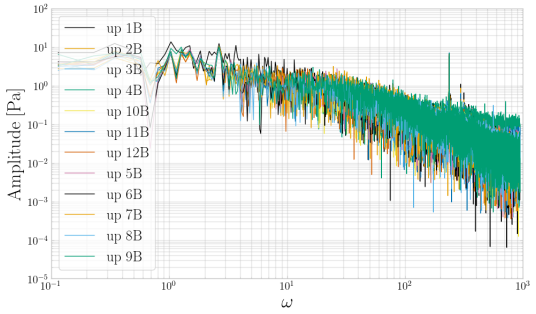

Figure 4.2: Fast Fourier Transform Unfiltered, upper pressure sensor array

4.3.3. Welch Method

To estimate the Power Spectral Density (PSD), the Welch method is applied to each pressure signal using a Hann window and the parameters listed in Table 4.2. The sampling frequency corresponds to that of the pressure sensors. Each segment has a window length equal to half the number of points used in the FFT computation. Consecutive windows overlap by 50% of the window length to reduce variance and obtain a smoother spectral estimate.

Current Data

The welch method works the same for the current data as for the wave data, except for the input of the method, therefore a distinction has been made.

Table 4.2: Sampling and Welch parameters current

f_s	Δt	N	n_{window}	n_{fft}	n_{overlap}
300 Hz	$1/f_s$	13	2^N	$2^{(N+1)}$	$2^{(N-1)}$

The graph in the right graph of Figure 4.3, is the mean of the Power Spectral Densities of the 12 sensors showed on the left of Figure 4.3. The orange line in the right of the graph, shows the hypothesis proposed by Thomas, 2023. The hypothesis underestimates the energy of the frequencies prior to filtering.

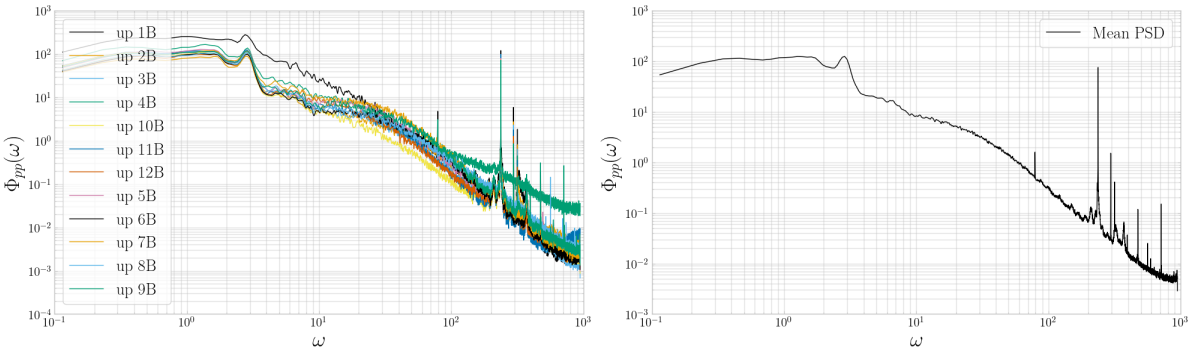

Figure 4.3: Power Spectral Density, upper pressure sensor array

Wave Data

The data acquisition of the sensors goes with a sampling frequency of 300 Hz, this frequency and according time interval result in a too high resolution as visible in Figure 4.4, therefore the wave data has been resampled, the new sampling frequency and other welch input parameters have been shown in Table 4.3. During resampling the data with a higher frequency than 4 Hz has been cut off, using a Butterworth filter.

Table 4.3: Sampling and Welch parameters Waves

f_s	Δt	N	n_{window}	n_{fft}	n_{overlap}
$3\ Hz$	$1/f_s$	8	2^N	$2^{(N+1)}$	$2^{(N-1)}$

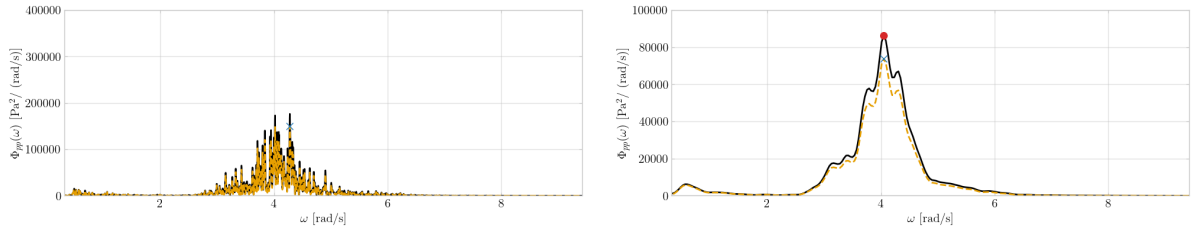

Figure 4.4: Waves pressure Power Spectral Density sampling frequency 300 Hz (left) and resampled (right)

4.3.4. Linear De-trending

The linear detrending of the signal is applied to remove slow temporal drifts, representing the first step of the filtering process. As shown in Figure 4.5, the left panel exhibits a gradual low-frequency trend that is effectively removed in the detrended signal on the right.

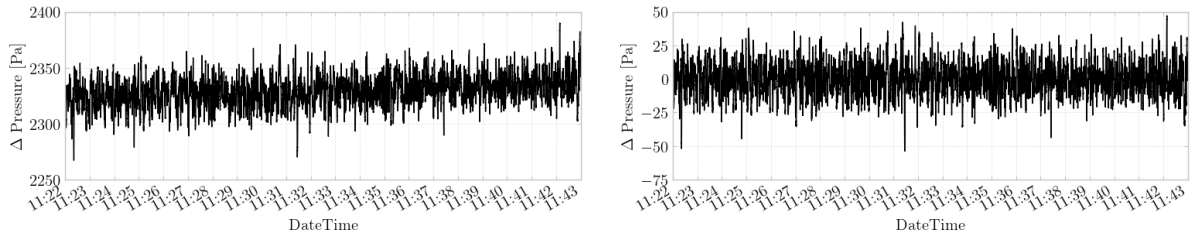

Figure 4.5: Linear de-trended single signal before (left) and after (right)

Since the objective of this research lies in the analysis of pressure fluctuations rather than absolute pressure levels, it is essential to normalise the pressure time series to enable meaningful comparison between sensors. The linear detrending step not only eliminates long-term drifts but also brings the signals to a comparable reference level, as illustrated in Figure 4.6.

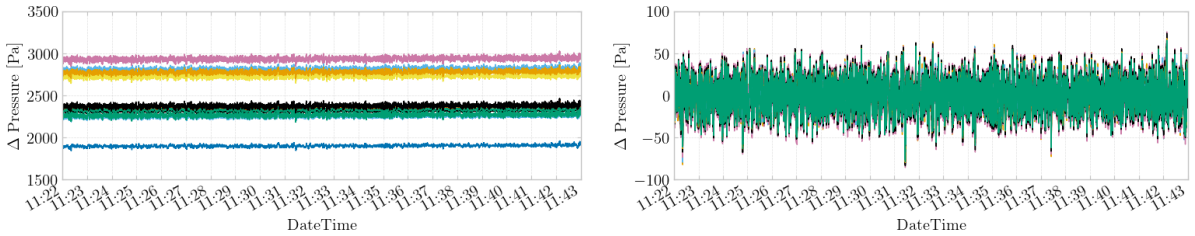

Figure 4.6: Linear de-trended multiple signals before (left) and after (right)

4.3.5. Hampel filter

The Hampel filter, filters the extreme outliers that will give an unrealistic output, this will later reduce the outliers in high frequency domains. The filter corrects in a time series based on the median and the median absolute deviation (MAD) within a local moving window. Unlike mean-based filters, it is resistant to skew from extreme values, making it well suited for impulsive noise. Each sample is evaluated against the local median; if its deviation exceeds a multiple of the MAD, it is flagged as an outlier and replaced (typically by the median). This preserves the underlying signal structure while suppressing spurious spikes, offering a statistically robust alternative to conventional smoothing in noisy experimental data.

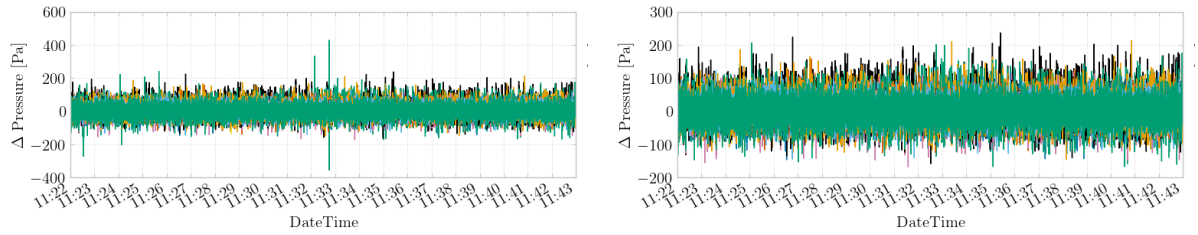

Figure 4.7: Hampel filter signal before (left) and after (right)

4.3.6. high-pass Filter

The high-pass filter uses a previously determined cutoff frequency, that removes very low frequencies (slow trends or drift), while leaving higher-frequency content in tact. In short, it acts as a detrender that suppresses long-term correlation and emphasizes short-term variability, short-term variability in the case of this research is the turbulence domain. The low frequencies have an external root, for example, during testing the first current sequence often had a very long wave signal, this was due to the filling of the flume. This difference is clearly visible in Figure 4.8, where the period is multiple minutes.

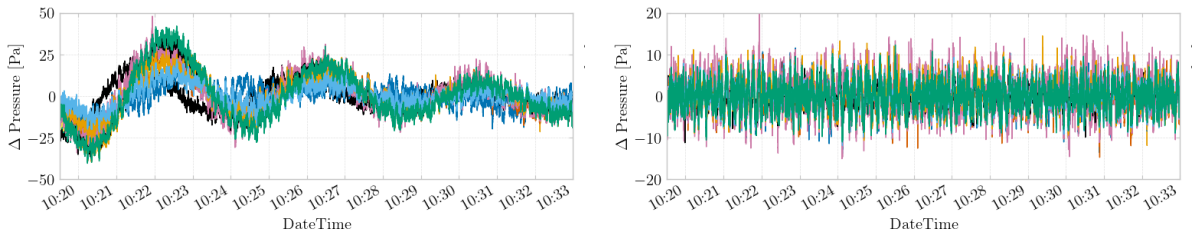

Figure 4.8: High-pass filter signal before (left) and after (right)

In this function, a Butterworth filter is used because it provides a maximally flat frequency response in the passband, meaning it suppresses unwanted drift smoothly without distorting the spectral shape near the cutoff. The filtering is performed using a forward–backward routine, which applies the filter twice (once forward, once backward in time) so that any phase shifts introduced by the filter are exactly canceled. The result is a clean, zero-phase signal where slow baseline variations are eliminated while preserving the true amplitude and timing of the fluctuations.

4.3.7. Notch Filter

The notch filtering, also called band-stop filter, weakens high frequencies that have been made visible using the premultiplied spectrum. In the case of the tests, the pump frequency is a very prominent high frequency, which should be removed for a smoother spectrum. The premultiplied spectrum explained in subsection 4.3.10, can show anomalies that should be filtered, these anomalies first have to be checked. The only frequency that has been notched in these experiments have been the pump frequencies, the peaks in the premultiplied spectrum corresponded to the pump frequencies that have been noted during testing.

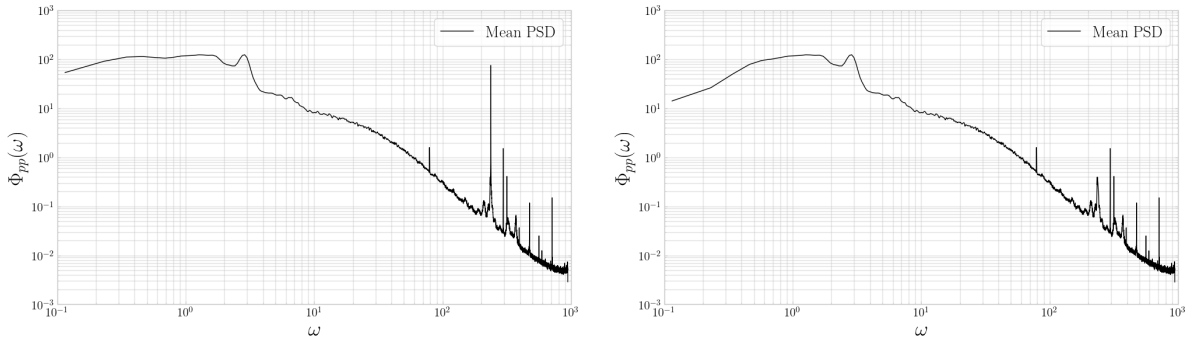

Figure 4.9: Notch filter signal before (left) and after (right)

The notch filter works as follows, when the frequency is detected, a gap is created and the gap is filled using interpolation. The width of the gap is chosen to be 1 Hz, meaning that the range of the gap is 0.5 Hz above and below the notch-frequency.

4.3.8. Coherence filter

The coherence filter is a method derived from Hofland (2005), that compares two sensors that are far apart and finds the frequencies with a high coherence. These frequencies are due to external influences (with high frequencies) or long waves in the flume and do not represent the turbulent frequencies. To better show the turbulent frequency spectra, these frequencies should be removed.

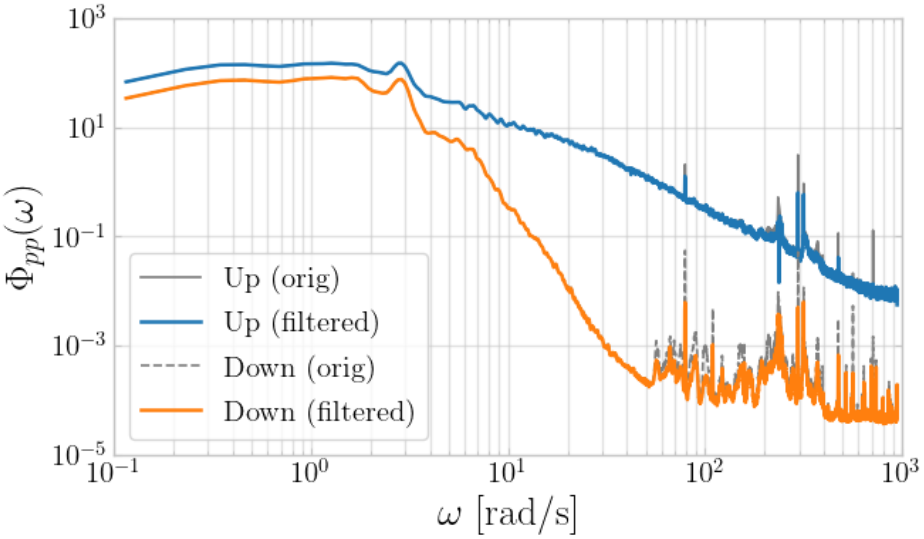

Figure 4.10: Coherence filter on Power Spectral Density, lower pressure sensor array

Figure 4.10 clearly shows the lower frequencies to have a lot of coherence and some higher frequencies to have a lot of coherence as well, the orange line shows the power spectral density after filtering.

4.3.9. White noise filter

White noise filtering was applied as a final post-processing step to further smooth the spectral curves and reduce the influence of high-frequency noise. In the spectral representation, the lower pressure sensors typically exhibit a lower energy boundary due to their position within the filter layer. The white noise filter estimates the mean background noise level by averaging the spectral energy over the frequency range where the combined slope of the PSD approaches zero—that is, where the tangent of the spectral values indicates no further physical signal decay. This mean noise level is subsequently subtracted from the entire power spectral density, under the assumption that white noise contributes uniformly across all frequencies.

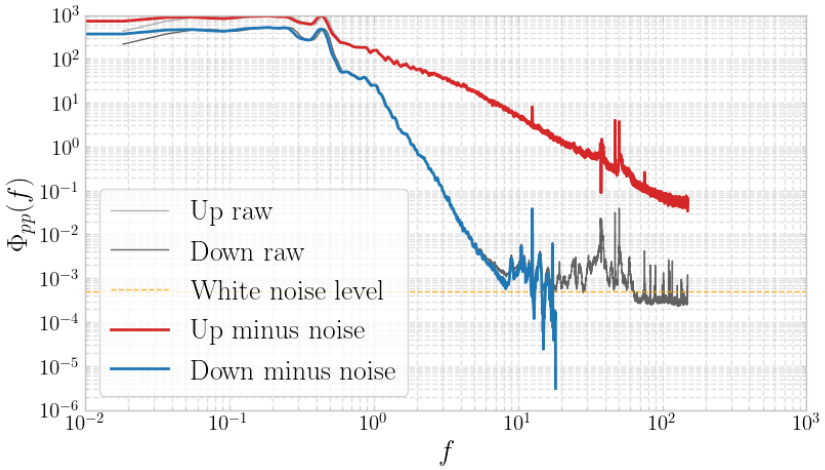

Figure 4.11: White noise filter on Power Spectral Density, lower (blue) and upper (red) pressure sensor array

Following this correction, the spectrum is truncated at the first wavenumber or frequency where the filtered PSD becomes negative. Beyond this point, the values are considered dominated by noise and no longer physically meaningful. Excluding these unreliable high-frequency components prevents the introduction of artificial values and ensures a clearer and more representative visualisation of the physical spectrum.

4.3.10. Premultiplied pressure spectrum

A premultiplied spectrum highlights which wavenumber ranges contribute most to the total energy, recognising that the variance of the signal equals the area under the spectrum. By multiplying the spatial spectrum with the wavenumber, i.e. plotting $k\,\Phi(k)$, the contribution per logarithmic wavenumber interval becomes visible. This emphasises features at higher wavenumbers and facilitates identifying the dominant energy, containing scales in the signal.

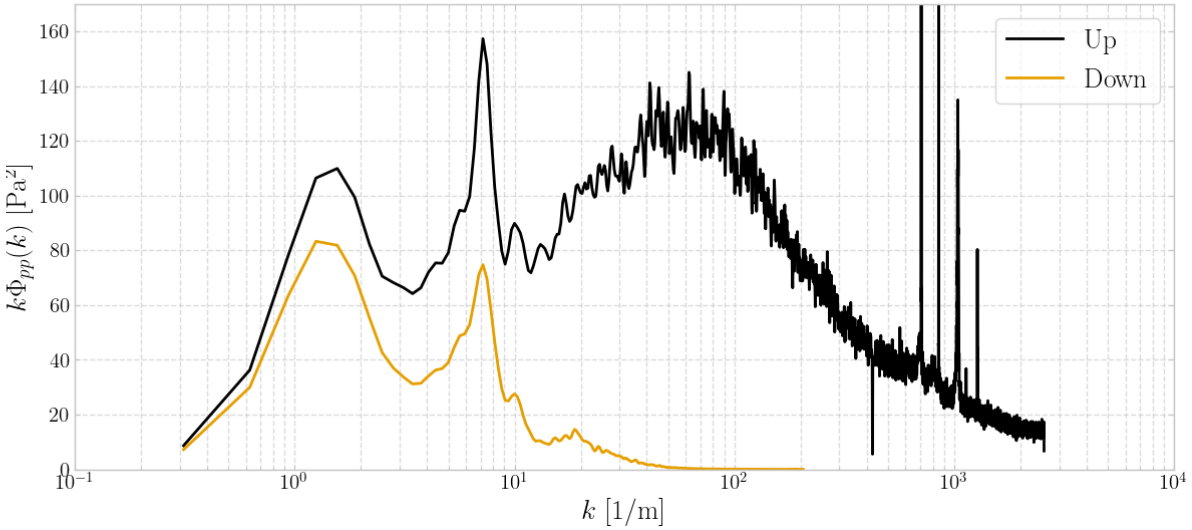

Figure 4.12: Premultiplied pressure spectrum

Premultiplied spectra are particularly useful for distinguishing different physical processes within the signal, such as hydrodynamic waves, turbulent pressure fluctuations, and measurement noise. In Figure 4.12, the upper PSA is shown in black and the lower in orange. Two distinct peaks occur at low wavenumbers, followed by a broad energetic region at intermediate wavenumbers and several sharp peaks at high wavenumbers. The sharp high-wavenumber peaks are likely caused by external interference, such as pump vibrations or structural resonance, and can be removed using the notch filter described in subsection 4.3.7.

The low-wavenumber peaks likely correspond to hydrodynamic wave components caused by filling effects or near-critical flow conditions, whereas the broader mid-wavenumber region represents turbulent pressure fluctuations within the flow.

4.3.11. Difference filter

Difference filter is a separate method of obtaining the hydraulic gradient, the method uses two pressure sensors that are in line with the flow direction and with a determined distance between them. By directly taking the difference between the two pressure sensors, and by knowing the distance in between, the hydraulic gradient can be determined as done in Equation 4.1.

$$i = \frac{\Delta h}{\Delta x} = \frac{\Delta p}{\rho_w g \Delta x} = \frac{p_1 - p_2}{\rho_w g \Delta x} \tag{4.1}$$

The noise caused by the pump frequency has been removed using the notch filter before making the graph in Equation 4.1. Most anomalies are filtered when using the difference filter.

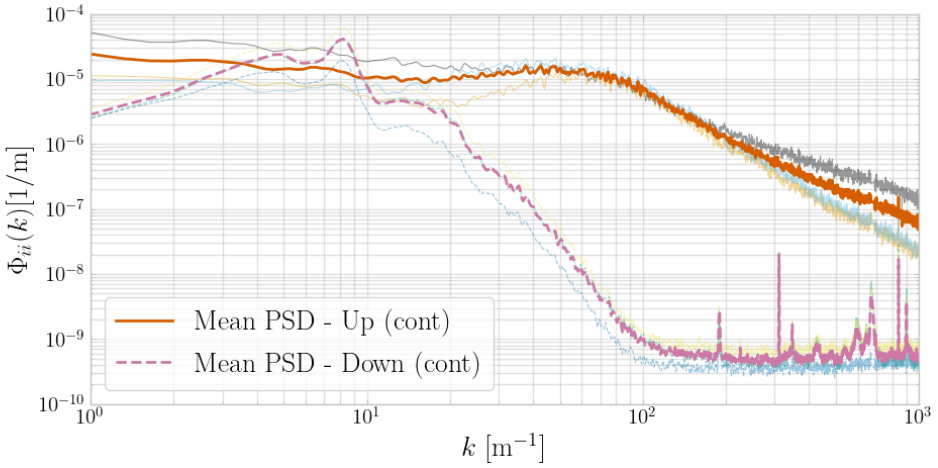

Figure 4.13: Difference filter

4.3.12. Filtered direct gradient PSD

After applying a white noise filter for the direct filter, the final direct gradient Power spectral Density is visible in Figure 4.14, with both the upper and the lower PSA.

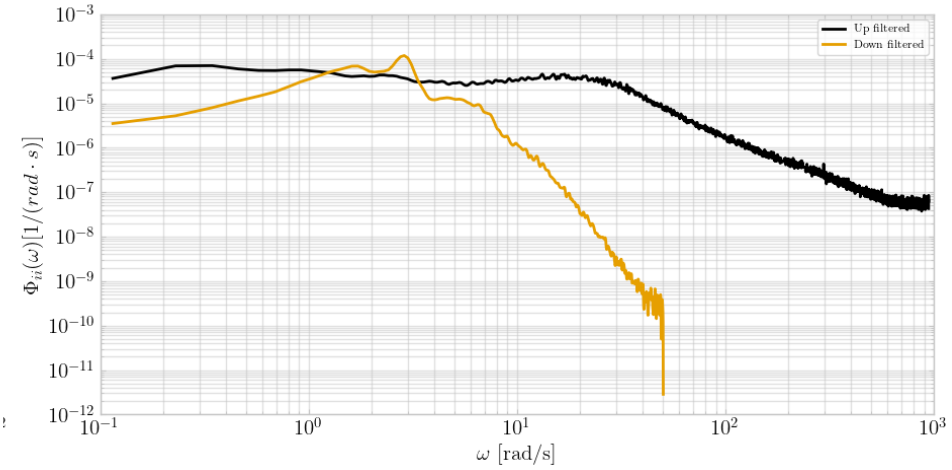

Figure 4.14: Filtered direct gradient PSD

4.3.13. Filtered pressure PSD

The resulting pressure power spectral density after filtering is shown in Figure 4.15. This dataset will be analysed further in chapter 5. The spectrum in Figure 4.15 has already been converted from the temporal domain to the spatial domain. First, the measured frequency was transformed into angular frequency, as shown in Equation 2.28. Then, the angular frequency was converted into the angular wavenumber using the convection velocity, following Equation 2.26 and Equation 2.27. This results in the PSD shown below.

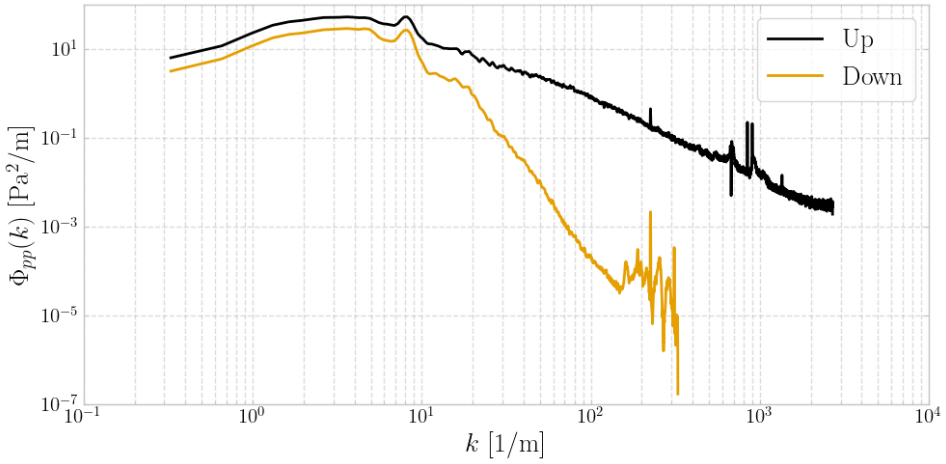

Figure 4.15: Filtered indirect pressure PSD

4.4. Data checks

This section explains the checks that have been performed during the post-processing, either to check the intermediate steps of the analysis or the data processing, or to check assumed coefficients obtained by earlier research.

4.4.1. Variance

The variance check compares two independent methods for determining the variance of the pressure signal. The first method applies Parseval's theorem and evaluates the total area under the power spectral density. The second method obtains the standard deviation directly from the measured time series, using the conventional statistical definition; its square yields the variance. Both approaches are summarised in Equation 4.2.

$$VAR = \sigma^2 = \int_{-\infty}^{\infty} \Phi(f) df \tag{4.2}$$

Where VAR is the variance of the signal, σ is the standard deviation, $\Phi(f)$ is the PSD at a specific frequency (with units of Pa^2/Hz), and f is the frequency in Hz. The PSD describes how the variance of the pressure signal is distributed over frequencies.

4.4.2. Convection velocity

The convection velocity is determined using Equation 2.26 given by Blake, 1970. This can be checked using the cross spectral density, a similar study has been performed by Uijttewaal and Booij (2000).

5

Results & Analysis

This chapter focuses on the results of the physical experiments, for which the data has been processed. The data is analysed using the theoretical substantiation of chapter 2, from which the hypothesis of Thomas, 2023 will be compared to the obtained data. The data analysed in this chapter have been filtered and processed according to the procedures described in chapter 4. The chapter begins with the Pressure spectral analysis in section 5.1, followed by several theoretically substantiated gradient calculation methods to obtain the gradient spectral analysis in section 5.2, the damping of the wave load and current is given in section 5.4, next the water depth influence is visualised, and finally a summary of the test results and analysis is given in section 5.7.

5.1. Pressure Spectral Analysis

In this section the findings of the spectral analysis are demonstrated by showing examples of the pressure spectral analysis. As mentioned in subsection 4.3.3 the welch method is used to obtain the pressure Power Spectral Density.

5.1.1. Current

The results that are shown for the current analysis, the current experiment that is examined in this section is with 30 cm water depth and 8 cm layer thickness, with three different flow velocities. The 30 cm water depth is the shallowest configuration, which allows to reach the highest flow velocities, giving the highest turbulence intensities. To obtain smooth and reliable data the filter methods from section 4.3 have been applied.

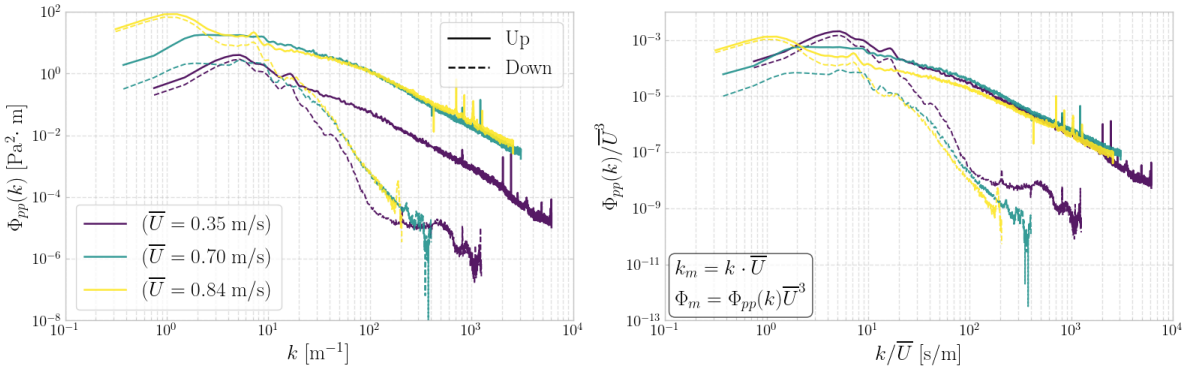

Figure 5.1: Pressure Power Spectral Density – Current – 30 cm water depth – 8 cm layer thickness

Figure 5.1 presents the pressure spectra of the current sequences for three increasing flow velocities, measured at both the upper and lower pressure sensor arrays. The left plot shows the unaltered power spectral densities (PSDs) of the different velocities. The right plot displays the spectra scaled using the time- and depth-averaged velocity, $\overline{U}$.

After scaling, the spectra from the upper array approach a common trend, indicating that the pressure fluctuations largely scale with the mean flow velocity. Although the curves do not collapse perfectly and some deviations remain—especially noticeable on the log–log axes—the overall spectral behaviour shows a consistent scaling tendency across the different flow conditions. The near-collapse suggests that the underlying turbulence structures responsible for the pressure fluctuations evolve in a self-similar manner with increasing velocity. When expressed in scaled, dimensionless form, the spectral energy distribution becomes approximately velocity independent, reflecting a common turbulent production and convection mechanism across the experiments. This interpretation aligns with the findings of Hofland (2005), who demonstrated that near-bed pressure spectra follow a universal shape when scaled by $\overline{U}$ and $\overline{U}^3$, and is further supported by similar velocity-scaling behaviour observed for smooth-wall turbulence by Lee and Sung (2001).

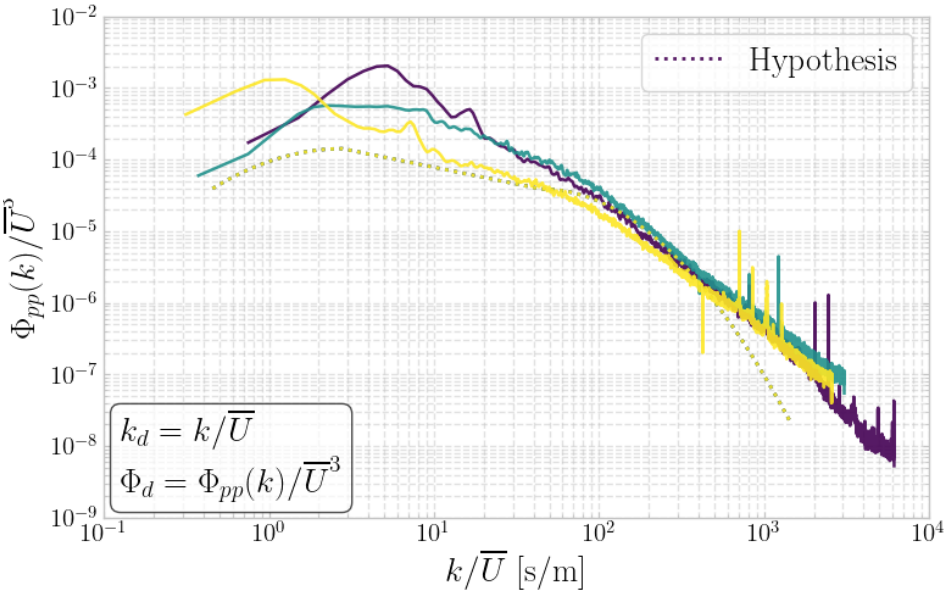

Figure 5.2: Upper Pressure Power Spectral Density with Hypothesis – Current – 30 cm water depth – 8 cm layer thickness

Figure 5.2 presents the scaled pressure spectra measured at the upper array (the filter–top interface) together with the theoretical spectral shape proposed by Thomas (2023), as introduced in subsection 2.6.1. The measured spectra exhibit a broadly similar slope to the hypothesis over the intermediate wavenumber range, but the spectral energy is systematically higher than predicted. This deviation is most pronounced at both the low-wavenumber end, where large-scale turbulent structures dominate, and at higher wavenumbers, where enhanced energy may arise from local flow–bed interactions, sensor noise amplification, or limitations in the assumed scaling. Despite these discrepancies, the overall form of the spectra suggests that the mean-flow scaling captures the dominant energetic trends, although the hypothesis underestimates the magnitude of the fluctuations across the tested flow conditions. The resemblance of the shape is less pronounced in the larger water depths.

5.1.2. Waves

This section shows the results of the pressure PSD of the wave experiments. As shown in subsection 3.6.5 the wave experiments consisted of 4 test cycles, one per layer thickness, each with 7 wave conditions. The first 5 wave conditions follow the irregular spectrum profile and the last two segments are regular wave conditions.

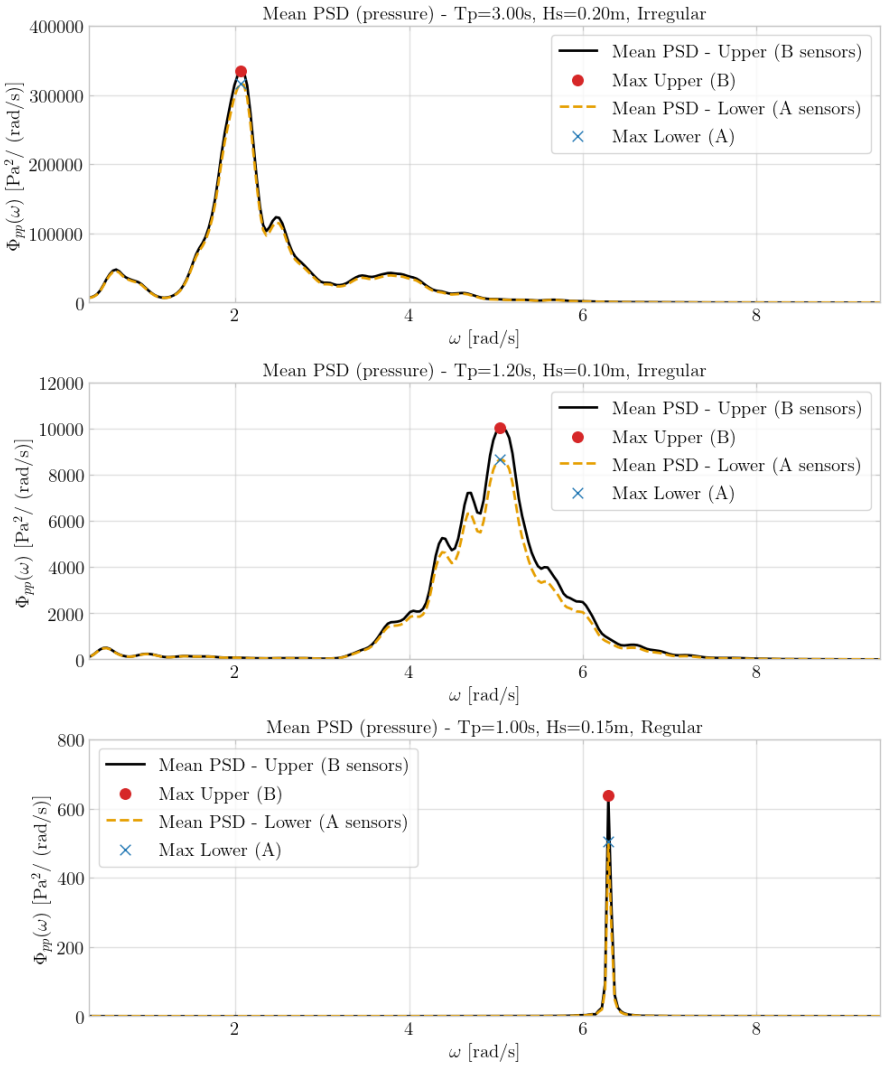

Figure 5.3: Pressure Power Spectral Density - Several wave conditions - 8 cm layer thickness

Figure 5.3 presents representative pressure power spectral densities for three wave conditions, consisting of two irregular sea states and one regular wave train. The upper and lower arrays are shown by the solid black and dashed orange curves, respectively, while the red and blue markers indicate the spectral peak of each array. For the wave-dominated regime, the dominant spectral peak is expected to coincide with the peak wavenumber k_p corresponding to the imposed peak period T_p, as obtained from the linear dispersion relation (Equation 2.30). The spectra are plotted as a function of angular frequency ω with the spectral density $\Phi_{pp}(\omega)$ expressed in units of $\mathrm{Pa}^2/(\mathrm{rad/s})$.

The figure illustrates that each wave condition exhibits a well-defined peak associated with the wave-generator input, with the irregular conditions showing a broader energy distribution and the regular wave condition producing a sharp, narrow-banded peak. Overall, the spectral shapes and peak frequencies agree with expectations for the prescribed wave conditions and validate the frequency-wavenumber conversion used in the subsequent damping analysis.

5.2. Gradient Spectral Analysis

This section shows results and analysis of the conversion from pressure PSD to gradient PSD. The conversion from pressure to gradient used Equation 2.36. This section has a subdivision in three subsections, the results of the indirect gradient method are shown in subsection 5.2.1, the direct method results are shown in subsection 5.2.3 and finally the wave gradient results are shown in subsection 5.2.4, where primarily the indirect method is covered.

5.2.1. Indirect

This section applies the indirect method described in subsection 2.7.1. In this approach, the measured frequency-based spectra are converted into angular wavenumber spectra using the convection velocity, as outlined in subsection 2.5.2. Subsequently, the pressure spectra are transformed into hydraulic gradient spectra through Equation 2.36.

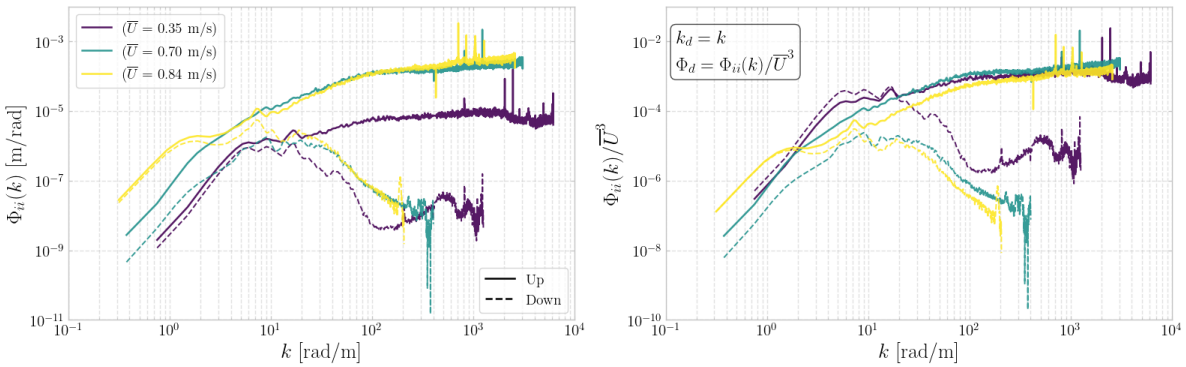

Figure 5.4: Indirect Gradient Power Spectral Density – Current – 30 cm water depth – 8 cm layer thickness

Figure 5.4 is constructed in the same manner as Figure 5.1, using identical water depths, layer thicknesses, and flow velocities as introduced in subsection 5.1.1. The left figure presents the unscaled gradient PSDs for multiple flow velocities, while the right figure shows the same spectra after scaling with the mean flow velocity of each test, following the velocity-based scaling indicated in the legend.

The gradient power spectral density exhibits a pronounced dependence on wavenumber, with spectral energy increasing systematically toward higher k-values. This behaviour arises directly from the wavenumber dependence of the conversion from pressure to gradient spectra in the indirect method. As expressed in Equation 2.36, the transformation includes two constant parameters (water density and gravitational acceleration) and a wavenumber-dependent amplification term. Consequently, higher wavenumbers lead to proportionally larger spectral magnitudes in the gradient PSD, even when the underlying pressure fluctuations do not exhibit the same increase. Consequently, higher wavenumbers amplify the magnitude of the converted spectrum for the indirect method.

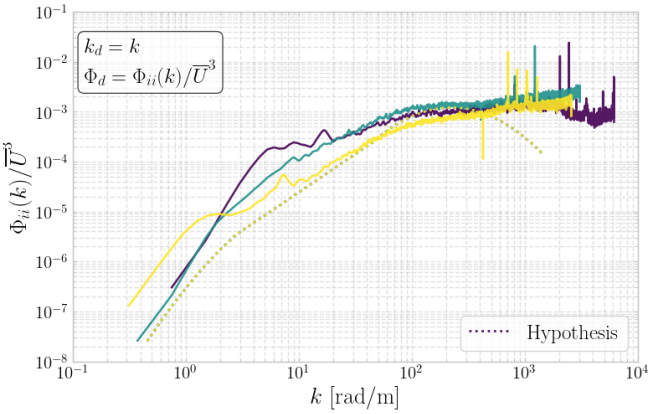

Figure 5.5: Upper Gradient Power Spectral Density with Hypothesis – Current – 30 cm water depth – 8 cm layer thickness

The theoretical hypothesis proposed by Thomas (2023) is included as the dotted line in Figure 5.5. The hypothesis predicts a distinct decay in spectral energy beyond approximately $k \approx 200$ rad/m, reflecting the attenuation of small-scale turbulent structures. The measured spectra show a comparable reduction in magnitude up to roughly $k \approx 400$ rad/m. Beyond this point, however, the decay does not continue as strongly. Instead, the spectra begin to level off, and even display a slight increase, before transitioning into a region characterised by elevated variability at the highest wavenumbers. This behaviour indicates that, although the initial onset of decay is consistent with the theoretical expectation, the high-wavenumber tail is not governed by the same physical mechanism. The flattening and subsequent fluctuations are more likely attributable to measurement noise, limited spectral resolution, or aliasing effects rather than a physical resurgence of turbulent energy.

This deviation suggests that high-frequency fluctuations may be stronger in the measurements than assumed in the theoretical formulation, or that limitations of the experimental setup begin to dominate in this range. Possible contributors include sensor noise, finite sampling resolution, and aliasing, all of which become increasingly influential at very high wavenumbers. The volatility observed in the tail of the spectrum is therefore unlikely to reflect genuine turbulent dynamics and more plausibly arises from these measurement-related effects. Despite these discrepancies, the agreement in the location of the spectral peak and the onset of energy decay indicates that the scaling behaviour proposed by Thomas (2023) remains broadly consistent with the experimental observations.

5.2.2. Premultiplied gradient spectrum

As shown in subsection 4.3.10, this section presents the premultiplied spectra of the indirectly derived hydraulic-gradient signals for the same experiment as before, with a mean velocity of 0.84 m/s, a water depth of 30 cm, and a filter-layer thickness of 8 cm.

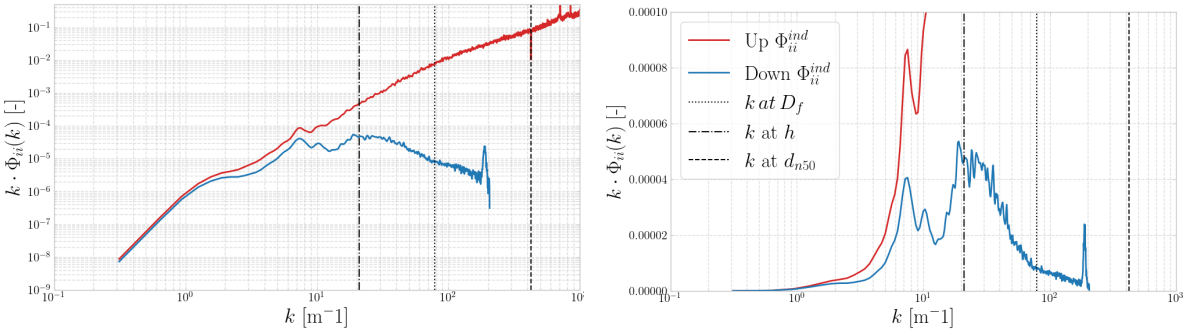

Figure 5.6: Premultiplied hydraulic-gradient spectra, with the full spectrum shown on log–log axes (left) and a zoomed semilog-x view highlighting the filter-base interface (right)

Figure 5.6 displays the premultiplied gradient spectra using two representations. The left panel shows the full spectrum in log-log scaling, illustrating that the gradient signal at the filter-top interface increases monotonically across the resolved wavenumber range. The right panel provides a zoomed semilog-x view of the filter-base interface, revealing three distinct peaks that correspond to different physical processes. The leftmost peak likely represents hydrodynamic wave motion, the middle peak is associated with turbulent pressure fluctuations, and the rightmost narrow peak is most likely an interference component (e.g. structural or pump-induced vibrations). The shape of the lower interface is relatively consistent over all experiments. The three vertical dashed lines indicate the characteristic length scales of the water depth, filter-layer thickness, and nominal rock diameter (from left to right). The spectrum exhibits a steep increase up to the wavenumber associated with the water depth, followed by a gradual decline until the layer-thickness wavenumber, after which the curve begins to flatten. By the wavenumber corresponding to the nominal rock diameter, the spectral energy has effectively vanished. The area below the lower premultiplied spectrum represents the variance used to compute the load parameter $i'_{2\%}$ in section 5.6. This load is primarily governed by the turbulent contribution (the broad mid-range peak), although smaller contributions from hydrodynamic waves and high-wavenumber noise remain present. As a result, the estimated base loading may be slightly overestimated due to these non-turbulent components.

5.2.3. Direct

This section presents the gradient spectra obtained using the direct gradient determination method, as described in subsection 2.7.2. For this analysis, a different experiment is considered than in the indirect method: the water depth is 50 cm, the layer thickness is 8 cm, and the corresponding velocities are shown in Figures 5.7 and 5.8. Similar to the indirect approach, the wavenumber is obtained by applying the convection velocity to convert the temporal spectra into the spatial domain. The lower Pressure Sensor Array (PSA) exhibits approximately the same cut-off wavenumber as observed for the indirect method (before correction), indicating comparable frequency resolution between both approaches.

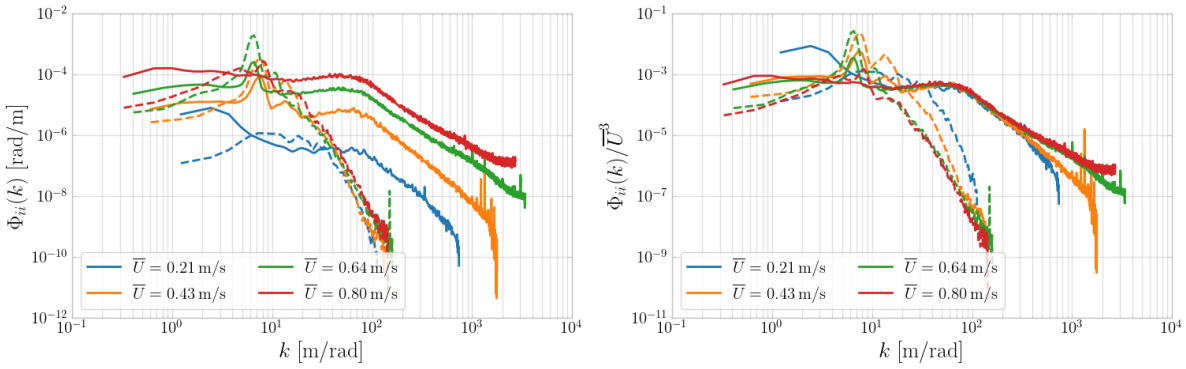

Figure 5.7: Direct Gradient Power Spectral Density - Current - 50 cm waterdepth - 8 cm layer thickness

Figure 5.7 shows that, for some conditions, the spectral energy of the lower PSA slightly exceeds that of the upper PSA at low wavenumbers, implying locally higher hydraulic gradients below the rock layer. In contrast to the indirect spectra shown in Figure 5.4, the directly measured gradient spectra do not exhibit a continuous increase with increasing wavenumber. Instead, the spectral energy reaches a distinct maximum around $k \approx 50$ rad/m, followed by a gradual decay at higher wavenumbers.

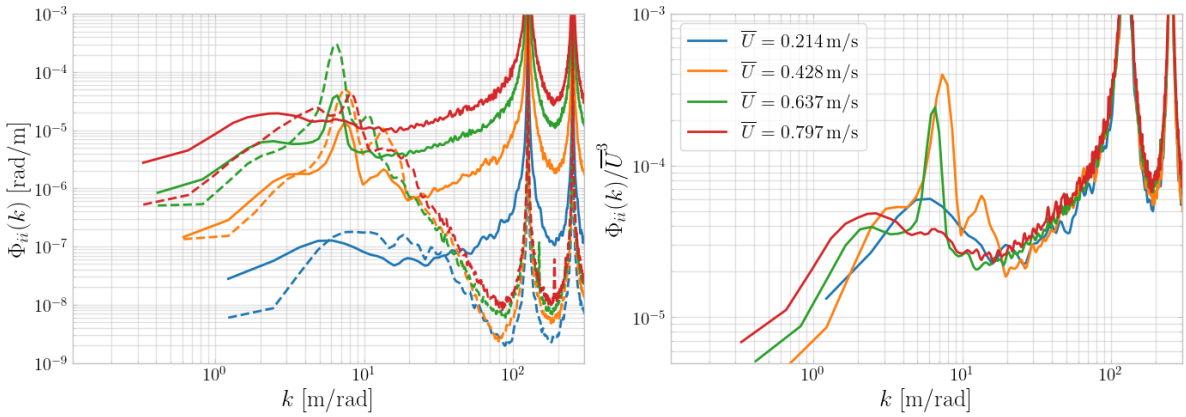

Figure 5.8: Corrected Direct Gradient Power Spectral Density - Current - 50 cm waterdepth - 8 cm layer thickness

Figure 5.8 presents the corrected direct gradient spectrum, obtained by applying the modification factor defined in Equation 3.9. Apart from this correction, the figure corresponds to the same test sequence as shown in Figure 5.7.

5.2.4. Waves

For the wave experiments, the fluctuating hydraulic gradient spectrum was determined using only the indirect method. In contrast to the current experiments, the wavenumber k was obtained from the linear wave dispersion relation. The direct method was not used, as it consistently produced unreliable results for waves (see Figure 5.2.4).

Figure 5.9 presents the gradient power spectral densities for two irregular and a regular wave conditions for an 8 cm filter layer. The spectra display variations in amplitude and bandwidth. A modest increase in spectral energy appears at higher wavenumbers, producing slight broadening of the spectral tail. This behaviour resembles the trend discussed in subsection 5.2.1, though here the effect is much weaker because the wavenumber range only extends to about $k = 6$ rad/m.

At very low wavenumbers ($k < 0.2$ rad/m), the spectral energy fully decays toward zero, indicating that large-scale motions contribute negligibly to the fluctuating hydraulic gradient. This observation suggests that the damping and gradient behaviour are primarily governed by intermediate and high-frequency wave components. The broadening of the spectrum observed for the irregular wave cases does not occur for the regular wave spectra, which are characterised by a single dominant peak containing nearly all the spectral energy.

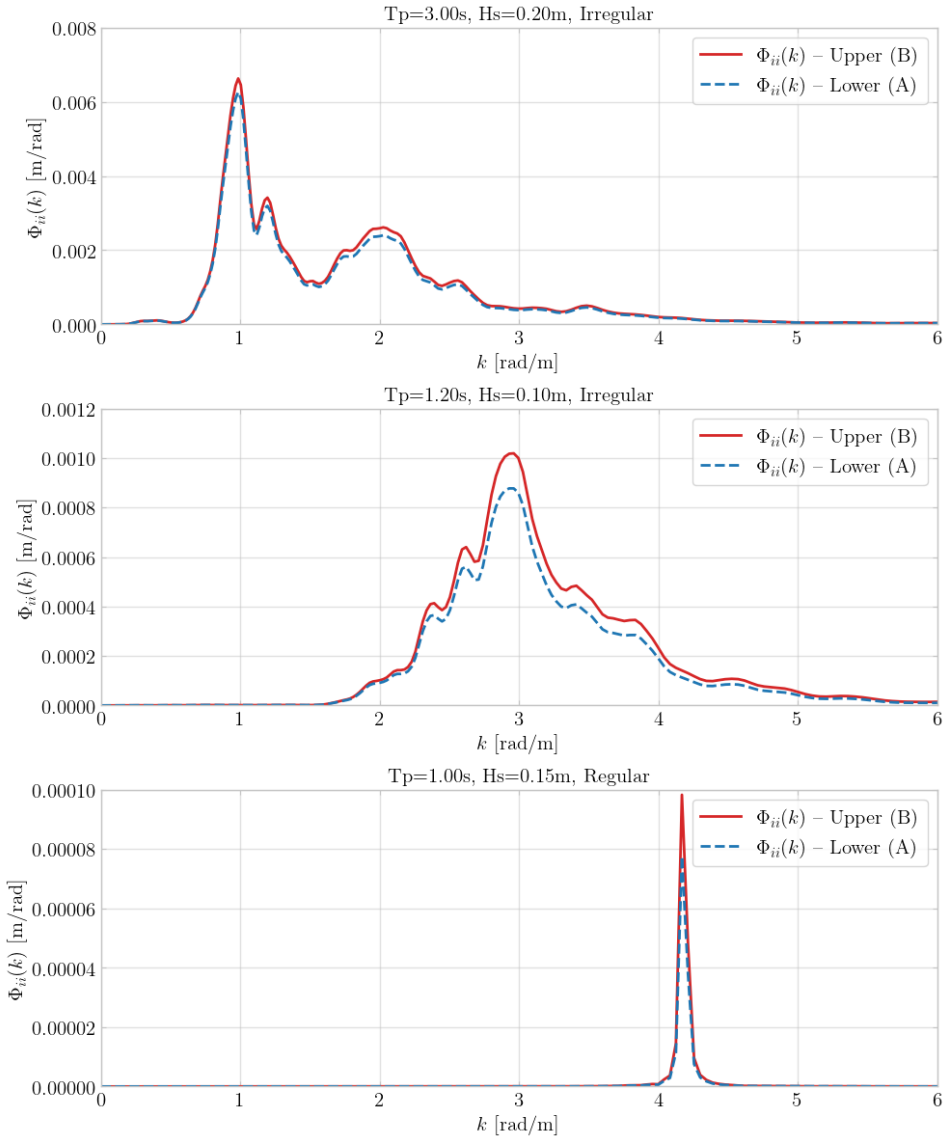

Figure 5.9: Indirect Gradient power spectral density - 8 cm layer thickness

Direct waves method

As noted earlier, the direct method produced inconsistent results for the wave experiments. Figure 5.10 illustrates this: the lower sensor array shows a higher spectral energy density than the upper array, which is physically counter-intuitive for wave loading. Since such inconsistencies occurred systematically across the wave datasets, the direct method is considered unreliable for wave conditions and is therefore excluded from further analysis. The wave sequence in Figure 5.10 corresponds to the first case shown in Figure 5.9.

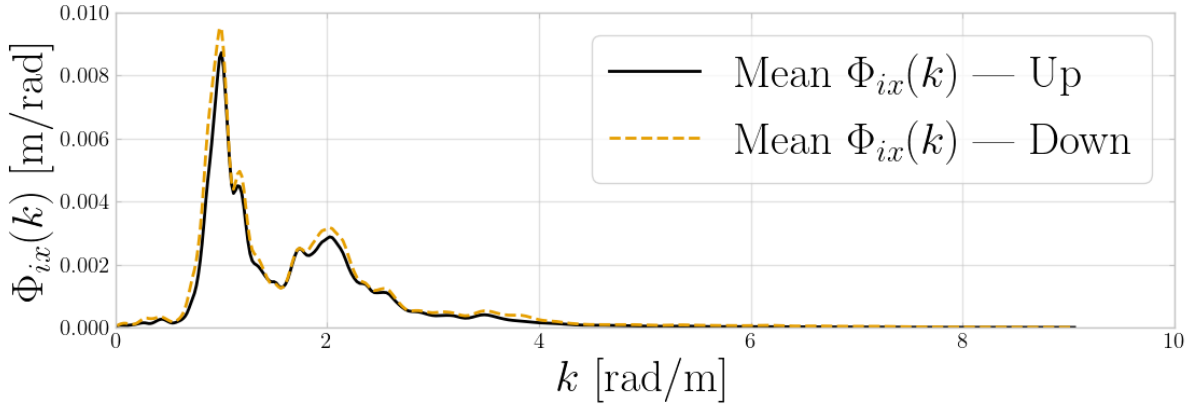

Figure 5.10: Direct gradient power spectral density - 8 cm layer thickness

5.3. Comparing Direct and Indirect Method

This section compares the indirect and direct approaches for determining the fluctuating hydraulic gradient spectrum. Only the current-driven experiments are considered, since the direct method produced unreliable results under wave-induced loading, as discussed in subsection 5.2.4. To highlight the differences and similarities between both methods, two contrasting filter configurations are shown: the thickest layer and the thinnest layer tested, each subjected to the lowest water depth and highest flow velocity.

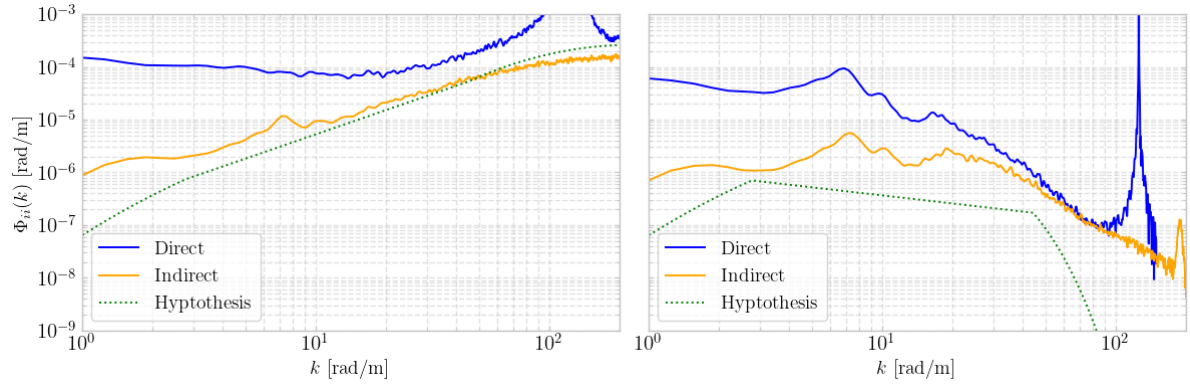

Figure 5.11: Indirect vs. direct method Gradient Spectrum – Current ($U = 0.8\,\mathrm{m/s},\ h = 0.3\,\mathrm{m},\ D_f = 0.08\,\mathrm{m}$). Filter–top interface (left) and filter–base interface (right). **Thickest layer**.

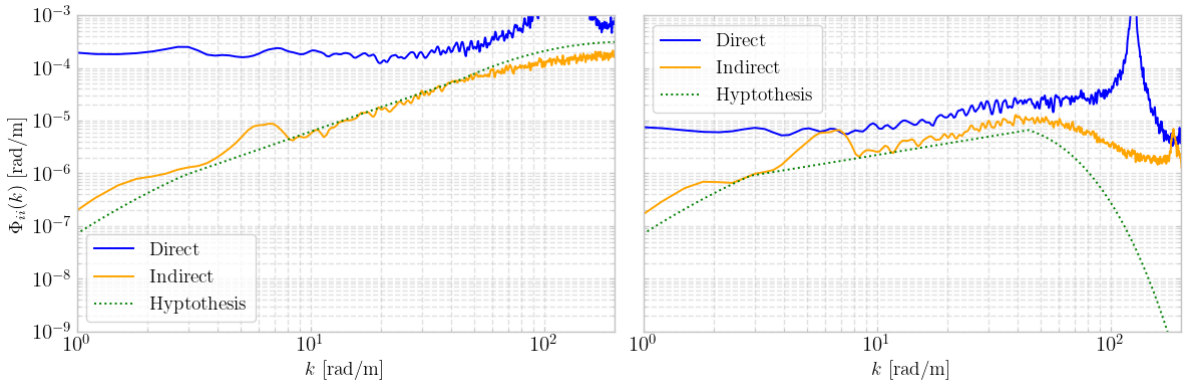

Figure 5.12: Indirect vs. direct method Gradient Spectrum – Current ($U = 0.87\,\mathrm{m/s},\ h = 0.3\,\mathrm{m},\ D_f = 0.04\,\mathrm{m}$). Filter–top interface (left) and filter–base interface (right). **Thinnest layer**.

Figures 5.11 and 5.12 compare the indirect and direct gradient spectra with the hypothesis proposed by Thomas (2023). The dotted line represents the theoretical gradient spectrum: on the left-hand side the pressure-spectrum hypothesis converted to gradient form (subsection 2.7.1), and on the right-hand side the same hypothesis after applying the depth-dependent damping relation (Equation 2.42).

The left panels correspond to the filter-top interface, whereas the right panels represent the filter-base interface. A methodological difference between the two approaches should be emphasised: the direct method uses only the four central pressure sensors, while the indirect method incorporates the full array. As a consequence, any lateral wall effects or asymmetric turbulence near the flume boundaries disproportionately affect the indirect method, since the outer sensors typically measure lower turbulence intensities; these reduced values depress the spatial average and therefore the indirectly obtained spectrum. The direct method, which exclusively employs the data of the middle the sensors, is less sensitive to such influences and generally yields a higher spectral energy level.

At high wavenumbers, the spectra at the filter–base interface are expected to approach a similar decay behaviour. Small-scale turbulent structures (corresponding to high k) are strongly attenuated within the granular layer, causing their associated gradient energy to diminish. This asymptotic decay is visible in both methods, although the indirect method tends to exhibit a smoother approach toward the expected slope.

For the filter–top interface, the indirectly obtained spectra resemble the theoretical shape predicted by the hypothesis for both the thick and thin layers, with only a modest discrepancy in spectral slope and at the tails. At the filter–base interface, the thin-layer case follows the hypothesis reasonably well up to approximately $k \approx 45\,\mathrm{rad/m}$, beyond which the measured energy deviates upward. The direct method shows a weaker agreement with the hypothesis than the indirect method for both interfaces, likely due to its higher sensitivity to small-scale noise amplification and the limited spatial resolution associated with the direct method.

5.4. Damping

This section focusses on the difference between the two interfaces of the filter layer, the damping is defined in a general way in Equation 5.1. subsection 5.4.1 focuses on the damping in the current experiments with generally higher wavenumbers and turbulent pressure fluctuations. subsection 5.4.2 shows the damping of the wave-induced pressure fluctuations.

$$Damping = 1 - \frac{\text{lower gradient}}{\text{upper gradient}} \tag{5.1}$$

5.4.1. Current

The damping for the current is calculated by measuring the difference between the upper and the lower PSD's of the pressure arrays, the PSD's have been determined using the indirect method. The damping is considered per bin of the wavelength, this gives the damping per wavenumber and gives a better idea of how the damping progresses, with higher frequencies and wavenumbers. This also allows to consider the damping better per water level, flow velocity, and layer thickness.

To obtain a stable estimate of the damping as a function of wavenumber, the raw damping values are averaged per discrete wavenumber bin. After converting the spectra to wavenumber space, each segment yields a vector k_i with upper and lower gradient spectra $\Phi_{\text{up}}(k_i)$ and $\Phi_{\text{down}}(k_i)$. The instantaneous damping follows from Equation 5.1:

$$D(k_i) = 1 - \frac{\Phi_{\text{down}}(k_i)}{\Phi_{\text{up}}(k_i)}, \tag{5.2}$$

Because this pointwise ratio fluctuates due to noise and discrete sampling in k, a moving-average binning is applied. For a bin of N samples, the bin-averaged damping becomes

$$\widetilde{D}(k_i) = \frac{1}{N} \sum_{j=i-(N-1)/2}^{i+(N-1)/2} \left(1 - \frac{\Phi_{\text{down}}(k_j)}{\Phi_{\text{up}}(k_j)}\right), \tag{5.3}$$

with the corresponding bin-averaged wavenumber

$$\widetilde{k}_i = \frac{1}{N} \sum_{j=i-(N-1)/2}^{i+(N-1)/2} k_j. \tag{5.4}$$

This binning smooths local fluctuations while preserving the underlying damping trend, enabling clearer comparison across flow conditions and with the theoretical curve.

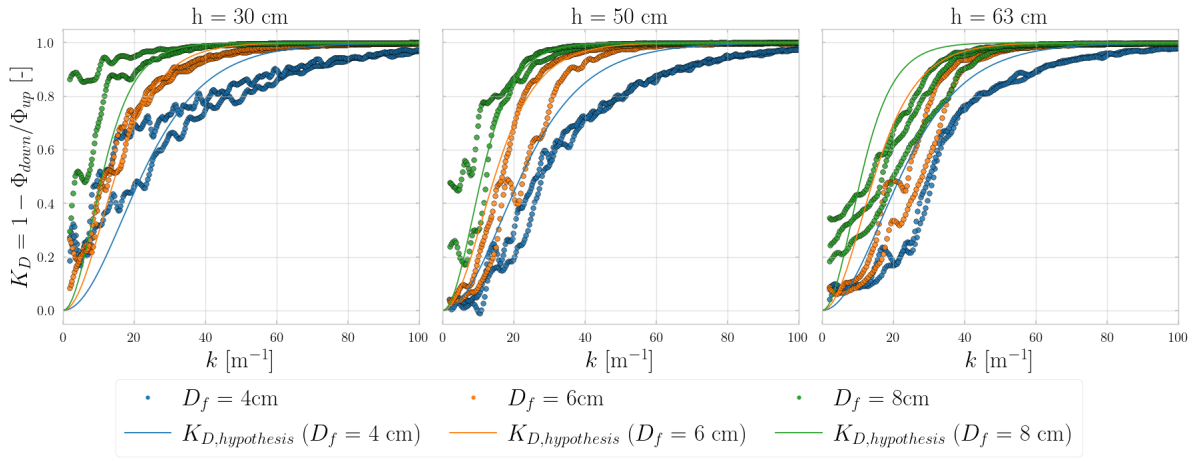

Figure 5.13: Current damping per water level in relation to wavenumber

Figure 5.13 shows the damping per wavenumber, there are three hypotheses plotted, these are each per the used layer thickness. This plot shows the hypothesis for the damping per layer thickness, in Figure 5.14 is the layer thickness one of the variables and only one hypothesis

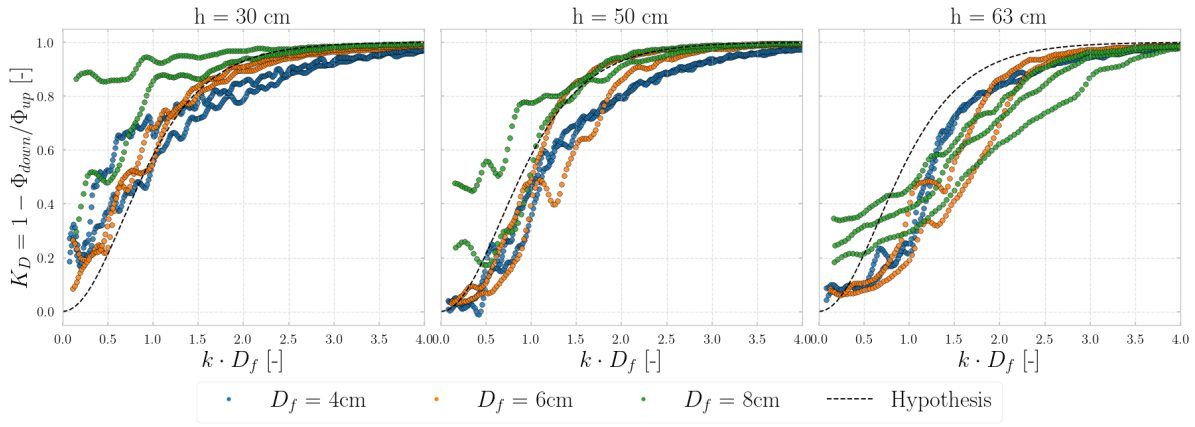

Figure 5.14: Current damping per water level vs kD_f

Figure 5.14 presents the measured damping behaviour for the three investigated water depths (30 cm, 50 cm, and 63 cm), representing increasing water depths from left to right. The black dashed line in each subplot denotes the theoretical damping relationship introduced in section 2.8. Since the damping is derived from the variance of the pressure fluctuations rather than their standard deviation, the theoretical curve reflects the expected variance-based damping response.

For the lowest water depth ($h = 30$ cm), corresponding to the highest mean flow velocities, the measured damping exceeds the theoretical prediction, particularly in the low-wavenumber range. This indicates that the filter layer attenuates turbulent energy more efficiently than anticipated under these energetic flow conditions. The intermediate case ($h = 50$ cm) follows the theoretical trend very closely for the medium layer. It shows significant coherence between the hypothesis and all the layer thicknesses, suggesting a consistent scaling between the measured and predicted damping behaviour. In contrast, for the deepest flow ($h = 63$ cm), the overall damping is reduced compared with the shallower tests, implying that the lower flow velocities at this depth produce weaker pressure fluctuations and less energy loss across the layer. Across all water depths, the results confirm that layer thickness has a pronounced effect in the low-wavenumber domain, where thicker layers yield greater damping of large-scale turbulent pressure fluctuations. At higher wavenumbers, however, the differences between layer thicknesses diminish, suggesting that small-scale pressure fluctuations are less affected by total layer thickness and are instead governed by local pore-scale processes within the filter material.

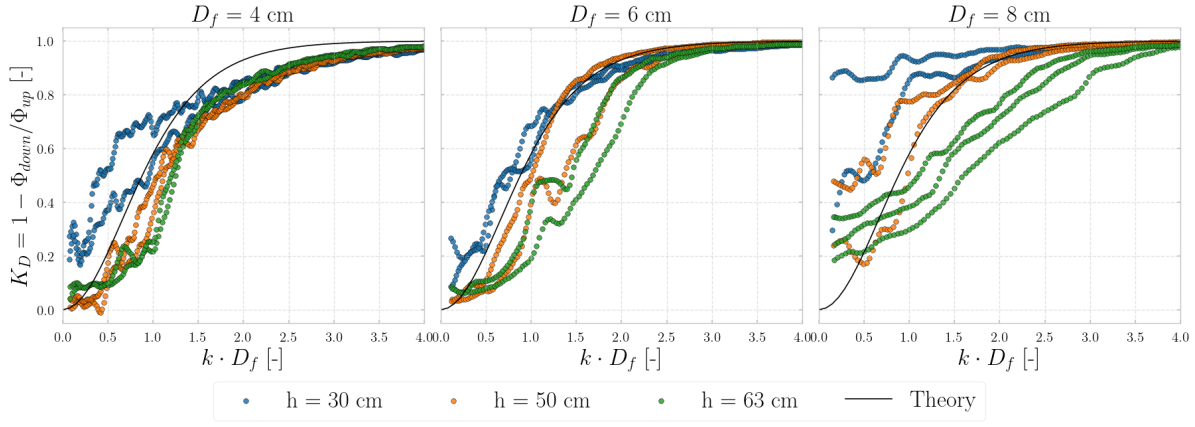

Figure 5.15: Current damping per layer thickness (D_f)

Figure 5.15 presents the measured damping behaviour for the three layer thicknesses investigated: 4 cm, 6 cm, and 8 cm (from left to right). The thinnest layer ($D_f = 4$ cm) exhibits limited damping in the low-wavenumber range, after which the damping rapidly increases with increasing kD_f. For this configuration, the lowest water depth shows moderate damping at low wavenumbers, while the highest water depth exhibits little to no damping and even slight negative values.

The intermediate layer thickness ($D_f = 6$ cm) follows the theoretical damping trend closely, showing a realistic relationship where lower water depths (higher flow velocities) result in stronger damping compared to conditions with larger water depth. For the thickest layer ($D_f = 8$ cm), damping occurs even at relatively low wavenumbers, demonstrating that thicker filter layers enhance the attenuation of pressure fluctuations throughout a wider spectral range.

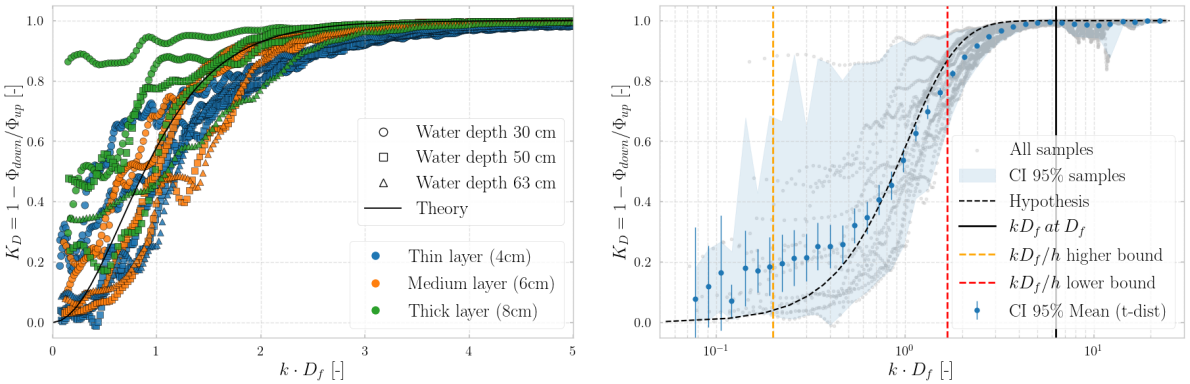

Figure 5.16: Damping all current experiments combined (left), mean of all experiments combined (right)

The left-hand plot in Figure 5.16 displays the damping results for all test conditions, showing each combination of water depth and layer thickness on linear axes. This visualisation highlights the general consistency of the experimental results with the theoretical damping curve, while also illustrating the spread caused by varying hydraulic conditions.

In the figure, the circles, squares and triangles show the 30 cm, 50 cm and 63 cm water depth respectively. The blue, orange and green markers correspond to the 4 cm, 6 cm and 8 cm layer thicknesses. The right-hand plot presents the same dataset in a binned representation on a logarithmic $k \cdot D_f$ scale. Within each bin, the mean damping value is computed, and its uncertainty is shown using a 95% confidence interval based on the Student-t distribution. For a bin with n samples, this interval is given by

$$\overline{D} \pm t_{0.975}(n-1)\,\frac{\sigma_s}{\sqrt{n}},$$

where $\overline{D}$ is the bin-averaged damping and σ_s the corresponding sample standard deviation. The t distribution is used instead of the normal distribution because each logarithmic bin contains a limited number of samples; with small n, the uncertainty in the estimated variance is larger, and the mean no longer follows a normal sampling distribution. The heavier tails of the t distribution account for this, yielding a more reliable confidence interval for the bin-mean.

The shaded central 95% band represents a different measure: it shows the empirical spread of the individual samples in each bin, bounded by the 2.5th and 97.5th percentiles. Together, the t-based confidence interval (uncertainty of the mean) and the central 95% band (variability of the samples) provide a clear statistical view of the mean damping trend and its scatter relative to the theoretical relationship.

As proposed in subsection 5.2.2, the spectra can be subdivided into three characteristic regions: a hydrodynamic-wave region at low wavenumbers, a turbulent region at intermediate wavenumbers, and a noise-dominated region at high wavenumbers. The transitions between these regions are expected to scale with key geometric parameters, in particular the water depth and the filter-layer thickness.

In the right-hand panel of Figure 5.16, the three vertical lines indicate the relevant geometric wavenumber scales. The orange line corresponds to the smallest water depth in combination with the largest layer thickness, the red line to the largest water depth together with the smallest layer thickness, and the black line to the wavenumber associated with the layer thickness itself. These scales approximate the expected transitions between the hydrodynamic-wave region, the mixed hydrodynamic–turbulent regime, the predominantly turbulent domain, and the noise-dominated tail at high wavenumbers. This framework helps interpret the damping behaviour across the different test conditions; for example, the green circular markers (thick layer, shallow depth) only enter the fully turbulent region beyond the red line, consistent with their smaller depth and larger layer thickness and the resulting shift of the turbulence transition toward higher values of kD_f. The quantitative comparison between the measured mean damping and the theoretical curve yields an **RMSE of 0.078**, corresponding to an average deviation of less than 8% over the full 0–1 damping range. This agreement would improve further if the uncertain low-wavenumber values were excluded. This level of deviation shows that the hypothesis captures the dominant spectral trends while still allowing for moderate discrepancies, particularly around the transition between hydrodynamic and turbulent regimes.

Overall, the results confirm that damping increases with layer thickness, particularly in the low-wavenumber domain. A reduction in water depth, and thus an increase in mean flow velocity, also results in relatively greater damping of the turbulent pressure fluctuations.

5.4.2. Waves

To quantify the wave damping, the zero-order spectral moment (m_0) of the wave spectra was calculated, representing the total variance of the spectrum. The square root of this variance yields the standard deviation of the surface elevation signal. The ratio between the standard deviations of the lower and upper sensor arrays provides a measure of the relative energy attenuation. The damping coefficient, defined in Equation 5.5, expresses the fractional reduction in wave energy between the two levels:

$$Damping = 1 - \frac{\sigma_{lower}}{\sigma_{upper}} = 1 - \frac{\sqrt{m_{0,lower}}}{\sqrt{m_{0,upper}}} \tag{5.5}$$

Figure 5.17 presents the resulting wave damping values, plotted as a function of the peak wavenumber multiplied by the layer thickness for each wave sequence. The blue line represents the theoretical damping relationship proposed by Thomas (2023). The coloured markers correspond to the experimental results for different filter layer thicknesses: green, orange, and blue for 8, 6, and 4 cm respectively. Marker size is scaled with wave height, indicating that larger symbols correspond to larger incident waves. The gradients have been obtained using the indirect method as discussed in subsection 5.2.4, where was concluded that the direct method gave unreliable results. The irregular wave sequences are shown with filled markers and the regular waves are shown with the outline of the markers. Figure 5.17b zooms in on the graph showing that the damping for the wave sequences is below 15%. Where the regular waves with a peak period of 1 second, experiences the most damping.

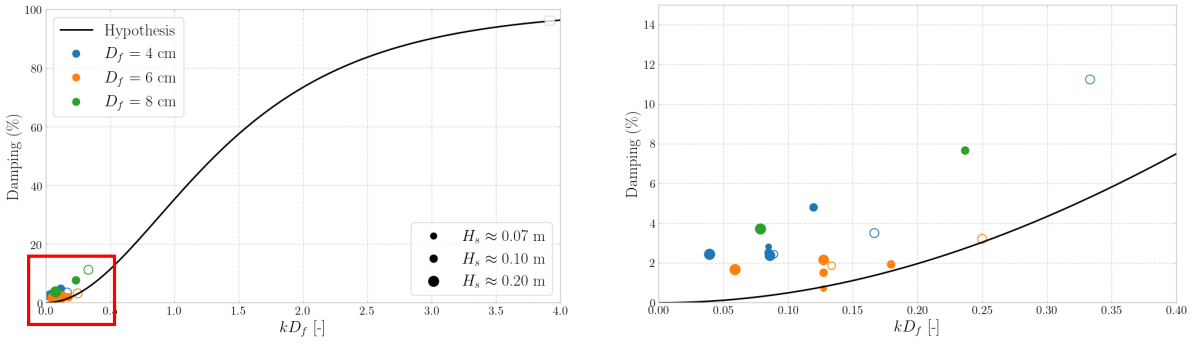

(a) Full range with zoom region (red).

(b) Zoomed view of the highlighted window.

Figure 5.17: Damping comparison: full plot and zoomed window. The red rectangle in a indicates the domain shown in b.

5.5. Water depth Influence - Current

This section dives into the influence of the water depth on the spectral shape and the damping. The assessment of the damping also looks into the relation between the water depth and the layer thickness.

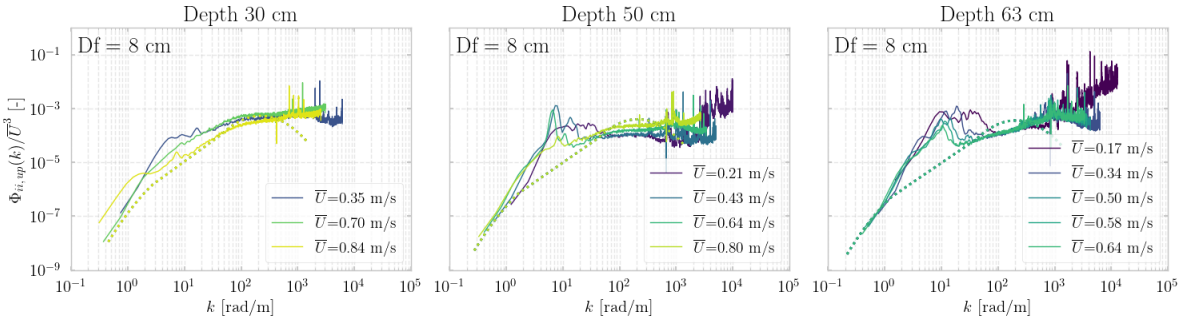

Figure 5.18: The gradient power spectral densities of at different depths - $D_f = 8$ cm

Figure 5.18 presents the scaled gradient spectra for the current experiments with a filter layer thickness of 8 cm. The spectrum corresponding to the 30 cm water depth aligns closely with the theoretical prediction of Thomas (2023), particularly across the intermediate wavenumber range. At higher wavenumbers, the measurements begin to diverge. For larger water depths (50 cm and 63 cm), a distinct peak appears at lower wavenumbers for the 50 cm water depth, and a wider peak, reaching lower wavenumbers, appears at the 63 cm water depth. This phenomenon reflects the dominance of larger, more energetic flow structures associated with conditions for flow in larger water depths. In these cases, the spectra deviate earlier and more strongly from the theoretical trend at higher wavenumbers. Across all depths, an increase in mean flow velocity results in improved agreement with the theoretical spectrum, extending the range over which the measured data follow the predicted behaviour. This demonstrates that turbulence intensity enhances the validity of the spectral similarity.

The influence of water depth is only relevant for the current-induced flow conditions, since the water depth remained constant during the wave experiments. Moreover, the physical mechanism behind the wave-induced pressure fluctuations differs fundamentally from that of the turbulent current flow. Under wave action, the pressure oscillations are primarily hydrostatic and only weakly dampened within the filter layer, as visible in Figure 5.17. Including these cases in the Figure 5.19 would therefore lead to a misleading representation of the damping behaviour, which is driven by turbulence in the current experiments.

Van de Sande Test

To evaluate the observed damping in this study, the results are compared with the experimental findings of Van de Sande (2012). From the experimental programme, only the water depth of the high-intensity turbulence tests conducted with a sill (T06b and T06c) are directly usable, as these were the only tests for which the water depth was explicitly documented.

The relevant test conditions from Van de Sande (2012) are those in which the base material experienced winnowing. In their study, three categories of failure were investigated: (i) failure of the top layer, (ii) failure of both the top and base layers, and (iii) failure of only the base layer. For comparison with the present work, only the latter two categories are considered.

Assuming the same water depths as tests T06b and T06c for the remaining experiments, the corresponding ratios of water depth to filter thickness fall approximately in the range of $2.5 \leq h/D_f \leq 10$. The upper bound of this range is primarily caused by an extremely thin filter layer of only $1.08\,d_{f50}$. Such a thickness is unlikely to be applied in practice. For offshore scour protection, Deltares (2023) recommends a minimum thickness of $7\,d_x$ and a maximum of thickness of $12\,d_x$, where

$$d_x = \max\left(d_{15},\, \frac{d_{50}}{1.5}\right).$$

A layer as thin as $1.08\,d_{f50}$ provides only marginal attenuation of turbulent loads, resulting in minimal damping. Consequently, the damping behaviour observed in the corresponding tests of Van de Sande (2012) is not representative of the trends observed in this thesis, as illustrated in Figure 5.19.

The study also employed pressure-difference meters, with two sensors positioned above and two below the filter layer. However, it was found that the fluctuations introduced by the measurement equipment dominated the recorded signal, making reliable assessment of the damping impossible. In contrast, the present study uses high-frequency pressure sensors capable of accurately resolving turbulent fluctuations, allowing the damping behaviour to be quantified with confidence.

The damping of the standard deviation is derived from the variance of the turbulent pressure signal, which is obtained from the zero-order spectral moment of the power spectral density, as calculated in subsection 5.4.2. The relationship between variance and standard deviation is given in Equation 4.2.

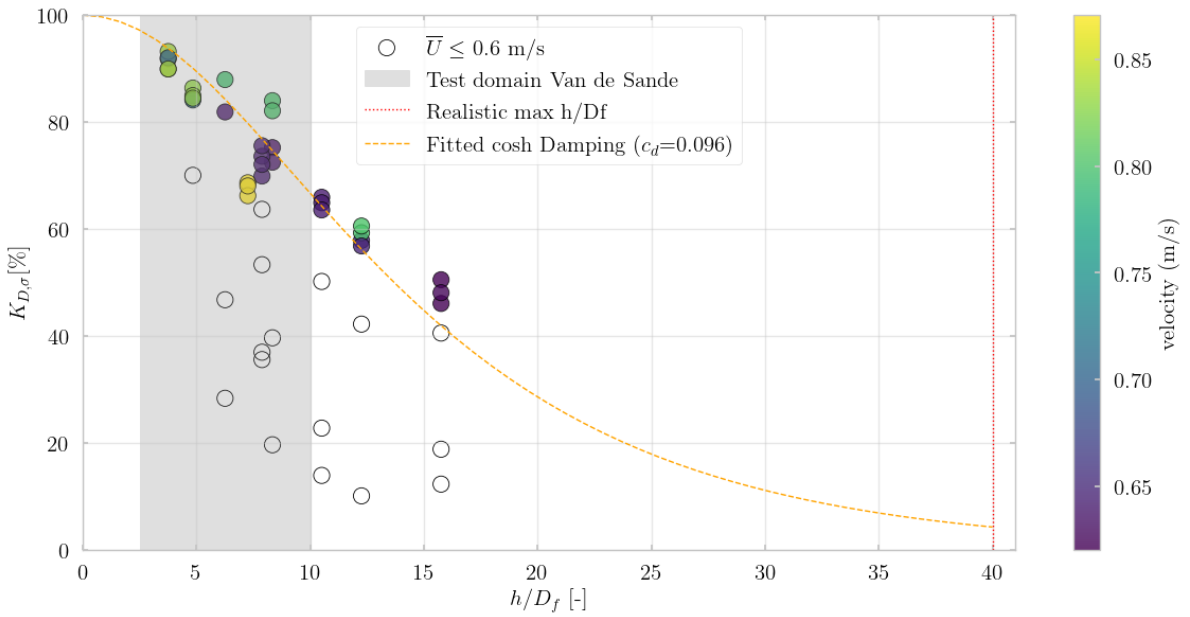

Figure 5.19: Damping of the standard deviation in turbulent flow in relation to the water depth and filter thickness

Figure 5.19 demonstrates a general trend of decreasing damping with increasing water depth and decreasing filter thickness, this trend is fitted using the format in Equation 5.6. In other words, flows in larger water depths exhibit a smaller reduction across the filter layer. This behaviour can be explained by the greater hydraulic load imposed on the filter due to the higher flow energy and larger-scale turbulent structures associated with greater water depths. These energetic eddies are less susceptible to attenuation over short vertical distances, leading to a lower effective damping ratio.

$$K_{D,fit} = \frac{1}{\cosh\left(c_d \cdot h/D_f\right)} \tag{5.6}$$

The colour scale represents the mean flow velocity, which appears to influence the damping only indirectly. Higher velocities increase the overall turbulent loading on the bed, and therefore also increase the absolute load transmitted to the base of the filter. However, this does not alter the damping behaviour, which is primarily controlled by geometric properties such as the water depth and layer thickness. Although a slight reduction in velocity is observed for larger water depths, this effect is due to experimental boundary conditions and pump limitations rather than a hydraulic dependence of damping on velocity. The absence of a systematic velocity trend confirms that the damping is governed mainly by geometry, the water depth and filter-layer thickness, while the flow intensity affects only the magnitude of the imposed loading, not the damping efficiency itself.

5.6. Loading

The loading on the base, defined in section 2.9, can be found using the standard deviation of the array at the base/filter-interface. Using the assumed Rayleigh distribution and Equation 2.44, the $i'_{2\%}$ is determined per test condition, each circle represents one test sequence.

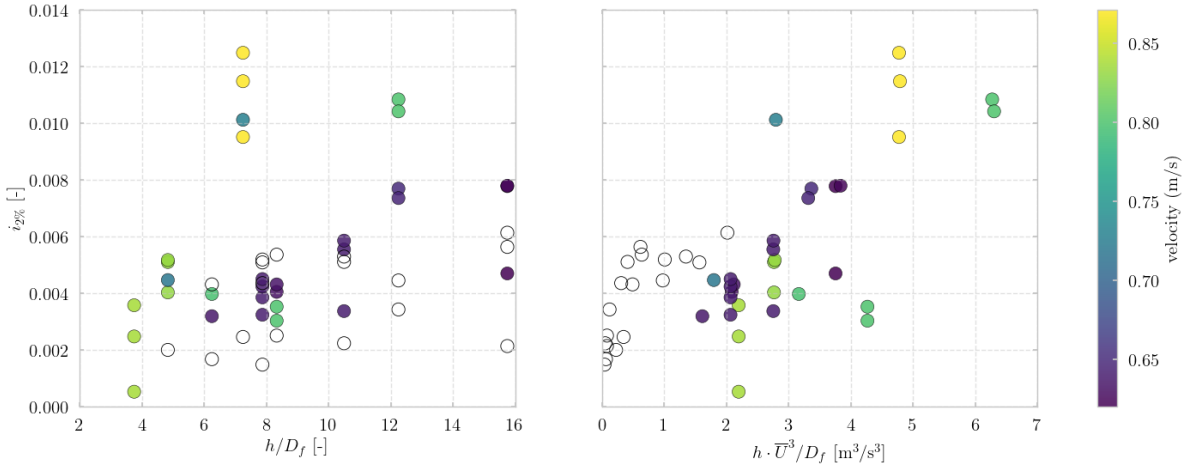

Figure 5.20: $i'_2\%$ Plotted against the water depth and layer thickness h/D_f (left) and $i'_2\%$ Plotted against $h\overline{U}^3/D_f$ (right)

The left figure in Figure 5.20 shows the load in the dimensionless $i'_{2\%}$ on the y-axis and the ratio between water depth and layer thickness h/D_f on the x-axis. This parameter expresses how deep the flow is relative to the thickness of the granular layer and therefore indicates the degree to which the turbulent structures generated in the water column can penetrate into the filter. In the right-hand figure, the x-axis is scaled by $h\overline{U}^3/D_f$, which incorporates the mean flow velocity and therefore reflects the turbulent kinetic input per unit filter thickness. This velocity-based scaling highlights the influence of flow intensity on the loading at the base. In both figures, empty circles denote test sequences with $\overline{U} < 0.6$ m/s, which are not considered in the main interpretation due to their comparatively low turbulence intensity. These lower-velocity conditions are shown explicitly for completeness, consistent with the presentation approach used in Figure 5.19.

The colorbar in both plots represents the mean flow velocity $\overline{U}$ of each test sequence. Higher velocities appear in yellow-green tones, while lower velocities are shown in purple. This allows the influence of flow intensity to be visually distinguished within each h/D_f or $h\overline{U}^3/D_f$ interval.

5.7. Summary of Data Results & Analysis

This chapter presented the results of the physical experiments and the subsequent spectral analyses of the pressure and hydraulic gradient measurements. The findings were evaluated within the theoretical framework of chapter 2, with specific reference to the spectral hypotheses proposed by Thomas (2023). The data were filtered, processed, and interpreted using the procedures outlined in chapter 4, enabling a consistent comparison across all loading scenarios.

The pressure spectral analysis demonstrated that, under current-induced flow conditions, the spectra measured at different velocities collapse onto a nearly universal curve when scaled by the mean flow velocity $\overline{U}$. This behaviour confirms that the pressure fluctuations exhibit dynamic similarity across test conditions and are governed primarily by velocity-dependent turbulent production mechanisms, consistent with the observations of Hofland (2005). Under wave loading, the spectral response differs fundamentally: regular waves yield narrow-banded, steep spectral peaks, while irregular waves produce broader spectra reflecting the imposed wave-energy distribution.

The gradient spectral analysis revealed distinct differences between the indirect and direct calculation methods. The indirect method, which converts pressure spectra using a k-dependent amplification term, displayed an increase in spectral energy at higher wavenumbers, reflecting the mathematical structure of Equation 2.36. The theoretical model of Thomas (2023) predicts a decay beyond $k \approx 200\ \mathrm{rad/m}$, and the experimental data showed a comparable shape, until $k \approx 400\ \mathrm{rad/m}$, after which it deviates from the theory and starts to climb. The divergence and variability in the high-wavenumber range likely caused by measurement noise, aliasing, or sensor-resolution limits. The direct method produced smoother spectra, characterised by a peak around $k \approx 50\ \mathrm{rad/m}$ followed by a gradual decay, before the correction is applied. However, its usable wavenumber range is restricted by the sampling interval $\Delta x = 0.05\ \mathrm{m}$, limiting reliable interpretation to approximately $k < 60\ \mathrm{rad/m}$. Overall, both methods capture the main spectral trends, but the indirect method is more suitable for high-wavenumber interpretation, whereas the direct method provides clearer information in the low-to-intermediate range.

For wave-induced conditions, the gradient spectra remained bounded within a relatively small wavenumber range ($k < 6\ \mathrm{rad/m}$), producing only minor spectral broadening for irregular waves. The regular waves exhibited a sharp dominant peak, consistent with their single-frequency nature. At very low wavenumbers, the spectral energy approached zero, indicating negligible contribution from large-scale motions to the fluctuating hydraulic gradient.

The damping analysis established that reduction of turbulent fluctuations depends primarily on geometric ratios, most notably the filter thickness D_f and the relative water depth h/D_f. Thicker layers produced stronger damping across a broad wavenumber range, with the effect most pronounced at low wavenumbers corresponding to large-scale turbulent structures. Increasing water depth reduced the effective damping, as larger-scale eddies generated in larger water depths experience less damping over the filter thickness. Mean flow velocity exerted only an indirect influence, by influencing the total load on the bed, the relative damping was unaltered by an increase in flow velocity. Under wave loading, damping remained weak ($< 15\%$), consistent with the predominantly hydrostatic character of wave-induced pressure fluctuations.

The loading analysis, expressed through the exceedance parameter $i'_{2\%}$, showed comparable dependencies. Load intensity increased with relative depth h/D_f and, when scaled by $h\overline{U}^3/D_f$, exhibited a clear relationship with the turbulent kinetic input per unit filter thickness. The velocity-dependent colour scale and the exclusion of low-velocity conditions ($\overline{U} < 0.6$ m/s) demonstrated that loading is dominated by energetic turbulent events. Overall, the results indicate that damping is governed mainly by geometric parameters, particularly filter thickness and water depth, whereas the loading at the base depends on both hydrodynamic forcing and geometric configuration.

Overall, the results indicate that the spectral behaviour of pressure and gradient fluctuations, as well as their damping through the filter layer, are broadly consistent with the underlying theoretical principles. The experimental trends suggest that geometric scaling, rather than absolute flow intensity, plays a dominant role in governing the attenuation of turbulent fluctuations in granular filter layers. These observations lend support to the theoretical model of Thomas (2023) and provide a coherent basis for the discussion presented in the following chapter.

6

Discussion

This chapter interprets the experimental findings presented in chapter 5, linking the observed spectral behaviour and damping characteristics to the underlying physical mechanisms and theoretical framework of Thomas (2023). The discussion critically examines the consistency between directly and indirectly derived gradient spectra, the influence of layer thickness and water depth on damping performance, and the potential sources of experimental uncertainty that may have affected the measured results. Emphasis is placed on the validity and limitations of the applied hydrostatic and convection-based assumptions, as well as on the spatial and spectral resolution constraints inherent to the measurement setup. Through this analysis, the chapter aims to assess the reliability of the derived spectral relationships, identify systematic deviations from theory, and outline the conditions under which the experimental data most accurately represent the physical damping behaviour of open filter layers.

6.1. Discrepancies Between Hypothesis and Experimental Data

The comparison between the hypothesis of Thomas (2023) and the experimentally obtained gradient spectra (indirect method) shows generally consistent behaviour across the low- and mid-wavenumber range, but several systematic deviations emerge that are important for interpreting the applicability and limitations of the theoretical model.

At the filter-top interface, the indirectly derived spectra reproduce the theoretical slope and overall spectral shape for both the thick and thin layers. The agreement is broadly similar across the two configurations, with only minor deviations in curvature and spectral energy that likely reflect measurement variability rather than systematic layer-thickness effects.

At the filter-base interface, the deviations become more pronounced. For both the thin and thick layers, the measured spectra follow the predicted decay only up to approximately $k \approx 40$–$50\ \mathrm{rad/m}$. Beyond this range, the experimental energy does not continue the sharp theoretical roll-off but instead plateaus or rises slightly. This behaviour reflects the limited ability of the filter layer to reduce the smallest turbulent scales. In practice, high-wavenumber fluctuations are not fully removed, particularly when small turbulent structures are able to propagate into the pore space of the granular layer. Additionally, noise amplification toward the upper spectral limit becomes more influential because the physical pressure fluctuations are small compared with the noise floor of the measurement system.

The mismatch at high wavenumbers is therefore attributed to two mechanisms: (1) *physical*-the granular layer does not exhibit the idealised exponential damping assumed in the hypothesis, particularly for thin layers. In addition, local surface irregularities (e.g. a missing stone) can create pathways that allow small-scale turbulent fluctuations to reach the underside of the layer; and (2) *methodological*-the spectral conversion amplifies residual small-scale noise, which becomes dominant where the true gradient energy is minimal. Despite these discrepancies, the overall trends remain consistent with the theoretical framework: increasing layer thickness enhances damping, and the observed spectra broadly reflect the predicted turbulent shaping.

6.2. Comparison Between Direct and Indirect Gradient Spectra

The comparison between the direct and indirect gradient spectra reveals several systematic discrepancies that are essential for interpreting both methods. While the detailed results were presented in chapter 5, the discussion here focuses on the underlying mechanisms that explain these differences and their implications for the reliability of each approach.

A first distinction arises from the theoretical basis of the indirect method, which applies a hydrostatic pressure-gradient conversion. This approach inherently increases the k-dependence of the spectrum, amplifying small-scale (high-k) fluctuations. At these scales, however, the hydrostatic assumption breaks down due to inertial pressure fluctuations, pore-scale turbulence, and phase differences between pressure and gradient signals. Consequently, the indirect method produces an ascending curve at high k, consistent with the hypothesis of Thomas (2023), whereas the direct method displays a flatter spectrum up to approximately $k \approx 50\,\mathrm{rad/m}$, after which it starts to ascend due to the correction equation

The direct method introduces its own limitations, primarily due to the measurement–spacing transfer function associated with estimating the gradient from two pressure sensors separated by Δx. For a sinusoidal pressure signal, the measured gradient scales with $\sin(k\Delta x)$ rather than the physically correct k–scaling of the analytical derivative (see Equation 2.37). The transfer function in Equation 3.8 compensates for this effect, but its inversion becomes increasingly sensitive at wavenumbers where $\sin(k\Delta x)$ approaches zero. Consequently, small uncertainties in the pressure measurements are amplified at high k, reducing the reliability of the corrected direct spectrum beyond approximately $k \approx 80\,\mathrm{rad/m}$.

A second important source of discrepancy stems from the different spatial sampling of both methods. The indirect method incorporates all pressure sensors across the flume width, including those near the sidewalls, where turbulence intensities are lower. This reduces the spatially averaged pressure spectrum and, by extension, the indirectly derived gradient spectrum. In contrast, the direct method relies exclusively on the four centrally positioned sensors and is therefore less influenced by boundary effects. As a result, the direct method generally yields higher spectral energy, particularly at the filter–top interface where wall-induced damping is minimal.

Additional uncertainty enters the current-induced spectra through the ω-k conversion, which uses the convection velocity approximation $d\omega/dk \approx U_c = 0.44\,\overline{U}$. Derived from the aerodynamic experiments of Blake (1970), this value may be imperfectly suited to free-surface hydrodynamic flows. The wave experiments, by contrast, rely on the linear dispersion relation, which is more robust for oscillatory motion.

The indirect method offers several practical advantages. The spectral conversion isolates turbulent fluctuations and suppresses low-frequency hydrodynamic waves that are not part of the turbulent load. It also avoids the spacing constraint of the direct method, which would require much smaller vertical distances (significantly below the present $\Delta x = 0.75\ \mathrm{cm}$) to adequately resolve small-scale gradients. In addition, the indirect formulation avoids the noise amplification that occurs at the highest resolvable wavenumbers and does not depend on the measurement-spacing operator inherent to the direct approach.

The direct method does offer benefits, such as reduced filtering requirements and a more straightforward physical interpretation of the gradient, but under the present experimental geometry these advantages do not outweigh its limitations. In particular, the finite sensor spacing restricts the resolvable high-wavenumber content and may lead to apparent fluctuations at the filter–base interface that exceed those at the filter top, a result that is unlikely to represent physical behaviour.

Overall, neither method provides a perfect representation of the gradient spectrum across all wavenumbers. The indirect method aligns more consistently with the theoretical hypothesis of Thomas (2023) and is therefore regarded as the more reliable approach for this study, provided that the high-k tail is interpreted with caution. The relative agreement between methods in shape in the low- and mid-wavenumber range nonetheless supports the robustness of the measured spectral trends.

6.3. Discrepancies Between Damping Layer Thicknesses

The second test week ($D_f = 6$ cm) exhibits noticeably less damping compared to both the first and third test weeks. This reduction is particularly evident in the damping of the wave-induced sequences, where the intermediate layer thickness shows an almost negligible damping capacity. In contrast, the thinner and thicker layers display a clear decrease in the measured response, even falling below the theoretical damping predicted by Thomas (2023). A similar trend is visible in Figure 5.15, where the damping observed for the 6 cm layer approximates that of the thinnest layer and is even lower under smaller water depths and lower wavenumbers.

This discrepancy is likely related to the positioning of the upper Pressure Sensor Array (PSA) within the rock layer. If the PSA was embedded slightly deeper than intended during the second test week, part of the turbulent pressure fluctuations may have been dissipated before reaching the upper sensors, resulting in an underestimation of the actual pressure gradient across the layer. This interpretation is supported by Figure C.1, where the middle panel (corresponding to the 6 cm layer at 50 cm water depth) shows an earlier decay of spectral energy at higher wavenumbers, indicating a loss of intensity of the short pressure waves. In contrast, both the thinner (4 cm) and thicker (8 cm) layers exhibit a closer agreement with the theoretical hypothesis, maintaining the expected spectral slope over a wider k/U range. The earlier energy decay observed for the 6 cm configuration, even at higher flow velocities, therefore suggests that the sensors may have been positioned too deeply within the filter layer, causing premature damping of the transmitted pressure fluctuations.

The increased variability observed for the thinner filter layer at low wavenumbers can be linked to its greater sensitivity to local surface topography and flow–structure interactions. In a thin layer, even small irregularities, such as a locally protruding stone or a minor gap in the armour, can significantly alter the flow path and allow large-scale, energetic turbulent structures to penetrate more directly toward the base. This effect is amplified when individual stones shift or when a single void forms, as this locally reduces the shielding capacity of the layer and enables the flow to impact the underside of the filter more directly. As a result, the attenuation of the largest turbulent fluctuations becomes less consistent spatially and temporally, explaining the higher scatter observed in the thin-layer spectra. In contrast, thicker layers are less affected by such local geometric irregularities because the additional depth provides redundancy: turbulent structures encounter more pore layers, more tortuous flow paths, and greater opportunities for dissipation, resulting in the stable damping trends measured across the full wavenumber range.

6.4. Dimensions covered

During the experiments, all calculations were performed under the assumption of lateral uniformity, effectively treating the flow as one-dimensional. In reality, the flume and the flow field are two-dimensional, and several lateral effects may introduce deviations from this assumption. These include wall-induced drag, the lateral variation of the turbulent velocity profile, local variability in the rock-layer packing, and the presence of lateral vortices. The drag exerted by the smooth sidewalls is not accounted for, even though it influences both the hydraulic radius and the lateral distribution of the flow velocity. The associated turbulent wall flow, which forms part of this drag, is also ignored. As a result, both the pressure fluctuations and the resulting hydraulic gradients differ between the centreline and the regions closer to the sidewalls. Furthermore, natural variability in rock-layer deposition could lead to measurable differences in the pressure fluctuations recorded by individual sensors. Finally, although the current analysis assumes vortices to move primarily in the vertical direction, they also travel laterally, producing local fluctuations. These lateral variations are expected to diminish when sufficient temporal averaging is applied, but they still contribute to the residual scatter in the measurements.

6.5. Measurement and Layer Construction Uncertainties.

This discrepancy is most likely related to irregularities in the construction of the rock layer and the positioning of the pressure sensors. The determination of the layer thickness is subject to measurement uncertainty. Consequently, the first layer may have been thicker than intended, while the second may have been thinner. Furthermore, the placement of the pressure sensor array (PSA) within the layer can vary slightly between test weeks. As described in subsection 3.4.4, the positioning method is sensitive to error. If, during the second week, the sensors were positioned more deeply within the filter layer, the turbulent pressure fluctuations would have been partially dissipated before reaching the upper sensors, thereby reducing the measured damping, as described in section 6.3.

The combined uncertainty in the physical construction and layer thickness determination is following the procedures of Hauer (2000). This leaves room for uncertainty, and this uncertainty propagates into both the damping and gradient analyses, as even small deviations in layer thickness alter the dimensionless scaling kD_f and h/D_f. The resulting scatter between nominally identical test conditions likely reflects such systematic variations rather than random measurement noise. While each test series was reconstructed with the same compaction procedure, the inherent heterogeneity of the basalt stones (angularity, void ratio, and surface roughness) further contributes to variations in local permeability and turbulence intensity within the layer.

6.6. Flow Intensity and Relative Damping.

Although the damping ratio provides useful insight into how much turbulent energy is dissipated within the filter layer, it remains a *relative* measure. Even strong attenuation, for example, 90% damping, does not guarantee hydraulic safety, as a sufficiently intense flow may still result in an absolute gradient that exceeds the critical value. This distinction becomes particularly important when evaluating cases in which negative or anomalously low damping occurs. For instance, the thin filter layer under high water levels exhibits negative damping, likely caused by local flow irregularities or phase differences between the upper and lower pressure arrays rather than an actual amplification of turbulence. This highlights that the damping ratio should be interpreted as a relative indicator of energy dissipation, not as a direct measure of hydraulic stability.

Figure 5.19 illustrates the dependence of relative damping on water depth and layer thickness, showing that a thicker filter and lower water depth generally lead to stronger attenuation. However, these results do not convey the *absolute* hydraulic load reaching the base. Figure 5.20 clarifies this by expressing the load at the filter-base interface. The left plot demonstrates that, despite similar relative damping behaviour, the absolute load remains highest for the strongest flow intensities. The right plot combines the three key experimental variables-water depth (h), layer thickness (D_f), and mean flow velocity $(\overline{U})$, and shows that higher velocities substantially increase the resulting load.

Together, these figures demonstrate that relative damping alone cannot characterise filter performance: the *flow intensity* fundamentally controls the remaining hydraulic load and therefore the likelihood of exceeding the critical gradient. Absolute load metrics are thus essential when assessing the interaction between turbulence attenuation and hydraulic stability in open filter layers.

6.7. Velocity Estimation and Convection Errors.

Figure 5.4 shows that small offsets between the hypotheses may result from uncertainties in the calculation of the bulk flow velocity, which directly affects the conversion from frequency to wavenumber. Since the wavenumber scaling depends linearly on the flow velocity through the convection assumption, even a slight deviation in U_c can lead to a visible horizontal shift in the spectral alignment. Additional contributions could arise from signal noise or temporal averaging effects, but the overall agreement suggests that the observed differences are primarily due to velocity estimation errors rather than inconsistencies in the underlying theory. Furthermore, drops in water level due to higher velocities could result in higher bulk velocities (which are not accounted for).

The uncertainty in the mean flow velocity $\overline{U}$ directly translates into uncertainty in the convection velocity U_c used for the ω-k conversion. A variation in $\overline{U}$ can induce a similar horizontal shift in k-space, leading to phase misalignment between the theoretical and experimental spectra. Since U_c was not measured directly but inferred from literature correlations (Blake, 1970; Thomas, 2023), this parameter remains one of the principal sources of systematic uncertainty in the indirect method. As described in subsection 4.4.2, the convection velocity can be determined using cross spectral density of two consecutive pressure sensors that are in line with the direction of flow.

6.8. Wave Regime Transitions.

The transition between turbulent and hydrostatic wave regimes is often difficult to precisely indicate, particularly when the water surface begins to exhibit standing wave behaviour at high Froude numbers (approaching 1). Under these conditions, the flow contains both oscillatory and turbulent components, and the resulting pressure fluctuations can overlap in the spectral domain. Consequently, the standing wave motion may be misinterpreted as low-wavenumber turbulence in the Power Spectral Density (PSD) plots. This effect is reflected in Figure 5.19, where the highest velocity conditions (indicated by the bright yellow markers) exhibit noticeably lower damping than the surrounding cases. This reduced damping likely results from the influence of standing waves that penetrate deeper into the flow field than the characteristic turbulent pressure fluctuations, thereby diminishing the apparent attenuation across the filter layer. As mentioned in Figure 5.6, some geometric parameters and there characteristic length can indicate the dominant cause for the fluctuations.

6.9. Discussion Summary

The experimental results generally align with the theoretical framework of Thomas (2023), particularly within the low- and mid-wavenumber ranges where the indirect method reproduces the predicted spectral slopes and damping behaviour. Deviations from the hypothesis emerge mainly at high wavenumbers, where both the physical attenuation capacity of the filter layer and methodological noise amplification limit the accuracy of the measurements. These discrepancies are consistent across layer thicknesses and reflect the finite spectral resolution rather than a structural inconsistency in the theoretical model.

The comparison between direct and indirect gradient spectra reveals that the indirect method is better suited to the present experimental geometry. The direct method is constrained by sensor spacing, the measurement-spacing transfer function, and increased high-k sensitivity, whereas the indirect method more reliably isolates turbulent fluctuations and shows closer agreement with the theoretical predictions.

Layer-thickness effects were reproduced for the thin (4 cm) and thick (8 cm) filters, but not for the intermediate 6 cm layer, whose unexpectedly low damping probably is attributed to construction- and positioning-related uncertainties. Additional variability originates from lateral flow non-uniformity, heterogeneity of the granular material, and deviations in layer thickness, which collectively alter the effective scaling parameters kD_f and h/D_f and propagate into both the damping and loading analyses.

The results further demonstrate that damping is strongly influenced by both layer thickness (D_f) and water depth (h), while the total hydraulic load applied depends on flow intensity. Relative damping alone is therefore insufficient to describe filter performance, and absolute load metrics (e.g. $i'_{2\%}$) are essential for assessing hydraulic stability. In the current-driven experiments, uncertainty in the convection velocity introduces systematic horizontal shifts in the spectral comparison, while standing-wave behaviour at high velocities complicates the distinction between oscillatory and turbulent fluctuations.

Within these bounds of experimental precision, the findings consistently reproduce the predicted spectral trends, confirm the dependence of damping on geometric and hydrodynamic parameters, and further substantiate the applicability of the theoretical model for describing turbulent load transmission through open granular filter layers.

7

Conclusions

This chapter presents the main conclusions of the research. The study was guided by a hypothesis derived from the spectral framework of Thomas (2023), which predicts the spectral shape of turbulent pressure fluctuations above an open filter layer based on geometric parameters (water depth, nominal grain size) and flow-dependent variables (fluid density, mean velocity, shear velocity). By incorporating the layer thickness, Thomas (2023) also provides a corresponding hypothesis for the spectral shape at the filter–base interface. In this theory, the damping of wave-induced pressures (or hydraulic gradients) through the filter layer depends on the ratio between the wavenumber k of the pressure field and the filter thickness D_f, predicting stronger damping for larger values of kD_f. The theory of Thomas (2023) was experimentally tested and expanded under controlled laboratory conditions using both current- and wave-induced flows. This required preparatory testing to optimise the setup, acquisition systems, and boundary conditions, ultimately leading to an experimental procedure. A key improvement was the integration of sealed pressure sensors within the filter layer, enabling reliable, high-resolution measurements of internal pressure fluctuations.

How can instantaneous pressure fluctuations and resulting hydraulic gradients through the filter layer be accurately measured and determined?
The instantaneous pressure fluctuations were measured using high-frequency differential pressure sensors, arranged in two pressure sensor arrays (PSAs): one embedded at the top of the filter layer and one positioned below it. This setup enabled direct comparison of the pressure field across the layer. The sensors were sampled at high frequency to capture both turbulent and wave-induced fluctuations, and the resulting signals were calibrated and filtered to ensure reliability.

The hydraulic gradient was determined using two complementary approaches: a direct and an indirect method.

- **Indirect method:** The pressure Power Spectral Densities (PSDs) were converted to gradient spectra using the wavenumber-dependent formulation of Thomas (2023), applying either the convection hypothesis of Blake (1970) for current tests or the linear wave dispersion relation for wave conditions. This approach isolates the turbulent fluctuations across the relevant spectral range.
- **Direct method:** The instantaneous hydraulic gradient was obtained from the spatial pressure difference between synchronised sensors, providing a time-domain representation of the fluctuating gradient.

Both approaches were supported by advanced filtering techniques, including high-pass, band-stop, coherence, difference, and white-noise filters, to remove drift, bias, low-frequency waves, sensor noise and vibrations of the setup. The methods contributed to understanding the behaviour of pressure and gradient fluctuations within the filter layer. However, given the scale of the experiment and the spectral focus of the analysis, the indirect method was selected as the primary approach for this research.

How do variations in water depth and flow velocity influence the pressure power spectral density due to turbulent pressure fluctuations near the top of the filter?
Variations in water depth and flow velocity primarily influence the magnitude and distribution of the pressure spectrum near the top of the filter. Increasing flow velocity amplifies the spectral energy and extends the range over which the spectra follow the theoretical behaviour, confirming that turbulent pressure fluctuations scale with the mean velocity. In contrast, greater water depths promote the development of larger, more coherent flow structures, which increase the low-wavenumber energy. After scaling with the mean velocity, the spectra collapse onto a nearly self-similar form, demonstrating that velocity scaling governs the spectral shape, consistent with Hofland (2005) and Thomas (2023).

How does the thickness of the filter layer affect the damping of turbulent and wave-induced pressure fluctuations between the top and base of the filter?
An increase in filter thickness results in greater overall damping of pressure fluctuations. For the current-induced flow conditions, the damping followed the theoretical trend proposed by Thomas (2023), based on Blake (1970), which depends on the wavenumber. This agreement is supported quantitatively by a low RMSE of 0.078 between the measured mean damping and the hypothesis, with the strongest correspondence occurring in the higher-wavenumber domain. At lower wavenumbers ($kD_f < 2$), the results exhibited greater variability, particularly for the thinner layer, whereas the thicker layers showed a more coherent and stable damping trend across the full spectral range. Under wave-induced conditions, the damping remained very low, with maximum values below 15%. This is attributed to the much larger wavelengths of the wave-induced pressure field, which result in very small values of kD_f and therefore only limited attenuation through the filter. Overall, the results confirm that filter thickness plays a dominant role in the damping of turbulent fluctuations, while its influence on wave-induced loads is minimal.

What is the influence of the ratio between water depth and filter thickness on the transmission and damping of flow-induced pressure fluctuations within the filter layer?
The ratio between water depth and filter thickness (h/D_f) was found to strongly govern the damping and transmission of pressure fluctuations through the filter layer. Increasing this ratio, due either to larger water depths or a thinner filter layer, reduces the damping efficiency, as larger turbulent structures interact less with the finite filter thickness and smaller-scale vortices can penetrate more deeply into thinner layers. Although higher flow velocities increase the absolute loading, they do not influence the damping efficiency itself. Notably, the experiments covered h/D_f ratios substantially higher than those previously examined in the literature, revealing that this parameter becomes increasingly dominant at large values and critically affects the degree of turbulent transmission. In summary, the damping capacity of the filter layer decreases systematically with increasing h/D_f, highlighting the controlling role of the relative water depth in governing the transmission of turbulent pressure fluctuations.

Main Objective
How can the spectral framework of Thomas (2023) be applied and experimentally validated to describe the transmission and damping of turbulent pressure fluctuations within open granular filter layers?

The spectral framework of Thomas (2023) was successfully applied and shown to provide a consistent description of the load and transmission of turbulent pressure fluctuations through open granular filter layers. The measured pressure and gradient spectra generally reflected the expected wavenumber-dependent behaviour, and the indirect spectral conversion method showed broad consistency with the damping trends, particularly at higher wavenumbers. The experiments demonstrated that the attenuation of turbulent fluctuations is primarily governed by geometric parameters, most notably the ratio between water depth and layer thickness, while flow velocity influences only the loading magnitude. Although deviations remain in parts of the spectrum, the general agreement between theory and measurements shows that the framework provides a sound and physically consistent basis for predicting the transmission of turbulent loads to the filter–base interface. By quantifying the spectral damping and the resulting hydraulic load at the base, this study also strengthens the design foundation for applications where natural geotextiles are used beneath granular filters. The results demonstrate that, when the spectral damping behaviour is incorporated into design, the hydraulic loads acting on a geotextile can be reliably estimated and effectively reduced through the geometry of the overlying filter layer. This supports the safe and sustainable use of natural geotextiles in hydraulic engineering applications.

8

Recommendations

8.1. Test setup improvements

These test-setup improvements would help create a more controlled hydraulic environment, allowing the turbulent pressure fluctuations to be measured with greater purity and reduced interference.

- **Flume width reduction:** Consider decreasing the width of the flume to achieve higher flow velocities. However, this modification would likely have only a limited benefit, as higher velocities reduce the stability of the filter material and therefore require larger rock sizes. Increasing the rock size, in turn, diminishes the comparability between tests and complicates the interpretation of the relationship between water depth and filter thickness, since the latter depends on the nominal rock size under otherwise identical boundary conditions.
- **Larger-scale facility:** To obtain a more comprehensive understanding of the hydraulic behaviour, future experiments could be conducted in a larger flume equipped with pumps of higher discharge capacity. A larger facility would allow for greater variation in water depth and layer thickness, thereby enabling the investigation of a wider range of h/D_f ratios. Higher flume walls would also accommodate thicker filter layers and stronger flow conditions, while the use of larger rocks would reduce the relative interference caused by sensor cables.
- **Cable interference reduction:** The influence of sensor cables on the flow field could be reduced by attaching small, stone-like beads along their length, creating a beaded configuration that mimics the surrounding filter material. This approach would help to minimise local flow disturbances, void ratio discrepancies and improve the representativeness of the measured pressure fluctuations.
- **Improved sensor placement:** During the medium layer experiment, the measured damping behaviour deviated considerably from the thinner and thicker layer, showing a notably different attenuation pattern. To verify and better understand such discrepancies, it is recommended to perform future experiments with an existing rock layer while providing multiple vertical positions for the upper PSA. This configuration would not only allow verification of the observed deviation in the medium layer thickness but also enable characterisation of the vertical distribution of pressure fluctuations within the filter layer.
- **Wave damper:** At the start of the flume, a flow conditioner was installed during the flow tests to reduce large vortices generated by the pump and the geometry of the pipe–flume transition. However, a dedicated wave damper should also be installed to minimise surface waves arising from the blockage created by the flow conditioner, the transition from pipe flow to open-channel flow, and high velocity conditions (approaching critical flow). This would improve the stability of the inflow and reduce low-wavenumber wave energy in the measurements.

8.2. Analytical formulation of the spectral hypothesis

A potential extension of this work would be to express the spectral hypothesis of Thomas (2023) in fully analytical form. Using the two universal peak coordinates of the inner and outer spectra, one could construct approximate analytical representations of the spectral shapes by defining piecewise law expressions that reproduce the correct asymptotic behaviour and peak magnitudes. With such analytical spectra, the pressure-fluctuation variance and corresponding standard deviation could then be obtained directly by integrating the modelled spectrum. This would allow future studies to evaluate the turbulent loading without relying on numerically interpolated universal curves and would enable clearer scaling analyses based solely on the governing flow and roughness variables.

8.3. Convection velocity

To determine the convection velocity, the cross-spectral density (CSD) between two consecutive pressure signals should be computed. Although this analysis has not yet been performed within the scope of this thesis, the CSD allows the determination of the phase angle between the signals, from which the convection velocity can be derived using Equation 2.26. Since the bulk velocity $\overline{U}$ is known, the convection coefficient c_v can then be obtained. According to Blake (1970), the convection coefficient remains approximately constant across experiments and primarily depends on the bed roughness. The coefficient currently applied corresponds to the category of densely packed, large elements, which closely resembles the filter layer configuration used in these experiments.

If the CSD-based approach does not yield consistent results, a sensitivity analysis should be conducted to evaluate the influence of the convection coefficient on the spectral conversion. The expected range of c_v lies between 0.4 and 0.5; variations within this interval are not expected to significantly alter the spectral shape but may affect the quantitative magnitude of the PSD. Such an analysis would provide additional confidence in the robustness of the chosen convection coefficient and its influence on the spectral results.

8.4. Obstacle-Induced Flow Conditions

At the end of each current test, additional experiments were conducted in which an obstacle was placed in the flume to generate vortices in its wake; the tests are elaborated in Appendix F. These experiments were exploratory in nature and have not yet been analysed in detail. Preliminary results based on the pressure power spectral densities (PSDs) indicate that the overall spectral shape closely resembles that of the standard current experiments at comparable flow velocities. This suggests that the presence of the obstacle did not substantially alter the general spectral distribution of the pressure fluctuations.

The initial observations therefore point to only a limited influence of the obstacle on the overall pressure spectra. The flow velocity remained the dominant parameter affecting the PSD shape, whereas the obstacle primarily introduced a narrow spectral spike in the higher-frequency range. This spike shifted toward higher frequencies with increasing flow velocity, consistent with the expected behaviour of turbulence generated in the obstacle's wake. It would be particularly interesting to investigate the damping behaviour of these obstacle-induced pressure fluctuations, since their high-frequency character suggests that they should attenuate almost entirely when transmitted through the filter layer.

For a more comprehensive evaluation, future analyses should omit the coherence-based filtering step, as it may undesirably attenuate the spectral peak associated with the obstacle-induced turbulence. Since the coherent fluctuations caused by the obstacle are spatially correlated across the entire Pressure Sensor Array (PSA), they may be misclassified as external noise by the coherence filter. The white-noise filter may remain applied; however, the NaN cut-off criterion should be removed to ensure that the high-frequency energy spike is retained in the processed signal.

8.5. Wave damping

Currently, the wave damping is determined by calculating the standard deviation of the pressure spectra measured by the upper and lower PSAs and evaluating their ratio to quantify the attenuation. The corresponding peak wavenumber is obtained from the dispersion relation using the peak period, and the damping values are plotted against the wavenumber related to the filter layer thickness, as shown in Figure 5.17.

In contrast, the damping in the current-induced experiments is calculated per wavenumber bin (Δk) by determining the spectral energy ratio between the lower and upper arrays. Applying this wavenumber-based approach to the wave experiments could provide a more detailed characterization of the damping behaviour, particularly within the low-wavenumber range ($k = 0.2$–$5\ \mathrm{rad/m}$). Since wave-induced fluctuations occur at relatively long wavelengths, this alternative method may capture the gradual attenuation across the lower wavenumber domain more effectively than the present zero spectral moment-based approach.

8.6. Damping relation for water depth and layer thickness

This thesis identified a clear empirical trend between the ratio h/D_f and the damping of turbulent pressure fluctuations, as presented in section 5.5. The damping was quantified by comparing the standard deviation of the pressure or gradient fluctuations at the top and base of the filter layer. Although the fitted line in Figure 5.19 captures this trend well, its physical basis has not yet been validated against the theoretical framework.

To confirm whether the observed behaviour follows the predicted damping relation, the variance of the theoretical spectra should be computed for the corresponding test conditions using Parseval's theorem. Applying the same procedure used for the experimental data, deriving damping percentages and plotting them against h/D_f, would allow a direct, like-for-like comparison with the empirical trend.

At present, the analysis is limited by the range of the experiments, which reached h/D_f values slightly above 15, whereas values of 40 or higher are realistic in practical applications. Extending the experimental parameter space and establishing a theoretical comparison are therefore essential next steps for determining whether the fitted trend represents the true physical damping mechanism.

8.7. Premultiplied spectra to determine boundaries

Premultiplied spectra offer a means to more precisely identify the wavenumber range associated with fully turbulent pressure fluctuations. In the current approach, the variance is obtained by integrating the entire area beneath the gradient spectra, after which the standard deviation is used to determine both the damping and the load on the filter-base interface ($i'_{2\%}$). However, this integrated area also contains contributions from hydrodynamic waves and high-wavenumber noise, components that do not represent turbulent loading on the filter base and can therefore bias the estimated load and damping. Although a substantial portion of external interference has been removed through the filtering procedures described in section 4.3, comparing premultiplied spectra before and after filtering can help visualise the magnitude of these corrections and their influence on the spectral energy distribution.

Using premultiplied spectra to delineate the wavenumber range that genuinely reflects turbulent fluctuations would enable future analyses to compute the variance only over this physically meaningful domain. Establishing such boundaries would result in a more controlled and accurate estimate of both the turbulent load and the damping at the filter-base interface.

8.8. Loading

A possible improvement for future studies is the reconstruction procedure proposed by Thomas (2023), in which a fluctuating gradient signal is synthesised directly from the gradient power spectral density. In principle, this method reconstructs a spatial or temporal series by:

1. converting the gradient spectrum $\Phi_{ii}(k)$ into an amplitude spectrum,
2. assigning a random phase to each spectral component,
3. mirroring the spectrum to satisfy the symmetry required for real-valued signals, and
4. performing an inverse Fourier transform to obtain a gradient signal $i'(x)$.

From this reconstructed signal, exceedance levels such as $i'_{2\%}$ can be obtained without assuming a Rayleigh distribution. In the present study, however, the extensive filtering applied during PSD construction, particularly the steps that remove coherent components and suppress phase information, makes a physically reliable inverse FFT difficult to achieve. As a result, a direct reconstruction of $i'(x)$ was not attempted.

Future work could therefore focus on generating PSDs in a manner that preserves phase consistency where possible, or on developing a reconstruction method that is robust to partial phase loss. Such an approach would provide a more physically representative description of turbulent loading, especially under conditions where the gradient distribution deviates from Rayleigh statistics or exhibits non-Gaussian intermittency. In the context of the trends observed here, a reconstructed gradient signal would strengthen the interpretation of how turbulent events penetrate through the filter layer and reach the base.

8.9. Design criteria

The results of this thesis show that the damping of hydraulic loads within granular filter layers depends strongly on the spectral characteristics of the load and on the ratio between water depth and filter thickness (h/D_f). Wave-induced loads, associated with low wavenumbers, exhibit very limited damping, whereas current-induced turbulent fluctuations at higher wavenumbers are significantly attenuated.

In Figure 5.19, a damping trend was fitted using Equation 5.6, based on the measured relationship between h/D_f and the attenuation of turbulent fluctuations. When the validity of this trend is further established, and the contributing variables are better resolved, such a relation may be used as a *reduction factor* in the classical Van de Sande equation (Equation 2.16), allowing filter design to explicitly reflect the influence of water depth and hydraulic load type.

Based on these findings, the following recommendations are made for future filter and geotextile design:

1. **Include load-type dependency in design.** The required filter thickness should distinguish between wave-dominated, current-dominated, and mixed hydraulic loading. Under wave-dominated (low-k) conditions, the limited damping observed in this study may require thicker filters or the addition of an intermediate layer.
2. **Incorporate the water-depth ratio h/D_f as a design parameter.** High h/D_f ratios lead to substantially greater transmission of turbulent pressure fluctuations. Future design criteria should therefore account for this ratio when determining filter thickness or evaluating geotextile loading.
3. **Use transmitted load rather than incident load in geotextile design.** The damping relationships quantified in this thesis can be combined with the natural geotextile design criteria of Akerboom (2024). The transmitted hydraulic gradient or velocity, after accounting for spectral damping, should be used as input to the geotextile design checks, allowing more realistic and load-specific assessments.

Incorporating these elements would lead to more physically consistent and load-responsive design rules, improving the reliability of granular filters and enabling the safe application of natural geotextiles in hydraulic structures.

8.10. Further research

- **Wall effects on turbulence:** Future work should investigate the influence of the flume sidewalls on the spatial distribution of turbulent pressure fluctuations. This includes analysing how proximity to the walls modifies the turbulence intensity and pressure fluctuation profiles compared with the central region of the flume.
- **Vertical gradient behaviour in wave conditions:** The vertical hydraulic gradient under wave-induced conditions could be examined using the direct gradient measurements. The existing dataset obtained in this study is well suited for such an analysis, as each PSA consists of twelve sensors precisely aligned in the vertical direction. This configuration also allows the construction of a lateral pressure profile, enabling assessment of possible wall influences on the measured pressure fluctuations.
- **Multiple open filter layers:** Investigate the effect of using multiple stacked open filter layers, with different stone size distributions, on the overall spectral damping and hydraulic load transmission. Such configurations may offer enhanced attenuation of both low- and high-wavenumber fluctuations. Understanding how turbulent structures interact with successive porous interfaces would help optimise multi-layer systems for stability and material efficiency.
- **Distinction between hydrostatic and turbulent components:** Developing a clear method to distinguish between hydrostatic wave-induced pressures and turbulence-driven pressure fluctuations is essential. Quantifying the relative contribution of each component would improve the interpretation of the total spectral energy and clarify the mechanisms responsible for damping within the layer. Conducting experiments with small-amplitude, high-frequency waves (corresponding to higher wavenumbers) could help identify the transition between wave-induced and turbulence-induced pressure fluctuations.
- **Combined wave-current interactions:** Future studies should combine wave and current forcing to assess how simultaneous oscillatory and advective flows interact. Comparing the resulting pressure and damping spectra with those from purely wave- or current-induced conditions would reveal whether the two mechanisms act independently or exhibit spectral overlap and coupling effects.

Summary of Recommendations

This thesis provides new insight into the spectral transmission and damping of hydraulic loads through granular filter layers. The recommendations focus on improving experimental practice, strengthening analytical methods, refining load reconstruction, and enhancing future design procedures. Improving the experimental setup, through larger-scale facilities, reduced cable interference, improved sensor placement, and better inlet wave conditioning, would enable more controlled hydraulic conditions and expand the range of attainable water depth and filter thickness combinations. Analytical refinements, such as developing a closed-form representation of the spectral hypothesis and determining an experiment-specific convection velocity, would support more accurate and transferable spectral predictions. Further investigation of obstacle-induced turbulence, wave damping behaviour, and the combined influence of water depth and filter thickness is recommended, particularly to validate the fitted damping trend across a broader h/D_f range. For load analysis, reconstructing the hydraulic gradient signal from the gradient spectrum (following Thomas (2023)) would provide a more direct representation of exceedance loads and reduce reliance on distributional assumptions. From a design perspective, the results demonstrate that the damping capacity of granular filters depends strongly on the spectral characteristics of the hydraulic load and on the relative water depth. Wave-induced (low-wavenumber) loads undergo little attenuation, whereas current-induced (high-wavenumber) fluctuations are substantially damped. Future design criteria should therefore incorporate load-type dependency, the ratio h/D_f, and the transmitted rather than incident hydraulic load when assessing geotextile stability. Once validated, the fitted damping relation may also serve as a reduction factor in the classical Van de Sande formulation, enabling a more physically grounded and load-responsive approach to filter design. Collectively, these recommendations aim to enhance both scientific understanding and practical design of granular filters, ultimately supporting more reliable and sustainable applications, including the integration of natural geotextiles, in hydraulic and coastal engineering structures.

References

Aggarwal, A., Alagan Chella, M., Bihs, H., & Myrhaug, D. (2020). Properties of breaking irregular waves over slopes. *Ocean Engineering*, *216*, 108098. https://doi.org/https://doi.org/10.1016/j.oceaneng.2020.108098

Akerboom, D. (2024, August). *Stability of open natural geotextiles: Evaluating the sandtightness of different natural geotextiles by means of physical modelling* [Master's thesis, Delft University of Technology].

Bakker, K., Verheij, H., & De Groot, M. (1994). Design relationship for filters in bed protection. *Journal of Hydraulic engineering*, *120*(9), 1082–1088.

Blake, W. K. (1970). Turbulent boundary-layer wall-pressure fluctuations on smooth and rough walls. *Journal of Fluid Mechanics*, *44*(4), 637–660.

Breugem, W.-P., Boersma, B.-J., & Uittenbogaard, R. E. (2006). The influence of wall permeability on turbulent channel flow. *Journal of Fluid Mechanics*, *562*, 35–72.

Brown, S. A., & Clyde, E. S. (1989). *Design of riprap revetment* (tech. rep.). United States. Federal Highway Administration.

Burcharth, H., & Christensen, C. (1991). On stationary and non-stationary porous flow in coarse granular materials: European community, mast g6-s: Project 1, wave action on and in coastal structures.

Cherry, N. J., Hillier, R., & Latour, M. E. M. P. (1984). Unsteady measurements in a separated and reattaching flow. *Journal of Fluid Mechanics*, *144*, 13–46. https://doi.org/10.1017/S002211208400149X

CIRIA, CUR, & CETMEF. (2007). *The rock manual: The use of rock in hydraulic engineering* (2nd ed.).

Civan, F. (2023). *Reservoir formation damage: Fundamentals, modeling, assessment, and mitigation*. Gulf Professional Publishing.

Dean, R. G., & Dalrymple, R. A. (1991). *Water wave mechanics for engineers and scientists* (Vol. 2). World Scientific.

Deltares. (2023). Handbook of scour and cable protection methods. *JIP HASPRO, Handbook Scour and Cable Protections*.

Griffin, M. S. (2006). *Surface water quality-assurance plan, u.s. geological survey, kentucky water science center, water year 2006* (Open-File Report No. 2006-1273). U.S. Geological Survey. https://doi.org/10.3133/ofr20061273

Hauer, M. (2000, July). *Maak- en meetnauwkeurigheden bij de uitvoering van baggerwerken en steenbestortingen* (Technical Report). Ingenieursbureau Gemeentewerken Rotterdam; Gemeentelijk Havenbedrijf Rotterdam; Vereniging van Waterbouwers in Bagger-, Kust- en Oeverwerken (VBKO). Rotterdam, Nederland, VBKO.

Heineke, D., & Verhagen, H. J. (2009). On the use of the fictitious wave steepness and related surf-similarity parameter in methods that describe the hydraulic and structural response to waves. In *Coastal structures 2007: (in 2 volumes)* (pp. 1057–1066). World Scientific.

Hofland, B. (2005). *Rock & roll: Turbulence-induced damage to granular bed protections* (Publication No. 05-4) [Doctoral dissertation, Delft University of Technology]. https://repository.tudelft.nl/

Honeywell International Inc. (2015, February). *24pc series smt low pressure sensors, uncompensated/unamplified, 1 psi to 15 psi* [Datasheet]. 1985 Douglas Drive North, Golden Valley, MN 55422, USA. https://sensing.honeywell.com

Hudy, L. M., Naguib, A. M., & Humphreys Jr, W. M. (2003). Wall-pressure-array measurements beneath a separating/reattaching flow region. *Physics of Fluids*, *15*(3), 706–717.

Jensen, B., Jacobsen, N. G., & Christensen, E. D. (2014). Investigations on the porous media equations and resistance coefficients for coastal structures. *Coastal Engineering*, *84*, 56–72.

Lee, I., & Sung, H. J. (2001). Characteristics of wall pressure fluctuations in separated and reattaching flows over a backward-facing step: Part i. time-mean statistics and cross-spectral analyses: Part i. time-mean statistics and cross-spectral analyses. *Experiments in Fluids*, *30*(3), 262–272.

Meteostat. (2025). *Weerstation rotterdam airport – meteostat* [Accessed: 2025-05-28]. https : / / meteostat.net/nl/place/nl/delft?s=06344&t=2025-05-21/2025-05-24

Miche, M. (1944). Le pouvoir réfléchissant des ouvrages maritimes exposés à l'action de la houle. *Annales des Ponts et Chaussées*, *121*, 285–318.

Programmable electromagnetic liquid velocity meter, version 1.1. (2019). Deltares. Delft, The Netherlands. https://www.deltares.nl

Ramberg, S. E., & Griffin, O. M. (1987). Laboratory study of steep and breaking deep water waves. *Journal of waterway, port, coastal, and ocean engineering*, *113*(5), 493–506.

Robinson, M., Rice, C., & Kadavy, K. (1998). *Rock riprap design for protection of stream channels near highway facilities* (Technical Report No. FHWA-RD-88-181). United States. Federal Highway Administration. Hydraulics Branch.

Schiereck, G. J., & Verhagen, H. J. (2019). *Introduction to bed, bank and shore protection: Revised edition*. Delft Academic Press.

Senturia, S. D. (2005). *Microsystem design*. Springer Science & Business Media.

Terzaghi, K., & Peck, R. B. (1948). Soil mechanics. *Engineering Practice. John Wiley and Sons, Inc., New York*.

Thomas, Q. (2023, July). *Design method for open geotextiles: The development of a design method for geotextiles under a single granular filter layer based on the principles of open filters* [Master's thesis, Delft University of Technology]. http://repository.tudelft.nl/

Uijttewaal, W., & Booij, R. (2000). Effects of shallowness on the development of free-surface mixing layers. *Physics of fluids*, *12*(2), 392–402.

Van de Sande, S. A. H. (2012). *Stability of open filter structures* [Master's Thesis]. Delft University of Technology.

Van der Meer, J. W., Allsop, N. W. H., Bruce, T., De Rouck, J., Kortenhaus, A., Pullen, T., Schüttrumpf, H., Troch, P., & Zanuttigh, B. (2018). *Manual on wave overtopping of sea defences and related structures: An overtopping manual largely based on european research, but for worldwide application* [http://www.overtopping-manual.com]. EurOtop.

van Nieuwenhuizen, C., & Taal, W. (2021, April). Ems calibration certificate [Calibration performed on 19 April 2021. Reviewed by W. Taal. Internal Deltares document.].

Wave height meter, version 1.1. (2019). Deltares. Delft, The Netherlands. https://www.deltares.nl

Whitaker, S. (2013). *The method of volume averaging* (Vol. 13). Springer Science & Business Media.

Wolters, G., Rudolph, D., Hofland, B., & Verheij, H. (2010). On the behaviour of open filters under wave loading. In *Scour and erosion* (pp. 142–151). American Society of Civil Engineers (ASCE). https://doi.org/10.1061/41147(392)13

Wolters, G., & Van Gent, M. R. A. (2012). Granular open filters on a horizontal bed under wave and current loading. *Proc. Coastal Eng*, *1*(33), 1–10.

Wörman, A. (1989). Riprap protection without filter layers. *Journal of Hydraulic engineering*, *115*(12), 1615–1630.

Young, W. C., Budynas, R. G., Sadegh, A. M., et al. (2002). *Roark's formulas for stress and strain* (Vol. 7). McGraw-hill New York.

Nomenclature

Latin Symbols

Symbol	Description	Unit
a	Wave amplitude	m
A	Cross-sectional area of flow	m^2
C	Chezy coefficient	–
c	Wave celerity ($c = \omega/k$)	m/s
c_f	Friction factor	–
C_D	Drag coefficient	–
C_v	Convection coefficient ($U_c = C_v\overline{U}$)	–
D	Characteristic particle or layer thickness	m
D_f	Filter layer thickness	m
d_{50}	Median particle diameter	m
d_{n50}	Nominal particle diameter	m
Fr	Froude number	–
f	Frequency	Hz
g	Gravitational acceleration	m/s^2
h	Water depth	m
I	Hydraulic slope or energy gradient	–
i	Mean hydraulic gradient	–
i_p	Fluctuating hydraulic gradient	–
k	Wavenumber ($k = 2\pi/\lambda$)	m^{-1}
k_r	Roughness	m
K	Hydraulic conductivity (Darcy permeability)	m/s
K_D	Damping ratio	–
L	Characteristic length scale	m
m_0	Zeroth spectral moment (variance)	m^2
n	Porosity	–
p	Pressure	Pa
p'	Pressure fluctuation	Pa
$\hat{p}$	Sinusoidal pressure amplitude	Pa
Q	Discharge	m^3/s
R	Hydraulic radius	m
Re	Reynolds number	–
Re_p	Particle Reynolds number	–
S_{pp}^{ω}	Pressure PSD in frequency domain	Pa^2/Hz
S_{pp}^{k}	Pressure PSD in wavenumber domain	$Pa^2/(rad{\cdot}m^{-1})$
T	Period	s
t	Time	s
u	Instantaneous velocity	m/s
$\overline{u}$	Time-averaged velocity	m/s
$\overline{\overline{u}}$	Depth- and time-averaged velocity	m/s
u_*	Shear velocity	m/s
u_f	Filter velocity	m/s
U_c	Convection velocity	m/s
w	Flume width	m

Greek Symbols

Symbol	Description	Unit
α	Forchheimer coefficient ($\approx$ 1000)	–
β	Forchheimer coefficient ($\approx$ 1.1)	–
Δ	Relative density $(\rho_s - \rho_w)/\rho_w$	–
Δ...	Known step	–
η	Water surface elevation	m
θ	Phase angle from cross-spectral density	rad
κ	von Kármán constant	–
λ	Wavelength	m
ν	Kinematic viscosity	m^2/s
ρ	Fluid density	kg/m^3
ρ_s	Sediment or stone density	kg/m^3
ρ_w	Water density	kg/m^3
σ	Standard deviation of water surface elevation	m
τ_b	Bed shear stress	Pa
$\Phi_{pp}(f)$	Pressure auto-spectral density	Pa^2/Hz
Φ_{ii}	Hydraulic gradient spectral density	–
ψ	Shields parameter	–
ω	Angular frequency ($2\pi f$)	rad/s

Mathematical Symbols

Symbol	Description	Unit
$\overline{(\cdot)}$	Time-averaging operator	–
$\langle\cdot\rangle$	Ensemble or spatial average	–
$\hat{(\cdot)}$	Amplitude or envelope of a sinusoidal variable	–
$(\cdot)'$	Fluctuating component	–
$\int$	Integral operator	–
$\sum$	Summation operator	–
$\partial/\partial t$	Partial derivative with respect to time	–
∇	Gradient operator	–
$\lvert\cdot\rvert$	Absolute value or magnitude	–
$\tanh(\cdot)$	Hyperbolic tangent function	–
$\mathrm{sech}(\cdot)$	Hyperbolic secant function	–

Abbreviations

Abbreviation	Description
CSD	Cross Spectral Density
CDF	Cumulative Density Function
EMS	Electromagnetic Flow Meter
FFT	Fast Fourier Transform
JONSWAP	Joint North Sea Wave Project (spectral model)
OWC	Oscillating Water Column
PDF	Probability Density Function
PSD	Power Spectral Density
PSA	Pressure Sensor Array
WHM	Wave Height Meter

A

Data

The dataset generated in this thesis has been published on the 4TU.ResearchData platform and is organised into four directories corresponding to the tested filter thicknesses (0, 4, 6, and 8 cm). Each test series consists of three files (A, B, and C). The A-files contain the measurements from the lower Pressure Sensor Array (PSA), the B-files contain the upper PSA data, and the C-files include all auxiliary instrumentation: the discharge meter, the EMS velocity sensor at the PSA location, the WHM wave height meter at the PSA location, as well as the EMS and WHM positioned upstream of the rock layer.

The dataset includes the accompanying `asc_loader.py` script, which is used to merge and preprocess the raw ASC files. When run through the `glue_runs` function, this script consolidates the individual recordings into a single structured dataset, handling the file paths, start and end times, column selection, and column renaming required for further analysis. A Read Me is added explaining how to handle the data, it is based on section 4.2.

The complete dataset is publicly accessible via the following DOI:

10.4121/e8740a5d-2410-49aa-91f2-13b0c1ca4c4e.

File Naming Structure

Each raw data file follows a structured naming convention that encodes the test configuration:

`TestX_DfYcm_TYPE_Z`

where:

- **X** denotes the dataset group:
  - **A**: lower Pressure Sensor Array (12 sensors at the filter–base interface),
  - **B**: upper Pressure Sensor Array (12 sensors embedded in the filter layer),
  - **C**: auxiliary instrumentation (discharge meter, EMS and WHM sensors at and before the filter layer).
- **DfYcm** specifies the filter thickness, e.g. `Df4cm` corresponds to a 4 cm layer.
- **TYPE** identifies the hydraulic loading:
  - `cur`: current-induced flow,
  - `wave`: wave-induced flow.
- **Z** indicates the hydraulic condition:
  - for current tests: the water depth (`30cm`, `49cm`, `67cm`),
  - for wave tests: no additional suffix (a single water depth was used),
  - repeated recordings are marked with `part2`, `part3`, etc.

Examples:

- `TestA_Df4cm_cur_30cm`: lower PSA, 4 cm layer, current test at 30 cm water depth,
- `TestB_Df4cm_cur_49cm`: upper PSA, 4 cm layer, current test at 49 cm water depth,
- `TestC_Df4cm_cur_67cm_part2`: auxiliary sensors, 4 cm layer, second recording of the 67 cm current test,
- `TestA_Df4cm_wave`: lower PSA wave test.

Files with the same suffix belong to the same hydraulic condition and are combined using the `asc_loader.py` script via the `glue_runs` function.

B

Flume Layout

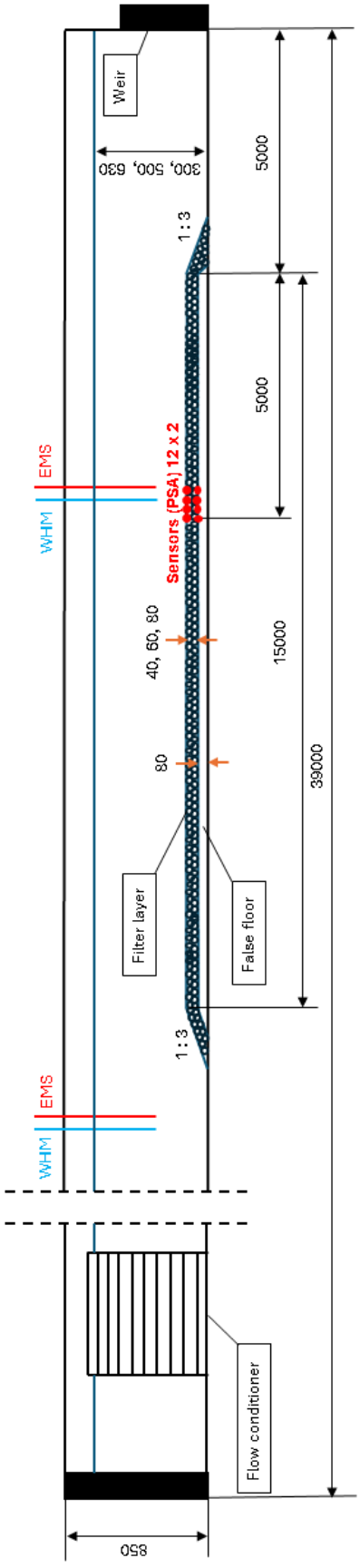

Figure B.1: Technical drawing of the current setup

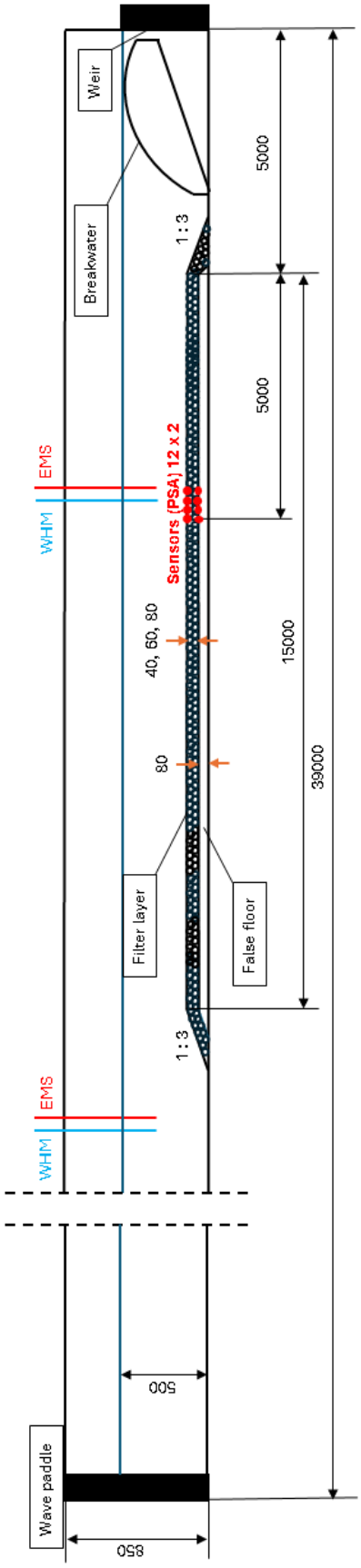

Figure B.2: Technical drawing of the wave setup

C

Plots

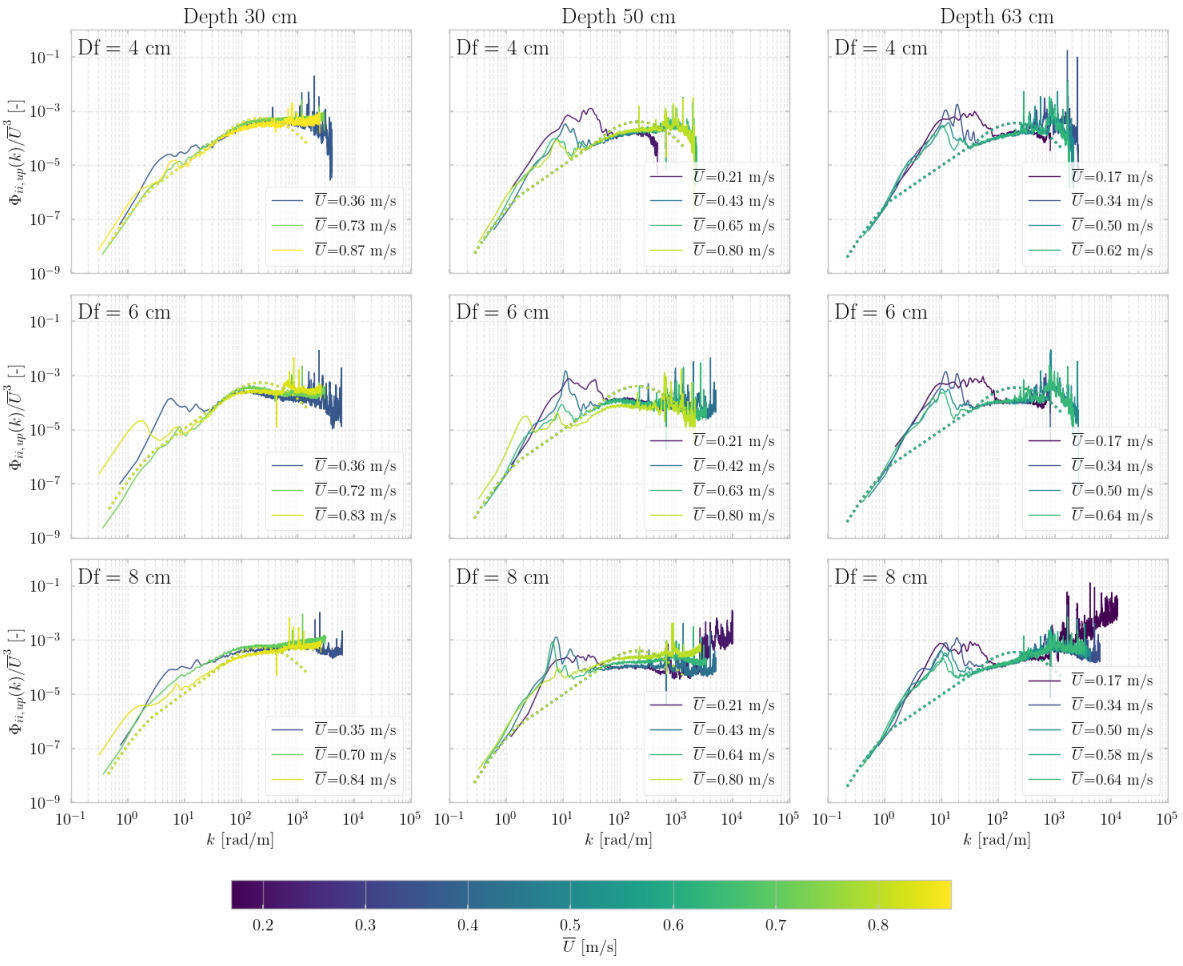

Figure C.1: All upper gradient spectra scaled, columns are the water depth and the rows form the layer thickness

D

Filter Material

In this section the step-by-step determination of the Filter Material is executed, focussing on the filter thickness and Grain size.

D.1. Grain size

In this section, the grain size is determined using multiple Boundary conditions, the Shields equation, Froude number, Maximal discharge capacity, dimensions of the Flume and the Reynolds Number in Porous Media.

Boundary conditions

1. Flume dimensions
   The Flume has a width of 76 cm and a height of 85 cm, for safety purposes, a 5 cm buffer zone between the wall height and the water height is imposed, making the operational maximum height 80 cm.

2. Maximal discharge
   The capacity of the pump creating a water supply to the flume is half a cubic meter of water, however due to safety concerns, the pump cannot exceed 70 percent of its maximum capacity, therefore the operational maximal capacity is 350 liter/s.

$$Q_{max} = \overline{u} \cdot w \cdot h = 0.5 \cdot 70\% = 0.35 \quad [m^3/s] = 350 \quad [l/s] \tag{D.1}$$

   Together with the Flume dimensions the boundaries for the flow velocity and water depth can be derived from Equation D.1, considering the fact that the width will not change.

3. Shields equation
   The Shields parameter and equation are used to determine the stability of granular elements, this value cannot exceed the rule : $\psi < 0.03$. The shields equation holds the next boundary condition for the grain size to ensure no movement in the filter layer.

$$\psi = \frac{\tau}{(\rho_s - \rho_w) g d_{50}} = \frac{u_*^2}{\Delta g d_{50}} \Rightarrow d_{50} = \frac{u_*^2}{\psi g \Delta} \tag{D.2}$$

   First the Hydraulic Radius $[R]$ is determined with Equation D.3, which is specific for a rectangular open channel.

$$R = \frac{wh}{w + 2h} \tag{D.3}$$

Next the shear velocity $[u_*]$ can be obtained with the Chezy equation depicted in Equation D.4 and making a first assumption of the grain size, knowing that the roughness is approximately twice the nominal grain size.

$$C \approx 18 \log\left(\frac{12R}{k_r}\right) \qquad ; \qquad k_r = 2 * d_{n50} \tag{D.4}$$

$$u_* = \sqrt{\tau_b/\rho_w} = \overline{u}\frac{\sqrt{g}}{C} \tag{D.5}$$

To go from the required median grain size d_{50} to the nominal grain size d_{n50}, Equation D.6 is needed:

$$d_{n50} = 0.84 \cdot d_{50} \tag{D.6}$$

By iterating the nominal diameter of the filter material, eventually the value should converge towards the shields parameter and the right d_{n50} will be obtained.

In the experiments the only fluid that is used is water, therefore the density of the fluid $[\rho]$ in Equation D.5 is noted as ρ_w.

4. Froude Number
The Froude number is used to consider the ratio between the external flow (denominator) and flow inertia (numerator), expressed in Equation D.7. The Froude number indicates the behaviour of the flow, for the experiments subcritical flow is required and therefore the Froude number should be below 1, and prefferably further below, to avoid critical flow.

$$\text{For subcritical flow:} \qquad Fr = \frac{u}{\sqrt{gh}} < [0.75 - 1] \tag{D.7}$$

5. Forchheimer and Reynolds Number in Porous media
The Forchheimer equation is used to consider the posibility of the inertial flow effects due to the narrowing of pores by formation damage in the momentum balance, according to Civan, 2023.

$$\frac{1}{\rho g}\frac{\partial p}{\partial x} = i = a u_f + b u_f |u_f| + c\frac{\partial u_f}{\partial t} \tag{D.8}$$

During the experiments is stationary flow assumed, therefore the term $\frac{\partial u_f}{\partial t}$ can be omitted, and the following equation can be derived:

$$i = a u_f + b u_f |u_f| \tag{D.9}$$

The empirical parameters a and b can be calculated as stated in Equation 2.7, "the dimensionless coefficients α and β (that depend on, among other things, the grading and the shape of the grains) have to be determined experimentally. Without any further information, $\alpha \approx 1000$ and $\beta \approx 1.1$ can be used as a first estimate (with possible values twice as low or twice as high)."(Schiereck and Verhagen, 2019, p. 106).

$$\text{with:} \quad a = \alpha\left(\frac{(1-n)^2}{n^3}\right)\frac{\nu}{g\, d_{(n)50}^2}, \qquad b = \beta\left(\frac{1-n}{n^3}\right)\frac{1}{g\, d_{(n)50}} \tag{D.10}$$

The filter velocity shown in Equation 2.6 can be derived when equalizing the Forchheimer gradient to the gradient through average velocity. Equation D.11 shows the calculation for the gradient obtained with the average velocity, Hydraulic Radius and Chezy coefficient.

$$i = \frac{\overline{u}^2}{C^2 R} \tag{D.11}$$

The filter velocity can now be derived using Equation D.9 and the quadratic formula, next the last boundary condition can be implemented:

$$Re_p = \frac{u_f D_{n50}}{n\nu} \tag{D.12}$$

According to Burcharth and Christensen, 1991 the value of 300 for the porous Reynolds number dictates the lower boundary of the turbulent flow regime, ”the fully turbulent flow regime should be somewhat larger, i.e. $Re_c \simeq 600$–1000”.

Table D.1 shows the 5 boundary equations that remain.

Table D.1: Boundary conditions to determine the Grain size

Boundary Condition	Consequential values
1.	$w_{max} = 0.76 \quad [m], \quad h < 0.85 \quad [m]$
2.	$Q_{max} < 0.35 \quad [m^3/s]$
3.	$\psi < 0.03$
4.	$Fr < 0.75$
5.	$Re_p > 300$

Input parameters

Table D.2 describes the input parameters used to obtain the design space.

Table D.2: Input parameters to construct the design space nominal grain size

Symbol	Parameter	Value	Unit
g	Gravitational acceleration	9.81	m/s^2
ρ_w	Density of water	1000	kg/m^3
ρ_s	Density of basalt	2960	kg/m^3
Δ	Relative density	1.96	$[-]$
ν	Kinematic viscosity of water	$1.002 \cdot 10^{-6}$	m^2/s
ψ	Shields parameter	0.03	$[-]$
n	Porosity of filter (Van de Sande, 2012)	0.38	$[-]$

Table D.3 shows the independent variables and the ranges that have been used to obtain the nominal grain size, the filter layer thickness has been omitted, for it has no contribution to the nominal grain size, as it is not used in section D.1.

Table D.3: Ranges used for the independent variables in the parameter study

Symbol	Variable	Range	Unit
h	Water column height	0.1 to 0.8	m
d_{n50}	Median grain diameter	0.01 to 0.1	m
u	Flow velocity	0.1 to 1.5	m/s

Design Space

The design space for the filter velocity and the grain size against the Reynolds Number in porous media is shown in Figure D.1. The red dashed line shows the boundary of the Reynolds number threshold.

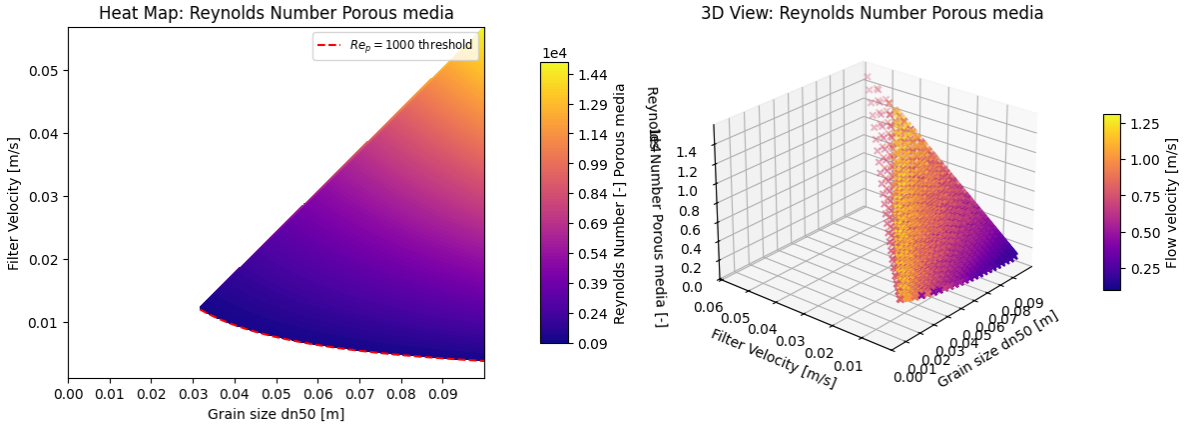

Figure D.1: The Reynolds Number in Porous Media for grainsizes between 0 and 0.1 meters

The design space for the three variables is shown in Figure D.2, on the left are the valid combinations given, on the right are three boundary condition planes shown, for boundary conditions 2, 4 and 5. The shields parameter, maximum width and height are omitted, considering that the maximum width is implemented in the constraint for the maximum discharge and the height is displayed by not surpassing this limit in the range for the water column height. The shields parameter is merely a control value, however is not relevant in this visualisation.

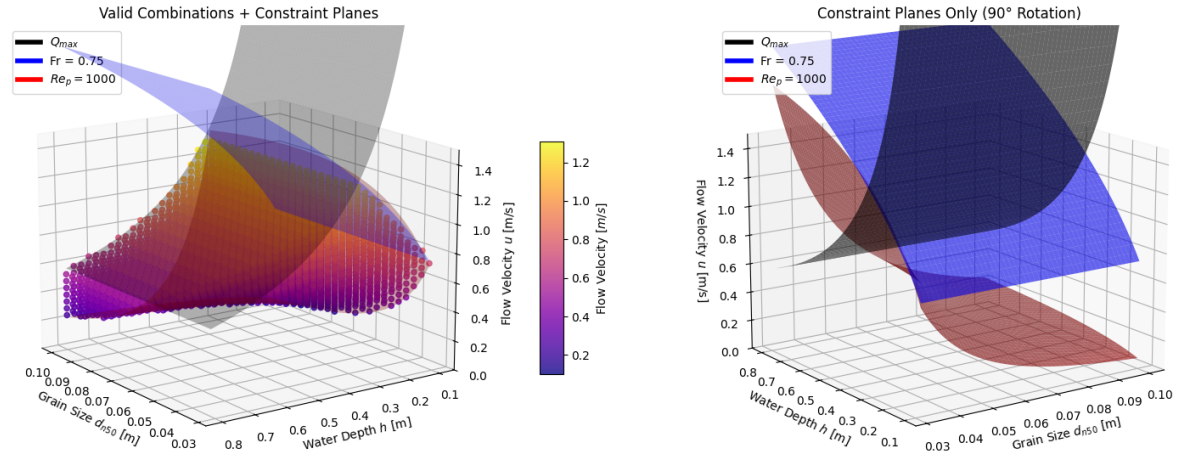

Figure D.2: Design space for three variables with the boundary planes

As seen in Figure D.2 and especially Figure D.1 the nominal grain size is at least higher than 3 cm to satisfy the Reynolds Number in Porous media constraint.

E

Wave conditions

This chapter focuses on the wave conditions that will be exerted during testing, these conditions are based on the literature, theoretical background and the capacity of the wave generator explained in Sections E.1, E.2, & E.3. The wave conditions will also be physically tested by controlled trial and error in the preperation week of the tests, as explained in section E.4.

E.1. Specifications Wave Generator

The experimental program is conducted within the operating range of the wave generator installed in the Sediment Flume. This device is capable of producing regular wave conditions with significant wave heights and peak wave periods ranging from:

$$H_s = 0.01 - 0.15 \quad [m] \qquad \text{and} \qquad T_p = 0.7 - 3.0 \quad [s]$$

These boundaries are suitable for the intended testing conditions, provided that wave breaking is avoided. Wave breaking may occur due to excessive steepness or depth-induced shoaling, particularly as the waves propagate over the elevated false bottom and filter layer. Additionally, it is crucial that wave crests remain below the flume walls to avoid overtopping on the sides. Establishing these theoretical limits is essential to characterise the operational space for safe and controlled testing.

E.2. Shoaling

Shoaling refers to the transformation of wave characteristics due to decreasing water depth. As waves encounter the elevation change introduced by the false bottom and filter layer, their heights increase and group velocities decrease. This energy concentration can lead to increased wave steepness and, under certain conditions, wave breaking. Since this phenomenon plays a significant role in determining the effective wave steepness, it must be considered when assessing wave stability limits, as further elaborated in section E.3.

E.3. Wave Steepness

The wave steepness for deep water waves is described by Heineke and Verhagen, 2009 as shown in Equation E.1. In deep water there is no dependence on the depth. The boundary for breaking waves in deep water is 0.11 according to Ramberg and Griffin, 1987 and 0.14 for individual waves according to Heineke and Verhagen, 2009, which is derived from the formula of Miche, 1944, which also states that the wave steepness has a normal range of 0.03 to 0.04. The spectral wave steepness is given on the right side of Equation E.1, according to Aggarwal et al., 2020, where the H_{s0} and T_p are the offshore significant wave height and the peak period respectively.

$$s_0 = \frac{H}{L_0} = \frac{2\pi H}{gT^2} \quad ; \quad s = \frac{2\pi H_{s0}}{gT_p^2} \tag{E.1}$$

Equation E.2 also includes the depth dependence, and can be applied to intermediate and shallow water conditions.

$$\left(\frac{H}{L}\right)_{max} = 0.142 \cdot \tanh\left(\frac{2\pi h}{L}\right) \tag{E.2}$$

The wave conditions used in the research of Wolters et al., 2010, used a steepness range of 0.004 to 0.027, here the depth of the test setup was 0.4 meters. When using wave loading in combination with current flow, the research of Wolters and Van Gent, 2012 can be consulted.

Table E.1: Wave Characteristics for Test Conditions

H_0 **[m]**	$H_s h$ **[m]**	h **[m]**	T_p **[s]**	s_0 **[-]**	s_0 **[%]**
0.05	0.052	0.6	1.5	0.015	1.5
0.10	0.104	0.6	1.0	0.066	6.6
0.10	0.104	0.6	2.0	0.017	1.7
0.10	0.104	0.6	1.5	0.028	2.8
0.15	0.155	0.6	1.5	0.044	4.4

Some of the values exceed the steepness of 4%, to test the theory in reality the values that exceed this boundary have to be tested iteratively. Considering a regular wave field will be generated, the waves should break in extremer events than the boundary of 4 % that is given.

E.4. Wave Test Procedure

The test procedure will begin with the most extreme wave conditions to assess the test ranges and adjust according to what is possible. These conditions will be tested before the filter layer is installed, the filter layer will cause a larger difference in depth and causes the waves to increase, the height in Table E.1 assumes the largest filter thickness, which causes an wave height increase of 3%, as a consequence of shoaling.

E.5. Breakwater

The breakwater at the end of the flume should be designed in such a way that there is not a lot of spillage over the sides of the flume.

The crest height of the flume is calculated using Equation E.3, given by Van der Meer et al., 2018.

$$\frac{q}{\sqrt{gH_{m0}^3}} = 0.09 \exp\left[\left(-1.5 \frac{R_c}{H_{m0}\gamma_f\gamma_\beta}\right)^{1.3}\right] \tag{E.3}$$

By assuming an allowed discharge of 1 l/s/m.

F

Obstacle

The obstacle test consisted of an obstacle described in subsection 3.1.4, these caused interference in the flow. As shown in Table F.1, the obstacle was placed either 2 meters or 1 meter in front of the pressure sensor array. The columns were put in place using two 12 centimetre screws on each side, the holes were pre-drilled, ensuring the same placement of the obstacle every test. To prevent the obstacle from experiencing a torsional deflecting caused by the force of the water flow, steel beams were placed on top of the obstacle, these ensured stiffness of the obstacle. The steal beams were mounted using glue clamps as visible in Figure F.1.

Table F.1: Obstacle tests summary by week: U-bulk per distance for each water depth at the array.

Week (dates)	**Water depth [m]**	$\overline{U}$ **at 1 m [m/s]**	$\overline{U}$ **at 2 m [m/s]**
	0.30	0.70, 0.83	0.70, 0.83
Week 3 (28–31 Jul)	0.49	0.43, 0.74	0.43, 0.74
	0.63	0.25, 0.60	0.26, 0.58
	0.29	0.54, 0.82	0.54, 0.82
Week 4 (4–6 Aug)	0.50	0.42, 0.74	0.42, 0.74
	0.63	0.34, 0.59	0.34, 0.59
	0.30	0.53, 0.82	0.53, 0.81
Week 5 (11–12 Aug)	0.50	0.43, 0.74	0.43, 0.72
	0.63	0.42, 0.58	0.58

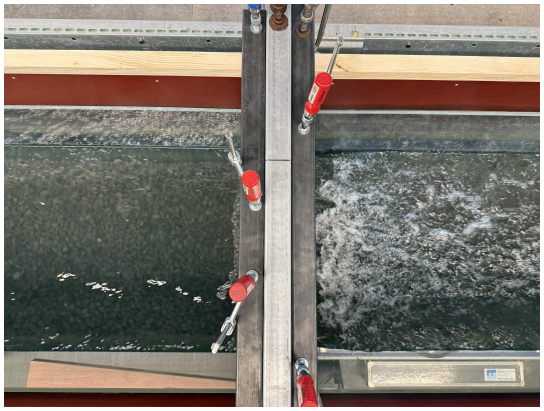

Figure F.1: Top view obstacle during testing

G

Pressure Sensor

G.1. Sealed characteristics through theoretical approximation

This section determines the characteristics of the sensor diaphragm, to determine the resistance of the air that remains in the opposite chamber of the water chamber. For the resistance of the air is the ideal gas law used and mechanics of plate structures. The pressure sensors that are used during the laboratory experiments are the Honeywell 24PC or 26PC series, these have the same internal dimensions.

Plate

The silicon square plate (chip) properties and assumptions are shown in Table G.1, furthermore, the plate is assumed to be a simply supported plate at all edges, this means that there is no deflection at the edges of the plate. In reality there is rotation resistance as well, however at this scale that is negligible and will give a more conservative estimate.

Table G.1: Physical parameters and computed values for a simply supported plate

Variable	Symbol	Value	Unit
Density of silicon	$\rho_{silicon}$	2330	kg/m^3
Density of water	ρ_w	1000	kg/m^3
Deflection coefficient	α	0.0444	–
Stress coefficient	β	0.3762	–
Poisson's ratio	ν	0.28	–
Young's modulus	E	130	GPa
Plate length	L	1.7	mm
Overpressure	p_{max}	138	kPa
Maximum shock pressure	$p_{max,shock}$	13.8	MPa
Plate area	A	2.89	mm^2
Yield strength	σ_0	3.5	GPa

The variable that is required to determine whether the volume of air will influence the measurements is the maximum tolerable deflection, which depends on the thickness of the plate. The plate thickness can be obtained by rewriting the plate deflection equation, with the bending stiffness . The pressure is the maximum overpressure of the used sensors for the experiments (Honeywell International Inc., 2015) which is 20 psi or 137 kPa. The manual provided by Honeywell International Inc., 2015, states that the maximum shock a pressure sensor can endure is an acceleration of 100G during 11 seconds.

The shock factor of 100 is multiplied with the maximum overpressure that the chip can withstand. It is assumed that this pressure is homogeneously distributed over the area.

For a uniformly loaded rectangular plate all edges are supported with hinges, the following formulas estimate the stress and central deflection, according to Young et al., 2002:

1. Pressure due to a shock wave

$$p_{shock} = \frac{F}{A} = \frac{m \cdot a}{A} = \frac{100 \cdot \rho_w \cdot V \cdot g}{A} = 100 \cdot \rho_w \cdot g \cdot h_{max} \tag{G.1}$$

2. Bending stress in the middle of the plate

$$\sigma_0 = \frac{\beta_2 q L^2}{h^2} \tag{G.2}$$

3. Max deflection:

$$w_{centre} = \frac{\alpha q L^4}{E h^3} \tag{G.3}$$

4. Combined formulas:

$$h = \sqrt{\frac{12(1-\nu^2) a \rho_{silicon} L^4 \alpha}{E w_{max}}} \tag{G.4}$$

The height of the chip necessary to withstand the pressure of with an acceleration of 100G is the $4.28\text{e}{-9}$ meters or 4.28 nm.

$$\sigma_0 = \frac{1}{\pi^2}(1-\nu^2)\left(\frac{L}{h}\right)^2 p_{max,shock} \quad \Rightarrow \quad h = L \cdot \sqrt{\frac{1}{\pi^2(1-\nu^2)} \cdot \frac{p_{max,shock}}{\sigma_x}} \tag{G.5}$$

The approximate model, made by Senturia, 2005 and shown in Equation G.5 gives a more realistic approach to determine the thickness of the plate, which is determined to be $32.6\text{e}{-6}$ meters or **32.6 microns**, which is a realistic thickness for the diaphragm, according to Senturia, 2005 most chips have a thickness of 50 microns or less.

Air Resistance

The resistance of the air is determined in this section, accounting for the external factors that may influence the resistance. The chamber that is filled with air is a cylinder combined with a box. The walls of the chamber are assumed to be infinitely stiff, ensuring that the only reduction of volume is created by the bending of the plate. To simplify the shape of deflection a sinusoidal shape in both x and y direction is assumed, as demonstrated in Equation G.6.

$$w(x,y) = -\frac{\Delta h}{2}\left[\sin^2\left(\frac{\pi x}{L}\right) + \sin^2\left(\frac{\pi y}{L}\right)\right] \tag{G.6}$$

By assuming this deflection, the reduction of the volume will be half the maximum deflection multiplied with the area, as shown in Equation G.7, as consequence of the deformation shape of the chip.

$$\Delta V = \frac{\Delta h \cdot A}{2} \tag{G.7}$$

Step 1: Geometry of the Chamber
The chamber consists of:

- A cylinder with height $h_c = 2\,\text{mm}$ and radius $r = 0.75\,\text{mm}$
- A square box with base $1.7\,\text{mm} \times 1.7\,\text{mm}$ and height $1\,\text{mm}$

Only the top of the rectangular box (diaphragm) compresses. The other walls of the chamber are assumed to be infinitely stiff. The vertical deflection is derived from the deflection of the centre of the plate, where the deflection is maximum, to calculate this deflection, Equation G.3 is used:

$$\Delta h = 22.5\,\mu m$$

The pressure used to obtain this deflection is the maximum pressure that can be measured during testing, which is 35 kPa.

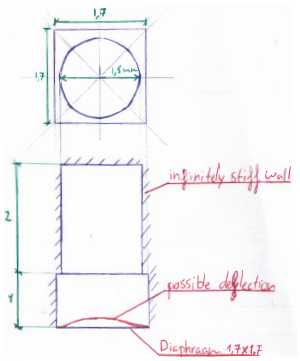

Figure G.1: Detail drawing of chamber (dimensions in mm)

Step 2: Initial Volume of the Chamber
The initial volume of the chamber is calculated as follows:

$$V_0 = V_{\text{cyl}} + V_{\text{box, 0}} = \pi r^2 h_c = \pi(0.75)^2 \cdot 2 + 1.7 \cdot 1.7 \cdot 1 \approx 6.424\,\text{mm}^3$$

Step 3: Volume After Compression
The Volume of the chamber changes after the deflection of the silicon plate, resulting in reduction in the volume. The plate is simply supported, therefore there is no homogeneous translation of plate, the displacement of the plate agrees with the boundary conditions at the edges of the plate, resulting in a non-linear shape.

$$V_{\text{box,new}} = V_{\text{box, 0}} - \Delta V \approx 2.841\,\text{mm}^3$$
$$V_1 = V_{\text{cyl}} + V_{\text{box,new}} = 3.534 + 2.841 = 6.375\,\text{mm}^3$$

Step 4: Pressure Increase
The pressure increase is calculated using the Ideal Gas Law, with ideal gas constant $[R]$, assuming that the temperature $[T]$, and amount of gas $[n]$ do not change.

$$nRT = P_0 V_0 = P_1 V_1 \Rightarrow P_1 = P_0 \cdot \frac{V_0}{V_1} \approx 101325.5\,\text{Pa}$$
$$\Delta P = P_1 - P_0 = 101325.5 - 101325 = 0.5\,\text{Pa}$$

Step 5: Relative compression
The relative compression is calculated using the maximum pressure and the pressure increase.

$$p_{relative} = \frac{\Delta P}{p_{max}} < 0.0000147 = \mathbf{0.00147}\%$$

Conclusion
This pressure difference is minimal and will not influence the measurements obtained with the pressure sensors. During the installation of the sensors, the local air pressure will be measured, to account for possible pressure differences, considering that these are more significant than the resistance of the compressed air.

G.2. Temperature Tests

This section describes the temperature tests conducted on the sealed and unsealed pressure sensors, to determine the influence of variations in water temperature.

Objective

To evaluate the effect of water temperature on the output of pressure sensors by immersing them in multiple water baths with gradually increasing temperatures. The goal is to determine whether internal air cavity pressure variation (due to heating) causes detectable output shifts.

Hypothesis

Assuming that the volume of the chamber does not change over time, and the initial pressure in the chamber was 1 ATM (101,325 Pa), steps of 0.25 psi are taken to determine the estimated temperature steps that are needed in the test. Assuming that the environmental room temperature is 20°C.

The values displayed in Table G.2 are based on the ideal gas law:

$$PV = nRT \Rightarrow \Delta P \propto \Delta T \quad \text{(at constant volume)}$$

Table G.2: Measured pressure as a function of water temperature

Temperature $[°C]$	**Pressure** $[Pa]$	**Pressure relative to 1 ATM** $[psi]$	**Voltage** $[V]$
30	97878	-0.5	-5
25	99601	-0.25	-2.5
20	101325	0	0
15	103049	0.25	2.5
10	104772	0.5	5

The influence of the temperature on the pressure is visualised in Figure G.2, according to the ideal gas law.

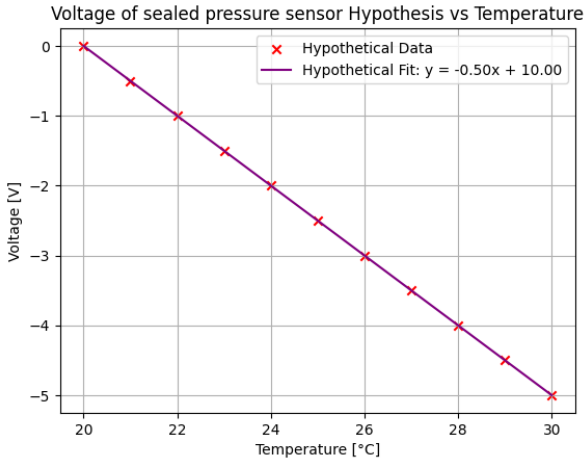

Figure G.2: Hypothesis plotted from 20 to 30 °C

Test Setup Overview

- 1 pressure sensor with a sealed reference port (trapped air cavity)
- 1 water bath with the ability to gradually increase temperature
- Depth of immersion kept constant
- Temperature measured in water bath
- Pressure sensor range: **±0.5 psi**

Materials

Item	Description
Pressure sensor	Relative sensor with sealed reference port
Temperature probe	Digital thermometer or thermocouple
Water bath	A water basin used to maintain a steady temperature for a prolonged time
Test tube rack	Used to keep the sensors in place (correct depth)
DAQ / multimeter	To log sensor output in real time
Ruler or guide rod	To ensure consistent immersion depth
Insulation materials	Optional: to reduce heat loss

Test Procedure

1. Fill the water bath with water of room temperature.
2. Measure and record the actual temperature, to confirm the reference measurement.
3. Submerge the pressure sensor to a fixed depth (e.g., 5 cm) in the water bath.
4. Wait until pressure readings stabilize. Record output and corresponding temperature.
5. Increase the temperature of the water bath and repeat the measurement after stabilisation.
6. Continue the process for all five temperature levels.
7. Optionally, repeat test in reverse order (cooling) to detect hysteresis effects.

Expected Results

- An increase in measured pressure of 0.25 psi is expected as temperature increases with $5^{\circ}\mathrm{C}$, caused by thermal expansion of trapped air.
- The change should remain within the ±0.5 psi operating range.
- The relationship may approximate linearity if the volume remains constant.

Data Recording Table

Table G.3 contains the measurements obtained during the test of the pressure sensors.

Table G.3: Measurements of temperature, depth, and sensor voltages in sealed and unsealed conditions.

Meas.	Temp ($^{\circ}\mathrm{C}$)	Depth (cm)	Depth (V)	Sealed (V)	Unsealed (V)
1	20.15	7.0	0.00	+0.01	+0.00
2	23.18	7.0	0.00	-1.59	+0.01
3	24.27	7.0	0.00	-2.25	-0.02
4	26.65	7.0	0.00	-3.70	-0.04
5	28.43	6.8	-0.03	-4.77	-0.06
6	26.79	7.3	0.04	-3.88	+0.00
7	24.30	8.7	0.24	-2.38	+0.42
8	22.10	9.0	0.28	-0.90	+0.39
9	19.98	8.5	0.21	+0.60	+0.42

The Depth expressed in Volts is calculated by subtracting the baseline measurement (7 cm) and converting it from centimetres head, to psi, to volts. The conversion is as follows: 0.01422 psi is 1 cm and 1 volts is 0.1 psi, therefore 1 cm equals 0.1422 volts.

Data Figures

Figure G.3 contains the raw data obtained during the tests, with the sealed pressure sensor (blue), the unsealed pressure sensor (green) and the depth influence (black). The depth influence has been calculated by subtracting the first value (baseline measurement) and converting the height in water head to psi and finally converting it to Volts.

Figure G.4 shows the linear regression of three situations, the first linearity is the sealed pressure sensor output (blue), this describes the progression of the test, taking no external factors into account. The second is the difference in output between the sealed pressure sensor and the unsealed pressure sensor (red), the unsealed sensor served as a reference sensor. The last linear regression is the measurements subtracted by the depth influence on the pressure, which should leave the temperature as sole influence on the pressure decrease.

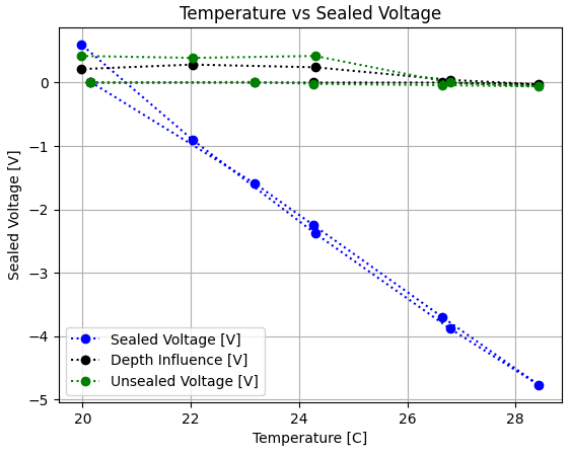

Figure G.3: Raw Pressure Data in voltage

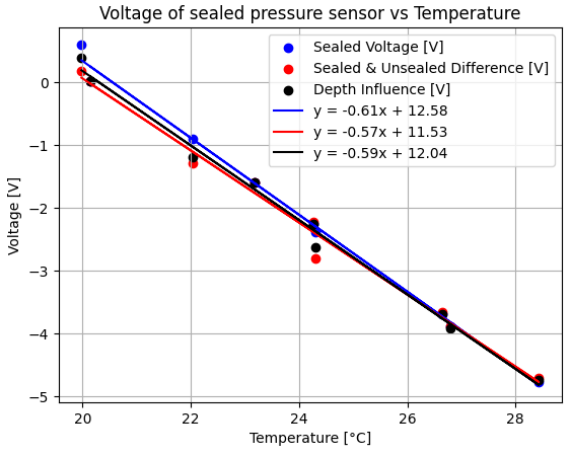

Figure G.4: Linear Regression Fit

Finally Figure G.5 displays the hypothesised progression of the temperature influence according to the ideal gas law and the measured influence.

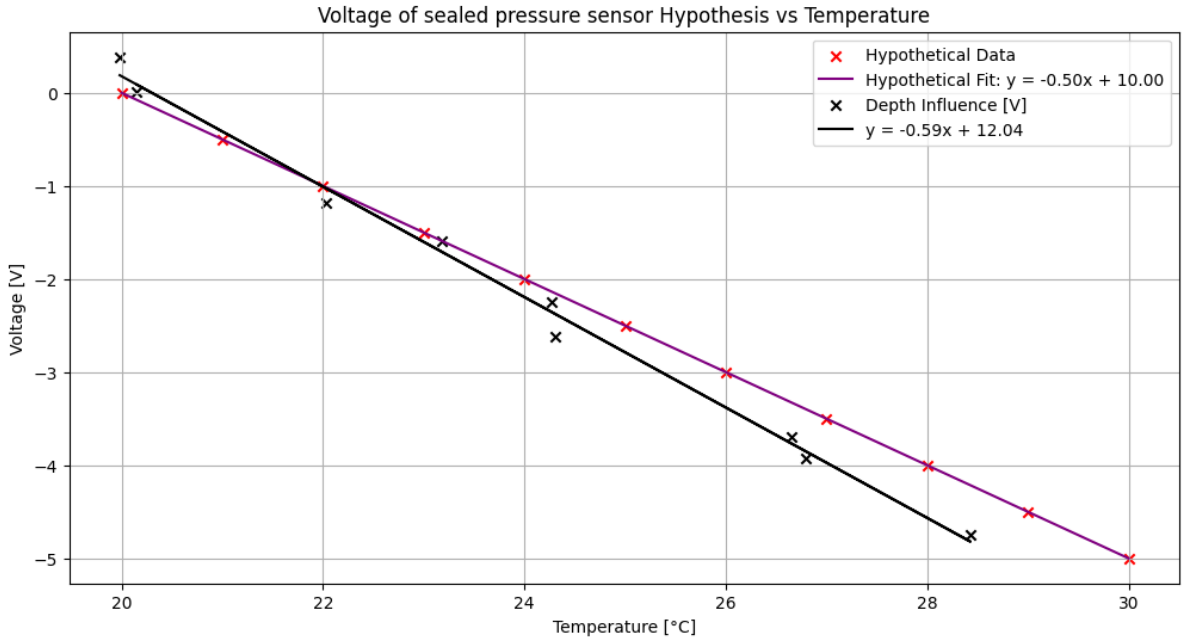

Figure G.5: Hypothesis of Temperature influence vs measured Temperature influence

Remarks

The first temperature measurement has been done with both an analogue thermometer and a digital thermometer, measured at **19**$^{\circ}\mathrm{C}$. Measurement frequency is 2 Hz. To ensure that the first measurement is stable, the nulmeasurement has a duration of 5 minutes.

The water in the cooldown bucket has a temperature of 13 $^{\circ}\mathrm{C}$. Small amounts of water are added to decrease the temperature in the basin (measurements 6 and 7). Afterwards the temperature was decreased using icepacks (after measurement 7)

When the water was added to reduce the temperature in the water bath, the test tube rack began to float, which may have relocated the reference sensor. This is the probable cause for the sudden increase in voltage for the Unsealed line (green) after measurement 6, visible in Figure G.3.Additionally, the increased water depth, as a consequence of extra cooling water, has increased the pressure in the sensors.

Conclusion

As stated in the hypothesis a pressure drift is shown due to thermal expansion, with a near-linear relationship. The expected data is very close to the test-obtained data, however the measured data has a steeper incline than predicted in the hypothesis.

Recommendations

When using pressure sensors with sealed reference port, it is vital to know the surrounding temperature to account for increases or decreases in pressure as a consequence of thermal expansion. When conducting experiments using these sealed pressure sensors, a thermometer needs to be closely installed and a unsealed reference sensor needs to be placed.

Discussion

The sealed pressure sensor is enclosed within a polyester casing filled with silicone sealant, leaving a small internal air pocket. Due to the insulating properties of the sealant and the small volume of the air chamber, the internal air temperature responds slowly to changes in the surrounding water temperature. As a result, it is difficult to determine the exact internal temperature of the sealed cavity during the experiment. This lag in thermal equilibration between the internal and external environments is a likely explanation for the observed discrepancy in the steepness of the measured pressure trend compared to the theoretical prediction. To quantify the thermal response time of the sealed chamber, a long-duration experiment could be conducted. Equilibrium between internal and external temperatures may be assumed when the rate of temperature change over time approaches zero.

G.3. Long-term Sensor Test

This section describes a long-term test conducted to assess the behaviour of pressure sensors with different reference configurations under stable and varying environmental conditions.

Introduction

Minimizing measurement disturbance caused by the presence of sensors is crucial in experimental research. To reduce flow interference and obtain accurate results, it is important to use sensors that are as small and unobtrusive as possible. In the context of detecting pressure fluctuations within an open filter layer, capturing small-scale variations requires sensors with low noise levels and high spatial resolution. Smaller sensors not only improve signal clarity but also allow for reduced spacing between measurement points, enabling the detection of short pressure waves. Moreover, integrating sensors directly into the filter material, such as embedding them in or designing them to resemble rocks, helps replicate the natural turbulence of the system, resulting in more representative and undisturbed measurements.

Using sealed pressure sensors further contributes to reducing the physical footprint of the instrumentation, as it eliminates the need for external reference tubes. These tubes can be relatively large and obstruct the flow, while also complicating the natural arrangement of filter rocks. By omitting them, sealed sensors offer the potential for more organic and realistic test configurations. However, sealing introduces sensitivity to external environmental conditions such as temperature and atmospheric pressure. Therefore, it is essential to compare the behaviour of sealed and unsealed pressure sensors to determine how they are affected by such influences. The goal of this test is to assess whether sealed pressure sensors are suitable for use in the experiments described in chapter 3, or whether the trade-offs introduced by unsealed sensors—such as the interference from connecting tubes must be accepted.

This long-term test was conducted to evaluate how external factors, particularly temperature fluctuations and atmospheric pressure changes, influence the output of such pressure sensors over time.

Test Setup

The test was carried out over a total duration of 2 days and 3 hours. Three sensors were used:

- A digital thermometer measuring temperature in degrees Celsius.
- A pressure sensor with a sealed reference port.
- A pressure sensor with an open reference port to ambient air.

All sensors were sampled at a frequency of 2 Hz throughout the entire test. The pressure sensors provided voltage outputs within a range of ± 5 V, corresponding to a pressure range of ± 0.5 psi. The thermometer provided direct temperature readings in degrees Celsius. During the tests the sensors were placed in the lab in open air.

Instrumentation Details

Pressure Sensors

The two pressure sensors used in this experiment differ in reference configuration. The sealed sensor contains a fixed air pocket as its reference, making it susceptible to changes in internal temperature and external air pressure. The air pocket is closed-off using a 3D-printed polyester casing and made waterproof with a silicone sealant. The open sensor references atmospheric pressure, allowing for more direct response to environmental changes. Both pressure sensors were placed in the open air, enduring the same baseline pressure.

Digital Thermometer

A standard digital thermometer was used to monitor water temperature. It provided consistent readings in degrees Celsius and served as an independent temperature reference for assessing the influence of thermal drift on the sealed pressure sensor.

Data Acquisition

All three sensors were logged simultaneously at 2 Hz using a data acquisition system. Over the total test period, more than 360,000 data points were recorded per sensor. The data was saved in voltage (V) for the pressure sensors and degrees Celsius for the thermometer.

Atmospheric Pressure Reference

To compare the sensor behaviour with ambient pressure variations, hourly atmospheric pressure data was retrieved from a public weather station (Rotterdam Airport), retrieved from Meteostat, 2025. The reference data consisted of one pressure measurement per hour, covering the full test duration. This data was used primarily to assess the behaviour of the sealed pressure sensor relative to environmental pressure trends.

Post-Processing

The sensor data was later resampled to hourly averages to align with the atmospheric reference data. Voltage readings from the pressure sensors were converted to pressure values using the known conversion factor (0.1 psi/V). Additionally, temperature correction and drift analysis were performed to isolate the impact of thermal response and sealed cavity behaviour.

Converting temperature to Volts

The method used to convert temperature to voltage follows the approach described in section G.2, based on the ideal gas law. According to this relationship, an increase of 2 $^{\circ}\mathrm{C}$ corresponds to a decrease of 1 V in pressure sensor output. Therefore, to account for the influence of temperature in volts, the measured temperature values were multiplied by a factor of -0.5.

Implementing ambient air pressure

The ambient pressure data, obtained from Meteostat, 2025, was originally provided in hectopascals (hPa). To express this influence in volts, a two-step conversion was applied. First, the pressure values were normalized by subtracting the initial value from the dataset, ensuring that the starting point corresponded to zero. Next, the values were converted from hPa to psi using a factor of 0.0145038, and subsequently from psi to volts by multiplying by 10.

The measured data has been resampled over a period of an hour retrieving the hourly mean to align with the air pressure data.

Results

This section presents the results of the long-term measurement campaign, including sensor output, data processing, and external influence analysis.

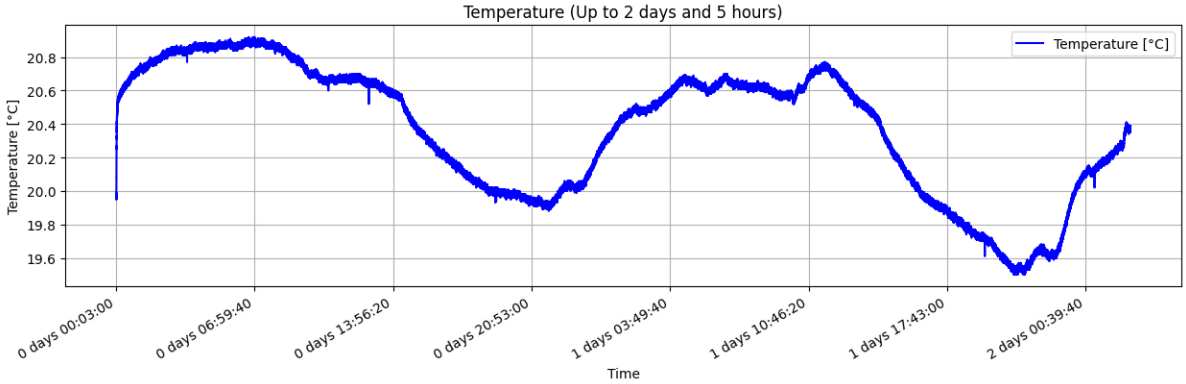

Figure G.6: Temperature progression (2 days and 3 hours)

The evolution of temperature throughout the test period is shown in Figure G.6, while the outputs of the sealed and unsealed pressure sensors are displayed in Figure G.7. These results are further integrated in Figure G.8, which combines sensor outputs with the temperature-based hypothesis (shown in black) and the derived effect of temperature on the sealed sensor output (shown in purple).

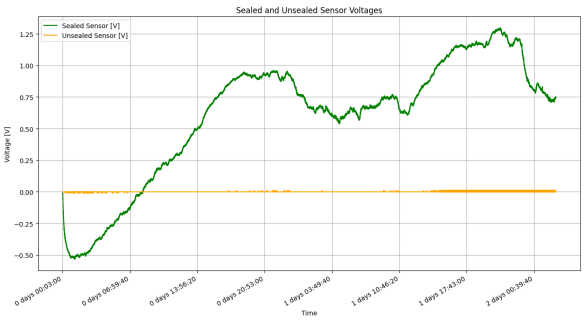

Figure G.7: Measurements Sealed and Unsealed pressure sensors

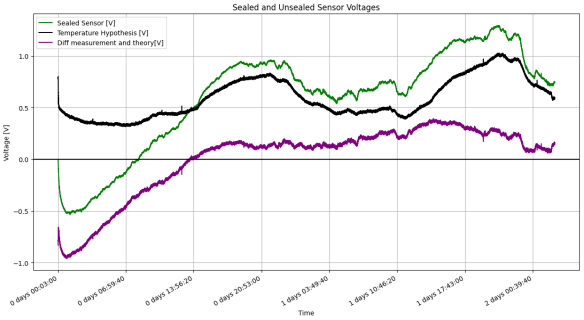

Figure G.8: Temperature influence and the Sealed output corrected with the temperature added

The influence of ambient air pressure is introduced in Figure G.9, where both external drivers, temperature and atmospheric pressure, are plotted. In Figure G.10, these theoretical external influences (purple) are compared directly to the measured data from the sealed sensor (green).

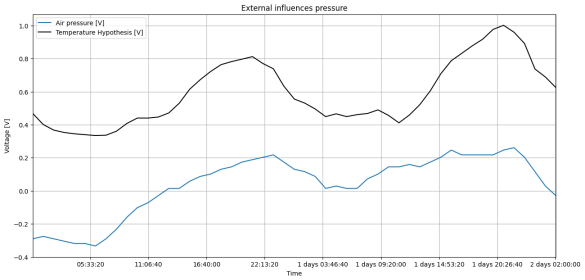

Figure G.9: External influences of the test (Temperature and Air pressure [Meteostat, 2025])

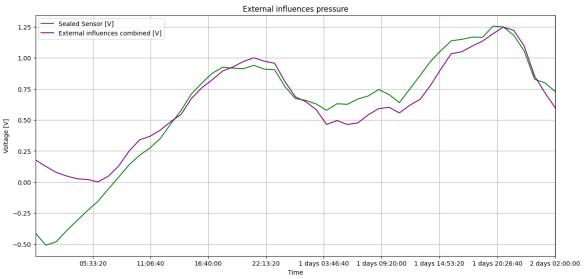

Figure G.10: External influences pressure variations Measurements vs theoretically obtained

Conclusion

The results of the long-term test show that the combined influence of atmospheric pressure and ambient temperature corresponds closely with the measured output of the sealed pressure sensor. This alignment suggests that both environmental factors play a significant role in shaping the pressure readings over time. In addition, the sealed sensor displayed a delayed response to temperature changes in the surrounding environment. This lag can be attributed to the thermal inertia of the sealed air chamber, which takes longer to reach equilibrium with the external conditions. These findings indicate that, while sealed sensors offer practical advantages in terms of form factor and flow integration, they require careful interpretation when used in environments subject to varying temperature and air pressure.

Recommendations

To improve the reliability of sealed pressure sensor measurements in future experiments, several adjustments are recommended. First, a thermometer should be placed as close as possible to the sealed pressure sensor array. This allows for accurate monitoring of local temperature conditions, which directly affect the internal air pocket and resulting sensor output. Second, it is advisable to place a sealed reference sensor outside the flume, in a stable ambient location. This external control sensor can be used to quantify and correct for the effect of ambient air pressure fluctuations, thereby enhancing the interpretability of the in-flume sensor data.

Discussion

Despite the informative results, the test is subject to several limitations and sources of uncertainty. The atmospheric pressure data used for comparison was obtained from the weather station at Rotterdam Airport, which may not perfectly reflect the conditions at the test site in Delft. Spatial variation in atmospheric pressure could lead to discrepancies between the measured and reference data. Furthermore, the precise start time of the experiment was not recorded, making it difficult to align the sensor data exactly with the hourly atmospheric pressure measurements. During the test, the thermometer was accidentally knocked to the ground, though it is unknown when this occurred. This incident may have introduced errors in the temperature measurements, particularly in the early or late stages of the test. Additionally, sensor drift and calibration uncertainty can influence results, particularly over a test duration of more than two days. The manual correction applied to the initial pressure readings introduces another layer of uncertainty, as it is unclear whether the sealed sensor had reached equilibrium at the time the baseline was set. It is also worth noting that the temperature in the water remained more stable than the ambient air temperature, which will likely buffer the sealed sensor from rapid environmental changes, as the long-term test was conducted in air, it may have endured these rapid changes.

G.4. Temperature Depth Sensor Test

This section describes the last sensor test that was performed.

Results

Figure G.11: Temperature depth test Depth-Voltage progression Sealed Sensor

- Temperature Depth Test Sealed Sensor
- Mean error between slopes: 0.000472 V/cm depth
- Mean error in psi: 4.72e-05 psi/cm depth
- Mean error in Pa: 0.325 Pa/cm depth
- Mean error in meters head: 3.32e-05 m/cm depth
- Mean error in percentage: 0.332 %

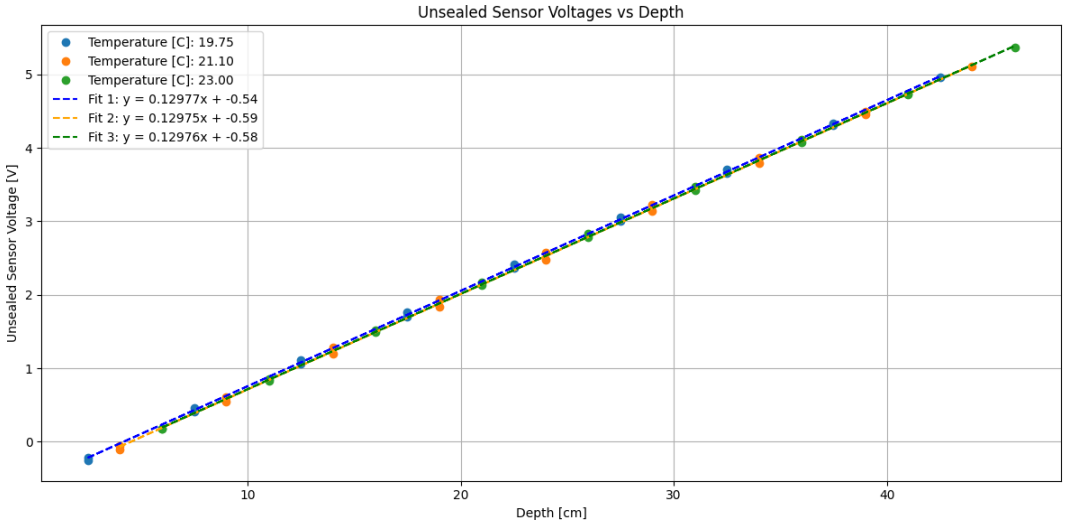

Figure G.12: Temperature depth test Depth-Voltage progression Reference Sensor

- Temperature Depth Test Unsealed Sensor
- Mean error between slopes: 1.29e-05 V/cm depth
- Mean error in psi: 1.29e-06 psi/cm depth

- Mean error in Pa: 0.00892 Pa/cm depth
- Mean error in meters head: 9.1e-07 m/cm depth
- Mean error in percentage: 0.0091 %

G.5. Pressure sensor Conclusion

The results of the temperature–depth test demonstrate that both the sealed and unsealed pressure sensors exhibit highly stable behaviour over the time periods relevant for the planned experiments, which have a maximum duration of approximately 50 minutes. The short-term drift is negligible, and the depth-voltage relationship remains effectively linear throughout the test range. The recorded mean errors—particularly in the unsealed sensor, where deviations remain below 0.01%, indicate that temperature effects and hydrostatic loading do not introduce significant bias over the operational depth.

Given this performance, the selected pressure sensors can be regarded as reliable for the experimental programme. The stability ensures that the measured pressure fluctuations will accurately reflect the hydraulic processes within the filter layer.